Pressureless Densification of SHS Produced Alumina – Titanium Diboride Ceramic Matrix Composites

By

Michael P. Hunt

Thesis submitted to the Faculty of the
Virginia Polytechnic Institute and State University
in partial fulfillment of the requirements for the degree of

Master of Science
In
Materials Science and Engineering

COMMITTEE:
Dr. Kathryn V. Logan, Chair
Dr. David E. Clark
Dr. Gary R. Pickrell
Dr. Carlos T. A. Suchicital

February 4, 2009
Blacksburg, Virginia

Keywords: Aluminum Oxide, Titanium Diboride, Aluminum Borate, Densification, SHS Produced Composites, Rate Controlling Diffusion Mechanism

Pressureless Densification of SHS Produced Alumina – Titanium Diboride Ceramic Matrix Composites

Michael P. Hunt

ABSTRACT

The research focus was to determine diffusion mechanisms responsible for densification behavior of SHS produced Al_2O_3/TiB_2 Ceramic Matrix Composites (CMCs). Previous research has shown SHS produced Al_2O_3/TiB_2 composites exhibited unique microstructural properties that contributed to high strength, fracture toughness, and hardness properties. Pressureless densification of SHS produced Al_2O_3/TiB_2 composites would provide a cost savings because the equipment for pressureless densification is less expensive and less complicated than equipment required for densification with pressure.

Models for sintering of CMCs and calculation of Sintering Time Constants (STCs) were used to predict the densification behavior of the SHS produced Al_2O_3/TiB_2 composite. The Levin, Dirnfeld, Shwam (LDS) equation was used to determine the Rate Controlling Diffusion Mechanism (RCDM) and activation energy for densification. X-Ray Diffraction (XRD) analysis of the as-milled reaction product powder revealed the presence of an aluminum borate ($Al_{18}B_4O_{33}$) as a third phase, as well as, in pressureless heat treated samples. Based on experimental results and analysis, it seemed possible the $Al_{18}B_4O_{33}$ compound may have formed by reaction of Al_2O_3 with TiB_2 along their interfaces. Aluminum borates have been observed to form $Al_{18}B_4O_{33\,(s)} + B_2O_{3\,(l)}$ at temperatures above 1000°C. The RCDM for densification of SHS produced Al_2O_3/TiB_2 was found to be liquid phase diffusion with volume diffusion also likely being active during densification. In addition, $Al_{18}B_4O_{33}$ seemed to be the preferred compound formed during oxidation. Further research should be performed to control formation of $Al_{18}B_4O_{33}$; as well as, on the oxidation behavior of the SHS produced Al_2O_3/TiB_2.

Dedicated to my grandparents.

Acknowledgements

First and foremost I would like to thank my Lord and Savior Jesus Christ for bearing a burden too heavy for me and paying a price that I could not afford on the cross of Calvary. I hope that this body of research and, more importantly, my life brings glory to Your name.

I would like to thank Dr. Kathryn Logan for her mentorship and advice throughout the duration of my graduate study. I would also like to thank Dr. Wallace Vaughn and Mr. Craig Leggette at NASA Langley Research Center for their assistance, guidance, and training on various pieces of equipment used in this research. Thanks to Mr. Jim Baughman, Mr. David Hartman, Mr. Keith Bird, Dr. Ravi Shenoy, and Mr. Steve McCartney for helping with the operation of characterization equipment and analysis of results at NASA Langley Research Center and the Nanoscale Characterization and Fabrication Laboratory at Virginia Tech.

Thanks also to Dr. David Clark and Ms. Diane Folz for the support they provided during my undergraduate research experiences and for their encouragement to pursue graduate studies. I would like to acknowledge Dr. Marie Paretti and the MSE/ESM Communications program at Virginia Tech for guidance, instruction, and support in the areas of technical writing and presentations. Mr. David Berry deserves recognition for his tireless efforts in keeping the equipment in the MSE department operational and for all the assistance he has provided the students of the department.

I gratefully acknowledge and thank the National Institute of Aerospace for material support of my research and NASA Langley Research Center for the use of their facilities to complete my research.

I would like to thank Mr. Brian Stewart, Mr. Eric Faierson, Dr. Jairaj Payyapilly, Ms. Susan Holt, and Ms. Sharon Jefferies for all of their support, insight, constructive criticism, and most importantly friendship. Thanks to Mr. Brad Hopkins, Mr. Scott Hopkins, and Mr. Michael Okyen for their assistance in getting the Center for Multifunctional Aerospace Materials (CMAM) at NASA Langley Research Center up and running.

I would also like to thank Dr. Carlos Suchicital and Dr. Gary Pickrell for serving on my committee and maintaining an open door policy throughout my undergraduate and graduate studies.

I would like to thank my parents, Patrick and Pamela Hunt, for their love, support, patience, wisdom, and guidance over the years. Thanks to my big brother, Vernon Hunt, for always looking out for me and believing that I have what it takes to tackle anything that may come my way. I love you all and I am eternally grateful to have you in my life.

Thanks to all of my friends that took the time to ask how my research was going, prayed with me or for me in good times and bad, and for the many laughs we've shared. I'd like to thank my church family at London Bridge Baptist Church (Virginia Beach, VA) and the 1st Church of God (Blacksburg, VA) for sharing their lives and homes with me throughout my studies.

Table of Contents

List of Figures

All figures are property of the author unless otherwise noted by a reference in the figure caption.

List of Tables

List of Acronyms

ANOVA – Analysis of Variance
CI – Confidence Interval
CIP – Cold Isostatic Pressing
CMC – Ceramic Matrix Composite
CMS – Compton Modified Scattering
DOE – Design of Experiments
DOF – Degrees of Freedom
EDS – Electron Dispersive Spectroscopy
ESEM – Environmental Scanning Electron Microscope
HIP – Hot Isostatic Pressing
HTC – High Temperature Ceramics
IPC – Interpenetrating Phase Composite
LDS – Levin, Dirnfeld, and Shwam
NPP – Normal Probability Plot
OVAT – One Variable at a Time
PPD – Polymer Precursor Degradation
PSA – Particle Size Analysis
PDF – Powder Diffraction Files
PR – Predicted Response
Pe – Péclet Number
QC – Quality Characteristic
RCDM – Rate Controlling Diffusion Mechanism
RCS – Rate Controlled Sintering
SD – Standard Deviation
SEM – Scanning Electron Microscopy
SHS – Self-Propagating High-Temperature Synthesis
SS – Sum of Squares
STC – Sintering Time Constant
TPS – Thermal Protection System
TSPP – Trisodium Pyrophosphate
UHTC – Ultra High Temperature Ceramics
VP-SEM – Variable Pressure Scanning Electron Microscope
XRD – X-Ray Diffraction

1. Introduction

This chapter presents the research objective, research goals, current state of knowledge, and significance of research. The current state of knowledge briefly covers production of Ceramic Matrix Composite (CMC) powders, heat treatment requirements for pressureless densification of manually mixed powders, Self-propagating High-temperature Synthesis (SHS) reactions, hot pressing of SHS produced powders, pressureless densification of SHS powders, Rate Controlling Diffusion Mechanism (RCDM), and activation energy. The significance of research discusses reductions in production costs, increasing production efficiency, and transition towards Rate Controlled Sintering (RCS).

1.1 Research Objective and Goals

The research focus was to determine diffusion mechanisms responsible for densification behavior of SHS produced Al_2O_3/TiB_2 ceramic matrix composites. The following goals were established:

1. Predict pressureless densification behavior of SHS produced Al_2O_3/TiB_2 powder using models from literature and data from Matsushita et al. and the ASM Handbook of Materials: Volume 4.

2. Experimentally determine the RCDM and activation energy for densifying SHS produced Al_2O_3/TiB_2.

3. Compare predictions from models with experimental results.

1.2 Overview of the Current State of Knowledge

CMC powders may be generated in a variety of ways including Polymer Precursor Degradation (PPD), manual mixing, and SHS reactions. Little research has been conducted on pressureless densification behaviors of PPD produced Al_2O_3/TiB_2 powders. Based on work performed by Matsushita et al. and Stadlbauer et al., pressureless densification of manually mixed Al_2O_3/TiB_2 has been demonstrated. However, pressureless densification of manually mixed Al_2O_3/TiB_2 required either multi-step forming processes or preliminary heat treatments.[1, 2]

It was shown by Stadlbauer et al., that mechanical properties of manually mixed Al_2O_3/TiB_2 were best after heat treatments between 1600°C and 1800°C. High final density (above 90% theoretical) for manually mixed Al_2O_3/TiB_2 powders heat treated below 1600°C

may only be obtained for compositions with 20 wt% or less TiB_2. Manually mixed composites with composition of ~70 wt% Al_2O_3/~30 wt% TiB_2 showed high final density for heat treatment temperatures above 1700°C.[2]

SHS reactions use heat generated from an initial chemical reaction sequence to initiate a series of identical chemical reaction sequences and are capable of synthesizing and/or forming ceramic materials. Previous work done by Logan showed that it is possible to hot press SHS produced ceramic matrix, non-oxide particulate reinforcement composites.[3] Pressureless densification of SHS produced CMCs has been studied by few researchers at this point.

Many factors affect the product of an SHS reaction including powder moisture content, heating rate, heating method, and stoichiometry of the reactants. High moisture content may create agglomerates within reactant powder mixtures; and, as a result, the agglomerates may react only on the surface leaving unreacted residuals within the interior.[3-7] It is unclear how the residuals might affect the diffusion and kinetics of the densification process. Greater understanding of densifying SHS produced powders may be gained from determining the RCDM and activation energy for densification.

Studying the RCDM for densifying SHS produced CMCs may increase understanding of how microstructures produced during densification help to create the CMC properties. In addition, understanding the RCDM of SHS produced CMC powders can provide important insight into SHS produced CMC densification behavior. Methods of matter transport within the material will determine the material behavior during densification and may affect the microstructures during densification.[8-10] The ability to pressurelessly densify SHS produced CMC powders creates new possibilities for forming and processing CMCs, particularly those with non-oxide particulate reinforcements.

1.3 Significance of Research

Al_2O_3/TiB_2 composites have demonstrated improved properties over the composite's pure constituents Al_2O_3 and TiB_2. The composite may have considerable impact on oxidation resistance behavior when compared with pure TiB_2.[9, 11, 12] Additionally, an SHS produced Al_2O_3/TiB_2 composite densified by hot pressing has been shown to have unique properties when compared with hot pressed Al_2O_3/TiB_2 formed from manually mixed Al_2O_3 and TiB_2 powders.[3]

The ability to successfully densify SHS produced Al_2O_3/TiB_2 composite powder without pressure would provide a processing alternative to hot pressing with potential cost savings.

Addition of pressure during densification requires expensive and complicated equipment to produce a fully dense part. When possible, pressureless densification is preferred as an alternative to densification with pressure because the equipment required for pressureless densification is less expensive. SHS production of composite powders provides a benefit of fusing composite constituent species during formation while manual mixing provides only a physical mixture of constituents. The fusion of constituents during SHS powder formation aids in the densification process.[10, 13, 14]

Use of models before experimentation provides a better understanding of what may be expected during experimentation and predictions of what heat treatment temperatures and times may be appropriate for experimentation.[15, 16] Understanding diffusion processes involved in densification of SHS produced Al_2O_3/TiB_2 composite powders allow possibilities for increased efficiency in production. Diffusion data can be used in implementation of a RCS process where shrinkage rates are held constant rather than heating rates. RCS can be used to create high density components with decreased intergranular pore frequency, grain size, heat treatment time, and heat treatment temperature. The activation energy and RCDM would help guide understanding of microstructure formation and final properties of SHS produced CMCs.[17, 18]

2. Survey of Literature

This chapter presents property comparisons, Al_2O_3/TiB_2 composite powder production methods, green body formation, Design of Experiments (DOE), modeling of densification, densification by diffusion, microstructure formation by diffusion, Rate Controlling Diffusion Mechanism (RCDM), activation energy, and densified sample characterization techniques. The property comparison section covers composite to constituent component property comparisons, processing method comparisons, and desired uses relating to key properties. The Al_2O_3/TiB_2 composite powder production section focuses on Self-propagating High-temperature Synthesis (SHS) reactions, manual mixing of constituent powders, particle size reduction techniques, and powder characterization methods.

Green body formation provides background on uniaxial pressing, isostatic pressing, and slip casting methods. DOE provides information on fundamentals of DOE, methodology, analytical tools, predicting response function, and confirmation experiments. The modeling of densification section shows how Sintering Time Constants (STCs) may be calculated and composite densities predicted under certain heat treatment conditions. Densification by diffusion explains mass transport, effects of chemical reaction on diffusion, and microstructure considerations.

Microstructure formation by diffusion discusses volume (or bulk) diffusion, grain boundary diffusion, liquid phase diffusion, and evaporation–condensation. The RCDM and activation energy sections cover experimental determination of the RCDM and activation energy. The densified sample characterization techniques section describes processes for determining density, shrinkage, and microstructural features.

2.1 Properties Comparisons

This section includes composite and constituent properties comparisons, processing method comparison, and properties with their desired uses. The composite and constituent properties comparison explores Ceramic Matrix Composites (CMCs), Ultra High Temperature Ceramics (UHTCs), and some differences in the Al_2O_3/TiB_2 CMC, and the Al_2O_3 and TiB_2 constituents. The processing method comparison section briefly discusses property differences due to powder production method and densification process. The properties and desired uses

section explains some key properties of the Al_2O_3/TiB_2 composite and some potential applications associated with each property.

2.1.1 Composite and Constituent Property Comparisons

CMCs are a class of ceramics incorporating a secondary phase to change properties of the matrix and/or reinforcing phases. Composite materials combine properties from their constituents to produce materials with properties uniquely different from the individual constituents. It is ideal for final properties of a composite to be better than properties of at least one of its constituents; however, there are some cases where composite properties are worse than properties of individual constituents.[9, 11]

UHTCs are ceramics able to maintain structural stability above melting temperatures of High Temperature Ceramics (HTCs). There is no clear cut-off point for distinguishing UHTCs from HTCs. The literature seems to suggest ceramics with melting points above 2000°C may be considered UHTCs. UHTCs generally consist of metal borides, carbides, and nitrides.[19]

One weak point of UHTCs can be oxidation resistance since boron, carbon, and nitrogen can readily form oxides and escape into the atmosphere leaving behind metal that may melt at UHTC oxidation temperatures. Another major concern with UHTCs is cost of production. Since UHTC materials have melting points greater than 2000°C, UHTCs are generally formed and densified by hot pressing.[9, 13, 14, 20, 21] The need for pressure application at elevated temperatures tends to increase cost of production for UHTCs. Pressureless densification is an alternative to hot pressing but generally requires prohibitively high temperatures and a very expensive inert atmosphere or vacuum furnace.[9, 13, 14, 21]

Oxide matrix – UHTC reinforcement composites provide possibilities for greater oxidation resistance and reduced processing costs, with limited loss of UHTC properties as shown in Table 2.1. The oxide matrix provides a measure of protection from oxidation for the UHTC reinforcement and may form a metal nitride or metal oxy-nitride skin. If the oxide matrix had an appreciably lower melting temperature than the UHTC reinforcement, or if the matrix and reinforcement formed a eutectic, then pressureless densification of the composite may be possible at much lower temperatures than the UHTC alone.[12]

Table 2.1 – Comparison of Al_2O_3/TiB_2 Properties with Al_2O_3 and TiB_2 Individual Properties[3, 9, 22, 23]

Property	Al_2O_3/TiB_2	Al_2O_3	TiB_2
Density (g/cm^3)	4.12	3.99	4.52
Compressive Strength (MPa)	2470 – 3032†	2470 – 2730	3388 – 3736
Hardness Vickers (GPa)	15 – 30	15 – 20	15 – 36
Fracture Toughness ($MPa*m^{1/2}$)	3.6 – 6.7	5.7 – 6.3	6.7 – 8.0
Electrical Resistivity (μohm*cm)	$1x10^{21}$ – $8x10^{21}$†	$1x10^{21}$ – $1x10^{22}$	8.99 – 17
Thermal Conductivity (W/m*K)	28.8 – 48.1†	28.8 – 31.2	77.8 – 96.0
Melting Point (°C)	2096 – 2350†	2004 – 2096	2916 – 3045

† Data point calculated using the composite rule of mixtures.

2.1.2 Processing Method Property Comparisons

Mechanical properties of Al_2O_3/TiB_2 may vary depending on powder production and heat treatment methods as shown in Table 2.2. Pressureless densification of manually mixed powders has been demonstrated as an alternative to hot pressing in producing similar properties. Hot pressing of SHS produced powders has shown improvements in some mechanical properties; namely, fracture toughness and hardness. It is believed further research with densification of SHS produced Al_2O_3/TiB_2 may result in even better mechanical properties than have been demonstrated to date. Pressureless heat treatment of SHS produced Al_2O_3/TiB_2 was not included in Table 2.2 because data on its mechanical properties is not available.[1-3, 24]

Table 2.2 – Comparison of Mechanical Properties for Heat Treatment of Manually Mixed and SHS Produced Al_2O_3/TiB_2 Composites[1-3, 24]

Property	Manually Mixed		SHS
Heat Treatment	Pressureless	Hot Pressed	Hot Pressed
Relative Density (%)	90.0 – 95.0%	99.2 – 99.7%	97.0 – 99.0%
Flexural Strength (MPa)	220 – 330	775 – 785	200 – 450
Fracture Toughness ($MPa*m^{1/2}$)	3.6 – 5.2	4.7 – 5.2	3.6 – 6.7
Hardness (GPa)	10 – 14	20 – 21	15 – 30

2.1.3 Properties and Desired Engineering Uses

This section discusses some key properties and behaviors of Al_2O_3/TiB_2 and potential uses derived from the material properties. Impact resistance behaviors of Al_2O_3/TiB_2 composites have made it a candidate for Personal Protective Equipment (PPE) and meteoroid shielding for

space craft. Wear resistance properties have led to consideration of using Al_2O_3/TiB_2 in braking systems for automobiles and aircraft. Thermal properties of Al_2O_3/TiB_2 including melting point, thermal conductivity, and potential oxidation and thermal shock behavior suggest its use as a Thermal Protection System (TPS) material. The presence of a secondary phase (TiB_2) allows a wider variety of possible microstructures to be created than within a single phase material. Therefore, composite performance properties may be controlled by varying composite microstructure.[2, 3, 25-27]

2.1.3.1 Impact Resistance

Impact resistance is a material's ability to resist damage and/or failure due to impact with an object. Impact resistance is important for PPE applications because it may be a measure of a material's ability to stop a projectile without damage or failure of the PPE material. Historically, it has been unclear which property or properties are most important in producing high impact resistance. Hardness, fracture toughness, and strength have been commonly accepted as responsible for performance characteristics of any armor material.[3, 25-27] Al_2O_3/TiB_2 composites have been considered for armor because the Al_2O_3/TiB_2 composites are believed to perform as well as TiB_2 armor ceramics with substantially lower production costs. In addition, Al_2O_3/TiB_2 showed higher space efficiency than silicon carbide (SiC) and a mass efficiency almost equal to SiC against medium caliber threats.[26]

According to Gilde et al., differences in microstructure created no discernable differences in performance of Al_2O_3/TiB_2 during depth of penetration testing.[27] On the other hand, Keller et al. found microstructure created noticeable differences in properties and armor performance.[25] High mass efficiencies were observed for Al_2O_3/TiB_2 composites when TiB_2 was localized at Al_2O_3 grain boundaries. Electrostatic dispersion of TiB_2 around Al_2O_3 was most efficient in producing the desired structure. Electrostatic dispersion relies on the build up of charge onto Al_2O_3 (positive charge) and TiB_2 (negative charge) during a dry ball milling process. The TiB_2 particles then coat the Al_2O_3 agglomerates based on attractive forces due to charge differences.[26] Experiments performed by Adams et al. showed dispersing TiB_2 around Al_2O_3 produced composites with better performance than Al_2O_3 and TiB_2 separately. Conversely, low density or high porosity has been shown to significantly degrade strength properties and armor performance. Phase size and distribution have also been proven to affect failure resistance.[25, 28]

2.1.3.2 Wear Resistance

Wear resistance is defined as a material's ability to resist degradation due to abrasion and friction. Materials with high resistance to wear have been used for cutting tool inserts and braking systems. However, cutting tool inserts and braking systems require more than wear resistance to maximize life and effectiveness.[24, 29, 30]

Hardness, melting point, and wear resistance properties of a material are important in production of brakes and braking systems. Higher vehicle speeds and shorter braking distances require a higher hardness and melting point for the material to effectively decelerate the vehicle. On the other hand, wear resistance is important for longevity of brakes and braking systems. Al_2O_3/TiB_2 composites have demonstrated hardness values approaching pure TiB_2 and a melting point above 2000°C as shown in Table 2.1.[3, 22, 30]

2.1.3.3 Thermal Properties and Oxidation Behavior

A material's usefulness in high temperature applications is dependent on its response to a specific temperature or temperature change for a desired application. However, thermal properties such as melting point and thermal conductivity are not the only properties requiring consideration for high temperature applications. Oxidation behavior and resistance to oxidation of a material are vitally important when considering high temperature applications in air or other oxidizing environments. Thermal properties and oxidation behavior are major considerations for TPS materials.[12, 14, 19, 31-33]

TPS materials must have a high melting point and low thermal conductivity. If the TPS will be used in hypersonic flow environments or in environments rich in oxygen, then oxidation resistance becomes very important as well. A material's oxidation resistance at high temperature may be improved by formation of a passivating oxide layer. Thus far, passivating oxide layers have been in the form of a refractory crystalline oxide scale with an amorphous component filling any voids.[12, 19, 32-34] An example of a composite system forming an effective passivating layer during oxidation would be aluminum nitride (AlN)/hafnium diboride (HfB_2) composites. During oxidation of AlN/HfB_2, a hafnium oxide (HfO_2) scale and aluminum borate ($Al_4B_2O_9$ or $Al_{18}B_4O_{33}$ depending on oxidation temperature) are formed. At temperatures above 1000°C, $Al_{18}B_4O_{33}$ forms along with a B_2O_3 rich amorphous phase that fills in the pore spaces in the HfO_2 and prevents further oxidation from occurring.[35]

Based on high-temperature compressive strength tests, TiB_2 has a potential to be useful for a high temperature application such as a TPS. However, most diborides experience considerable degradation due to oxidation at elevated temperatures. Degradation of diborides is generally a result of boron oxide (B_2O_3) formation at the material surface. Vaporization of B_2O_3 has been observed as low as 1150°C in free oxygen rich environments; however, in a standard atmosphere B_2O_3 boils at 1860°C.[9, 36] Gaseous B_2O_3 is the dominating vapor species for diborides at temperatures above 1500°C. High B_2O_3 vapor pressure at temperatures above 1500°C would lead to considerable mass loss in TiB_2 by vaporization of B_2O_3 even at low oxygen partial pressures. However, formation of a titanium oxide (TiO_2) layer on the surface of TiB_2 reduces or prevents further oxidation of subsurface material.[36]

Oxide matrix – boride reinforced composites have been suggested as a means to protect borides from oxidation while improving properties of oxide matrix materials.[12, 37] The oxide matrix provides its own difficulties because diffusion of oxygen from the matrix may lead to oxidation of diboride reinforcements under certain conditions.[36] In the Al_2O_3/TiB_2 system specifically, formation of B_2O_3, aluminum sub-oxide (Al_2O), and titanium oxide (Ti_2O_3) at elevated heat treatment temperatures has been predicted by thermodynamics as shown in Equation 2.1. Further calculation, revealed a reaction (in Equation 2.1) would begin at ~1500°C.[38] Evidence of a reaction may be determined by sample mass loss (as Al_2O is volatile) or by identification of new compounds by X-Ray Diffraction (XRD). [36-38]

$$9\,Al_2O_3 + 4\,TiB_2 \rightarrow 9Al_2O + 2Ti_2O_3 + 4\,B_2O_3 \qquad (2.1)$$

Formation of glassy surfaces with inner oxide layers has been observed for Al_2O_3/TiB_2 composites heat treated below 1150°C in oxygen-rich environments. Boron's small atomic radius is believed to allow more rapid diffusion to the material surface where B_2O_3 liquid is formed.[36] While oxidation resistance characteristics of Al_2O_3/TiB_2 composites have not been researched extensively, the material is known to have a melting point above 2000°C (meaning both constituents have melting points above 2000°C) and thermal conductivity similar to Al_2O_3.[12, 19, 32-34]

2.1.3.4 Thermal Shock Resistance

Thermal shock resistance is a material's ability to resist fracture or catastrophic crack propagation when experiencing a rapid change in temperature. Thermal shock resistance is

important for applications where materials are subject to wide and rapid fluctuations in temperature. A TPS for a hypersonic vehicle would be an example application where materials would undergo such temperature fluctuations.[33, 39, 40]

High thermal conductivity materials, in general, have better resistance to thermal shock because of their ability to reduce interior temperature gradients that in turn, reduce thermal stresses. Two of the most important thermal shock resistance factors for brittle materials are fracture toughness and fracture strength. The thermal stress fracture (R') and thermal stress damage (R"") resistance parameters are commonly used to evaluate thermal shock properties of ceramics. R' is a representation of critical temperature change (ΔT_c) required to initiate fracture under steady state heat flow while R"" represents the ΔT_c required for catastrophic crack propagation initiation. R' and R"" are dependent on many properties including fracture strength (σ_f), thermal conductivity (λ), Poisson's ratio (μ), coefficient of thermal expansion (α), Young's modulus (E), and fracture toughness (K_{IC}) as shown in Equations 2.2 and 2.3.[39, 41, 42]

$$R' = \frac{\sigma_f \lambda (1 - \mu)}{\alpha E} \tag{2.2}$$

$$R'''' = \frac{K_{IC}^2}{\sigma_f^2 (1 - \mu)} \tag{2.3}$$

TiB_2 has shown great potential for high temperature applications because of its hardness, high melting point, high thermal and electrical conductivity, and good thermal shock stability.[3, 9, 22, 23, 39] Excellent high temperature performance has been shown in composite materials where both matrix and reinforcing phases have continuous three-dimensionally interpenetrating microstructure. Composites with interpenetrating microstructure are known as Interpenetrating Phase Composites (IPCs).[39, 41, 42]

When compared with traditional CMCs, IPCs have potential to further improve thermal stability and some high-temperature properties. During loading or rapid temperature change in IPCs, the reinforcing phase may transfer stresses effectively in all directions using toughening mechanisms such as crack deflection, pinning, and bridging providing resistance to crack growth. Continuity of TiB_2 reinforcement throughout an Al_2O_3 matrix has been demonstrated in SHS produced Al_2O_3/TiB_2 and should result in improved thermal shock resistance due to IPC structure. According to Equations 2.2 and 2.3, Al_2O_3/TiB_2 composites should have better

resistance to fracture under steady state heat flow than tungsten (W)/copper (Cu) composites as shown in Table 2.3. However, resistance to catastrophic crack propagation for Al_2O_3/TiB_2 is significantly less than for W/Cu composites.[3, 39, 41, 42]

Table 2.3 – Mechanical Properties and Calculated Thermal Shock Resistance for Al_2O_3, TiB_2, Al_2O_3/TiB_2, and W/Cu.[3, 9, 22, 24, 39]

Property	Al_2O_3	TiB_2	Al_2O_3/TiB_2 (70/30 by wt%)	W/Cu
Fracture Strength (MPa)	327.7	406.6	348.5	483
Thermal Conductivity (W/m*K)	31.2	24.0	29.3	135
Poisson's Ratio	0.27	0.10	0.23	0.33
Coefficient of Thermal Expansion (μstrain/K)	9.1×10^{-6}	6.0×10^{-6}	8.3×10^{-6}	5.6×10^{-6}
Young's Modulus (GPa)	410	410	410	312
Fracture Toughness (MPa*$m^{1/2}$)	6.3	6.7	6.4	14.7
R' (W/m)	2000	3570	2330	2198
R""	506.3	301.7	435.9	1386.0

2.2 Al_2O_3/TiB_2 Composite Powder Production Methods

This section explains production of Al_2O_3/TiB_2 composite powders by SHS reaction and manual mixing; as well as, particle size reduction and powder characterization techniques. Under the SHS section, general information on production of Al_2O_3/TiB_2 powder by SHS reaction, aluminum borate formation, properties of aluminum borate, and particle size effects on reaction products are discussed. The manual mixing section includes information on methods of mixing, mechanisms for mixing, mechanisms for demixing, and impurity considerations. The particle size reduction section discusses several techniques including jet milling, attrition milling, and ball milling. The powder characterization techniques section describes methods for determining particle size, particle shape, compounds, and surface area.

2.2.1 Self-Propagating High Temperature Synthesis

SHS reactions are a form of reaction synthesis using energy released from initiation of a sequence of chemical reactions to initiate further reaction and produce a desired product. SHS reactions have advantages such as high purity reaction products, low energy investments, and short processing time.[1, 3-5, 7, 43, 44] An advantage of SHS production of CMC powders is pressureless densification without additives. Sinterability is believed to be due to the fine ultimate particle size of reacted powders; as well as, free metal (in quantities generally below

detection limits of XRD) that may form a liquid phase to aid in densification. In addition, high cooling rates and defect concentrations associated with SHS reactions are expected to create non-equilibrium metastable phases in the reaction product. The metastable phases are also believed to promote sinterability of SHS produced materials. Microstructures of SHS produced CMCs tend to show excellent dispersion of phases partially due to local sintering during synthesis. [3-5, 7, 45-47]

The reaction represented by Equation 2.4 to produce Al_2O_3/TiB_2 uses a mixture of aluminum (Al), anhydrous boron oxide (B_2O_3), and titanium oxide (TiO_2) powders that is heated until reaction initiation occurs. The reaction product is a friable ceramic composite that requires milling to produce a powder precursor for a compact. Additional milling may be used to further reduce particle sizes of produced products. Other compounds may be formed during reaction since Al_2O_3 reaction products may react with B_2O_3 and TiO_2 before reaction completion.[3, 4, 7, 45-47]

$$10Al + 3\,B_2O_3 + 3\,TiO_2 \rightarrow 5\,Al_2O_3 + 3\,TiB_2 \qquad (2.4)$$

Based on previous work done by Logan, aluminum borate ($Al_{18}B_4O_{33}$) has been observed within SHS reaction products of the Al, B_2O_3, and TiO_2 reaction. $Al_{18}B_4O_{33}$ is an aluminum borate compound comprised of nine Al_2O_3 molecules and two B_2O_3 molecules. The presence of $Al_{18}B_4O_{33}$ is believed to be partially responsible for unique microstructural properties created during processing of SHS produced Al_2O_3/TiB_2 composites. [3-5, 7, 45, 46]

2.2.1.1 Properties of $Al_{18}B_4O_{33}$

Two primary aluminum borate compounds have been found to exist; one containing a 2:1 ratio of Al_2O_3 to B_2O_3 ($Al_4B_2O_9$), and the other containing a 9:2 ratio of Al_2O_3 to B_2O_3 ($Al_{18}B_4O_{33}$) as shown in Figure 2.1. During reaction, the ratio of Al to B seems to determine whether $Al_4B_2O_9$ or $Al_{18}B_4O_{33}$ is formed.[48, 49] Based on work done by Gielisse and Foster, $Al_4B_2O_9$ is currently believed to melt incongruently at 1035°C to form $Al_{18}B_4O_{33\,(s)} + B_2O_{3\,(l)}$, with $Al_{18}B_4O_{33}$ melting at 1965°C.[48] The elastic modulus and hardness values for $Al_4B_2O_9$ and $Al_{18}B_4O_{33}$ are listed in Table 2.4.[48-50]

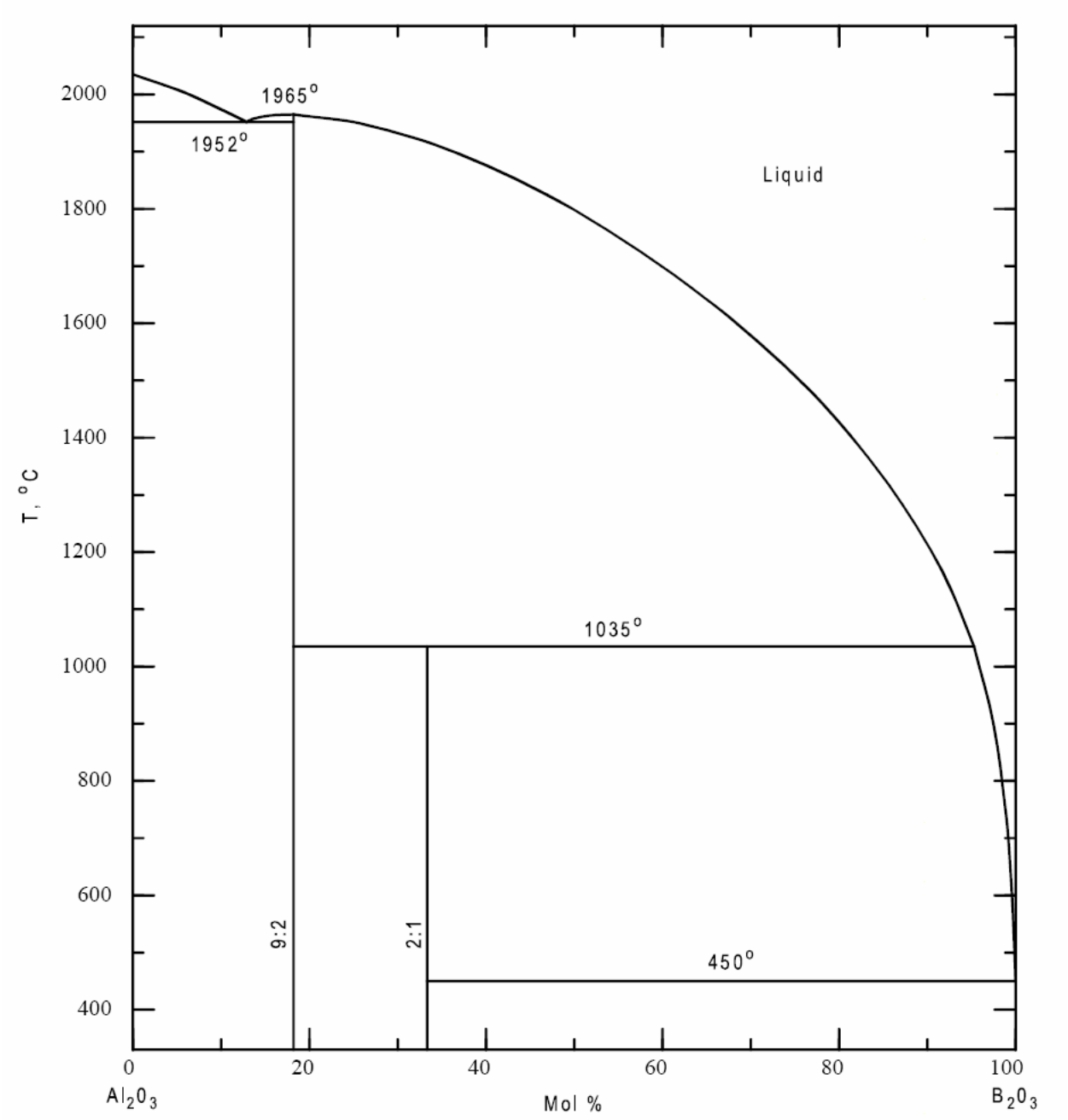

Figure 2.1 – Phase diagram for the Al_2O_3 – B_2O_3 system.[51]

Table 2.4 – Elastic Modulus and Hardness of Aluminum Borates[50]

Property	$Al_4B_2O_9$	$Al_{18}B_4O_{33}$
Elastic Modulus (GPa)	102 – 104	117 – 125
Hardness (GPa)	10.1 – 10.7	12.4 – 13.2

Depending on temperature and other constituents present, $Al_{18}B_4O_{33}$ may help or hinder densification of CMCs. $Al_{18}B_4O_{33}$ is believed to form in aluminum nitride (AlN)/zirconium

diboride (ZrB_2) ceramics by chemisorption of B_2O_3 (from ZrB_2) onto the surface of Al_2O_3 before densification begins. In work done by Postrach and Potschke, $Al_{18}B_4O_{33}$ was believed to impede densification of AlN/ZrB_2 at temperatures below 1700°C by reducing levels of sintering activity.[49] However, at temperatures above 1700°C, it was believed that $Al_{18}B_4O_{33}$ began to melt and activated sintering of AlN/ZrB_2 ceramics allowing for high densities at short times. Increased B_2O_3 content in Al_2O_3/B_2O_3 compacts was shown to significantly decrease relative density for given heat treatment conditions, which may indicate formation of $Al_4B_2O_9$ hinders the densification process. Formation of $Al_{18}B_4O_{33}$ is generally evidenced in the microstructure by acicular crystallites averaging 450 nm in diameter and 3-8 μm in length.[49, 52, 53]

2.2.1.2 Particle Size and Configuration Considerations

In an SHS reaction, particle size and configuration have a substantial effect on reaction characteristics.[54] Reaction initiation temperature, as well as product particle size, morphology, and density are all affected by the reactant particles. Controlling reactant particle sizes makes it possible to produce sub-micrometer powders by SHS reaction. In production of SiC by direct reaction of silicon (Si) and carbon (C), particle sizes of C control final particle sizes of SiC.[4] Previous research also suggests morphology of SiC products may be controlled by C reactant morphology. Also, SHS reaction initiation temperatures have been shown to be affected by particle size and stoichiometry of reactants.[4, 6, 9]

A broad particle size distribution can potentially occur during processing of raw materials. Wide particle size distributions may create preferred ordering during subsequent mixing and packing of powders, which will ultimately affect reaction initiation temperatures and probabilities of reaction completion. One possibility is particles would order with ideal particle stacking on decreasing size scales as shown in Figure 2.2. Large particles would then form an ideal particle stacking structure and smaller particles, in the same ideal stacking structure, would fill void spaces left by larger particles. Since each particle size scale would mostly be comprised of the same material, such an arrangement of particles may hinder interaction of chemical constituents required to initiate an SHS Al_2O_3/TiB_2 reaction.[4, 13, 29, 55]

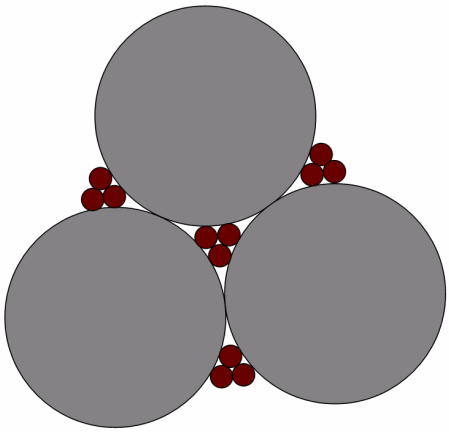

Figure 2.2 – Particle packing configuration where smaller particles fill in the spaces between larger particles.

The Brazil-nut effect is another possible configuration and occurs when smaller particles migrate to a mixture's bottom while larger particles remain at the top as shown in Figure 2.3. A Brazil-nut effect configuration would provide some surface interaction between larger and smaller particles but the SHS reaction would likely not complete. However, in either case, formation of a liquid during initial heating or reaction would greatly increase diffusion rates allowing reaction completion.[4, 55, 56]

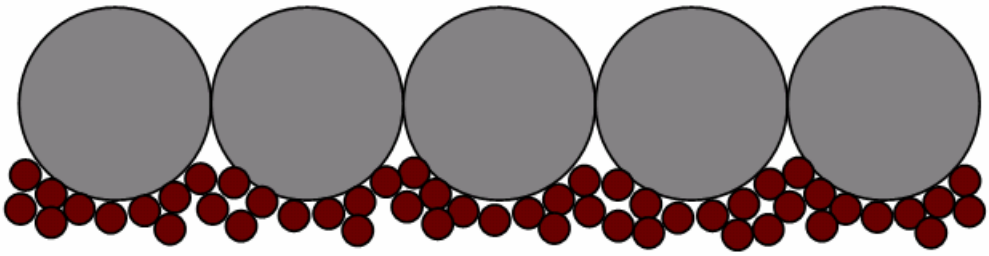

Figure 2.3 – Particle packing configuration where smaller particles settle to the bottom.

2.2.2 Manual Mixing

Manual mixing combines commercially available powders to create a composite mixture of the desired material. Manual mixing has the advantage of being simple but is limited by purity and structure of starting materials. Methods of mixing include ball milling and planetary mixing. Ball milling is ideal when powder to be mixed will not form compacted layers on milling media or milling jar walls. Generally, use of a surfactant even in small quantities can greatly reduce compaction on media and jar walls. Milling is also a method to reduce the size of particles, which should lead to more uniform mixtures on the micro-scale. Planetary mixers are used to

mix pastes and use shearing motions to reduce particle sizes. Pastes must have high apparent viscosities so agglomerates will break down and liquid components can contact all individual particles during the shearing motion. Mixing tools move in a complex pattern through a rotating or stationary cylindrical bowl containing materials to be mixed.[1, 3, 4, 7, 43, 44]

There are three primary mechanisms for mixing solid particulates: convective, shear, and diffusive mixing. In convective mixing, mixture parts interchange according to circulation patterns established by the mixing method. As the interfacial area between different components increases during mixing, particles begin to break forming smaller particle sizes and more uniform mixtures. Convective mixing may occur in all mixtures regardless of rheology and is most effective during early stages of mixing.[9, 13, 14, 55]

Shear mixing uses relative movement of particles within a mixture to draw out regions containing different compounds and improve mixture uniformity. Shear mixing may also occur in a variety of mixtures. Diffusive mixing is similar to molecular diffusion through fluids and requires free-flowing particles in suspensions of non-attracting particles. Individual particles are moved by mixer action or gravity, and when particles collide the particles are randomly scattered in the mixture. Diffusive mixing causes compositions of particles close in size to become more uniform; but even small particle size differences may cause demixing.[9, 13, 14, 55]

Demixing occurs due to particle size differences and by three primary mechanisms: trajectory segregation, percolation, and rising/settling. Trajectory segregation occurs when powders are moving non-uniformly during mixing and larger particles are moved further than smaller particles. In percolation, coarse particles create a network through which fines are able to move through and separate out. Rising is a phenomenon similar to the Brazil nut effect and is only observed in dry mixing. During rising, large particles rise to the mixture surface due to vibration, and fines move into vacated spaces left by large particles. Settling is primarily observed in wet mixtures and is characterized by large particles settling to the bottom of a mixture, while fines remain in the mixture. Differences in particle density has a larger effect on wet mixtures as more dense particles tend to settle faster for a given particle size.[9, 13, 14, 55]

Another major consideration for mixing processes is the presence of impurities from processing of raw materials. Since the researcher does not generally control synthesis of materials being mixed, it is important to consider how each raw material was processed and what impurities may be introduced from processing. Processing impurities may affect the

characteristics of subsequent reactions and, consequently, other aspects of processing, particularly densification. [9, 13, 14, 57]

2.2.3 Particle Size Reduction Techniques

This section focuses on reduction of particle size by jet, attrition, and ball milling. Due to the process of reactant to product volume changes, release of volatile gases during reaction, and short reaction times, most SHS reactions result in low density friable ceramics.[4] Milling of SHS Al_2O_3/TiB_2 reaction products is necessary to produce a uniform Al_2O_3/TiB_2 powder precursor for further compaction. There are various methods for reducing particle size of powders including jet, attrition, and ball milling. The relative hardness of constituents being milled may significantly affect final particle size distributions for resultant powders. The amount of energy used on particles during particle size reduction may also affect final compounds and structure of powder constituents.[4, 9, 13, 14, 58]

Jet milling pushes high speed gas through a nozzle and into a chamber containing particles to be milled. The created jet streams are used to accelerate particles into one another and chamber walls to reduce particle sizes. Large amounts of kinetic energy are generated by particles moving in the jet stream, and the kinetic energy is used to fracture particles until desired sizes are achieved. Jet mills rely on the momentum of particles, which is created by movement of fluid; meaning milling is limited by interaction of particles with the jet stream.[13, 14, 59]

Attrition mills are comprised of a grinding chamber with an impeller and a separator allowing fines of a particular size and smaller to escape the grinding chamber. The impeller is driven by a motor and has protruding grinding surfaces used to crush particles against chamber walls thus reducing particle size. Attrition mills are generally found in larger scale production environments where constant throughput is important to production. Milling speed, impeller diameter, and grinding element design all have a potential to impact final properties of attrition milled powders.[13, 14, 60]

Ball milling makes use of a rolling mill, jar, and milling media (also known as balls) to reduce sizes of powder particles. The jar is loaded with powder and milling media, sealed, and then placed on a set of rollers driven by a motor. As the jar turns, media follow the jar's profile as the media approach the jar's top and then fall to the jar's bottom as shown in Figure 2.4. The kinetic energy produced from falling media is transferred into the powder as media impact the jar's bottom.[9, 13, 14]

Ball milling relies on differences in hardness and fracture toughness between powder constituents, jar walls, and milling media to reduce particle sizes of powder. Based on the Brazil nut effect, larger particles should be on top when media strikes the powder on the jar's bottom. However, powder may become very compacted during dry milling and the compacted powder may behave more like the jar wall than loose particles. [9, 13, 14]

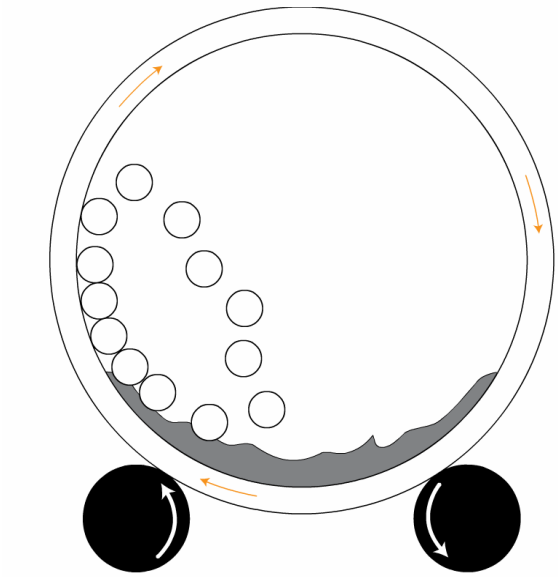

Figure 2.4 – Schematic of ball milling process used to reduce particle size.

2.2.4 Powder Characterization Techniques

This section discusses techniques for determining particle size and shape, compound identification, and surface area. Characterization of powders may provide valuable information on materials being used for experimentation. Size and shape of powder particles may have a significant impact on production of powder compacts and densification of compacts. Chemical and compound makeup of powders used for experimentation provides insight into impurities present within a sample and effects on densification. Determination of particle surface area may give some indication of particle surface energy. High particle surface energy may act as a driving force for densification.[9, 61, 62]

2.2.4.1 Particle Size and Shape Determination

Particle Size Analysis (PSA) may be used to determine distribution of particle sizes within a powder. Most PSA instruments use refraction of lasers of different wavelengths to determine the size of individual particles. A liquid dispersant is generally used as the medium

for particle size determination. However, some newer instruments include configurations for dry measurements. Dry measurements would be useful in determining particle size distributions for powders sensitive to liquid exposure.[9, 62]

For composite powders, index of refraction used to determine particle size distribution is very important unless both matrix and reinforcement materials have similar indices. For manually mixed composites, it is most accurate and convenient to determine particle size distributions for each individual constituent. However, SHS produced composite powders experience some sintering during synthesis, which makes it impossible to separate constituents. There are three basic approaches for determining distributions of composite powders based on using matrix, reinforcement, or rule of mixtures indices. If matrix and reinforcement indices are similar to one another, then it is appropriate to use the dominant phase index according to volume or overall number of constituent particles. If not, using the rule of mixtures is a good approximation of a composites particle size distribution.[9, 62]

Scanning Electron Microscopy (SEM) may be used to determine the shape and surface texture of powder particles. In a SEM, an electron beam is focused onto a small material surface region using magnetic focusing lenses. Scattered electrons released from a sample, because of exposure to an electron beam, are collected by a fixed detector producing a signal and the signal is processed into an image. As the beam scans the small sample region, a continually refreshed image is produced. SEMs are commonly used for imaging because depth of focus is greater than may be achieved with an optical microscope. Depending on software used to operate an SEM, it may be possible to measure sizes of objects within the image produced.[9, 62]

2.2.4.2 Compound Identification

This section covers basics of compound identification by XRD including scattering, diffracted beam intensities, amorphous phases, preferred orientation, and crystallite size effects. An X-ray beam is an electromagnetic wave whose electric field strength varies sinusoidally with time along the beam. Any electric field will exert a force on a charged particle causing the particle to move similarly to the field exerting the force. Since X-rays have an oscillating magnetic field, any electron an X-ray beam encounters will begin oscillatory motion about its mean position. Oscillating electrons continuously accelerate and decelerate resulting in production of an electromagnetic wave. Electrons scatter X-rays by radiating a scattered beam in response to an incident X-ray beam and beams scattered by oscillating electrons will have

identical wavelength and frequency of its incident beam. The Thompson equation explains electron scattering of incident X-rays in terms of incident beam intensity (I_0), electron scattered beam intensity (I_e), electron charge (e), distance between source and electron (r), electron mass (m_e), speed of light (c), and angle between scattered and incident beam (φ) as shown in Equation 2.5. [63-65]

$$I_e = I_0\left(\frac{e^4}{r^2 m_e^2 c^4}\right)\left(\frac{1+\cos^2\varphi}{2}\right) \tag{2.5}$$

Electrons may also scatter X-rays based on the Compton effect that involves treating an incident X-ray beam as a collection of photons each with energy (h_{v1}). Compton Modified Scattering (CMS) occurs when photons collide with electrons in a manner similar to billiard balls and photons deflect away from the collision at an angle. During collision, some kinetic energy from each photon is transferred into each electron encountered; meaning kinetic energy of each photon after impact (h_{v2}) will be less than h_{v1}. Since there is a difference in photon energy, there is a difference in wavelength between incident beams and CMS beams. As a result, CMS beams are not fixed phase related to their incident beams; and therefore, can not take part in coherent (constructive) scattering because CMS beams produce no interference. In the quantum theory of scattering, coherent scattering occurs only when an electron is so tightly bound it receives no momentum from photon impact, as in an atom. Since the electron receives no momentum ($h_{v1} = h_{v2}$), incident and scattered beams have identical wavelengths and diffraction may occur.[63-65]

When dealing with an atom, each electron in the atom coherently scatters part of the incident X-ray beam. The nucleus does not take part in coherent scattering because it cannot appreciably oscillate due to its extremely large mass compared with electrons. Based on the Thompson equation (Equation 2.5), coherent scattering is inversely proportional to scattering particle mass squared; meaning electrons will contribute much more significant coherent scattering than the nucleus. Therefore, scattering intensity of an atom is directly related to the atom's atomic number (Z), which is a measure of electrons within an atom. An atom's scattered wave is a combination of all scattered waves produced by component electrons within the atom. As the angle between an incident beam and an atom changes, scattering waves produced by individual electrons will become more or less out of phase, changing the intensity of the atom's coherently scattered wave.[63-65]

Much as scattered waves produced by atoms are a combination of scattered waves produced by each atom's electrons, scattered waves produced by crystals are a combination of scattered waves produced by its atoms. Periodic arrangement of atoms within a crystal severely limits coherent scattering to definitive directions and beams produced by scattering from crystals are referred to as diffracted beams. XRD determines phases present within a material by detecting constructive interference within diffracted beams created by varying the angle at which X-rays interact with a sample. Constructive interference is created at a diffraction angle (θ) or interplanar spacing (d) solving the Bragg equation shown in Equation 2.6. Diffraction angles are only related to the interplanar spacing and are a direct function of unit cell size and shape for a specific phase at a given wavelength (λ) of X-rays. The crystal plane that X-rays interact with during diffraction is denoted by an integer (n). [9, 62-64]

$$n\lambda = 2d\sin\theta \tag{2.6}$$

Since each crystalline phase has its own characteristic unit cell with a specific shape and dimensions, it is possible to identify phases by the pattern of constructive interference created during exposure to X-rays at various angles. Periodic arrangement of atoms within a crystal causes destructive interference of scattered waves under all conditions not satisfying Bragg's Law. However, atomic position within a unit cell affects diffracted beam intensity but not direction; meaning atomic positions can only be determined by diffracted intensities. Therefore, it is not surprising the crystal imperfections may cause measurable diffraction at non-Bragg angles. Since imperfections tend to be slight compared with overall lattice regularity, resultant diffracted beams are confined to narrow angular ranges and are centered at angles satisfying Bragg's law. [9, 62-64]

Amorphous materials are characterized by an almost complete lack of periodic structure, tendency for atoms to tightly pack together, and preference for a particular interatomic distance. As a result, diffraction patterns for amorphous phases generally only display nothing more than one or two humps in the baseline of the diffraction pattern. The presence of such broadened maxima may indicate the presence of an amorphous, or semi-crystalline phase.[9, 62-64]

Preferred orientation occurs when the distribution of crystal orientations is nonrandom and is a very common condition, especially when dealing with polycrystalline solids. In most cases, preferred orientation is the rule rather than the exception because preparation of an aggregate with completely random orientation of crystals is difficult. Some XRD machines have

been fitted with rotating stages to reduce preferred orientation effects within final diffraction patterns. Usually, reasonable care in sample preparation will produce a diffraction pattern with diffraction lines in correct order of decreasing intensity. However, errors in Powder Diffraction Files (PDFs) due to preferred orientation are a much more serious problem because the errors may lead to mistaken identifications of phases. "Starred" PDF patterns provide highest confidence for identification of phases and should be used, when available, to identify phases within experimental patterns.[62-64]

Every phase produces a characteristic XRD pattern independent of whether the material is in a pure state or a constituent in a multi-phase substance and XRD is a method of chemical and phase analysis. Analysis of a multi-phase substance requires knowledge of chemistry of the multi-phase system and some knowledge of phase equilibria of its constituents. Qualitative and quantitative analyses of phases present in multi-phase substances are possible with XRD. Qualitative analysis may be accomplished by identification of peaks corresponding to a known PDF. Quantitative analysis relies on relationships between intensity of diffraction lines for one phase and proportion of the phase within a multi-phase substance. XRD quantitative analysis depends heavily on X-ray absorption characteristics of constituents within a multi-phase substance. If their absorption coefficients are equal, then direct comparison of experimental intensities with PDF intensities may be used to determine weight fraction of each constituent.[62-64]

2.2.4.3 Surface Area Determination

One common method for measuring surface area of a material relies on adsorption of a gas onto a material's surface. The number of gas molecules in an adsorbed monolayer on a material's surface and cross-sectional area of adsorbed gas molecules may then be used to determine total surface area of the material. Therefore, calculation of surface area by gas adsorption depends heavily on the ability to predict the number of gas molecules required to create an exact monolayer on a material's surface. Most instruments for determining surface area use advanced software to predict the number of adsorbed molecules required to accurately cover a material's entire surface and consequently its surface area. Based on similar principals, software may be used to determine pore diameter and volume.[9, 62]

2.3 Green Body Formation

This section discusses formation of a green ceramic body from powder particles by uniaxial pressing, isostatic pressing, and slip casting. For commercial production, higher green densities are preferred because less time at densification temperature is required to produce high density parts. Each forming method has disadvantages and determination of which method to use depends on availability of equipment, desired use of a final part, expense of machining, and ability to perform the method.[9, 13, 14, 29]

Uniaxial pressing uses force applied to parallel platens to compact powders within a forming die as shown in Figure 2.5. Force applied to a powder compact is along one direction of the compact. Uniaxial pressing is useful for creating simple shapes. The appeal of uniaxial pressing is the ease for forming a powder compact. Depending on the materials being pressed, a binder may be required to help hold the compact together.[9, 13, 14, 29]

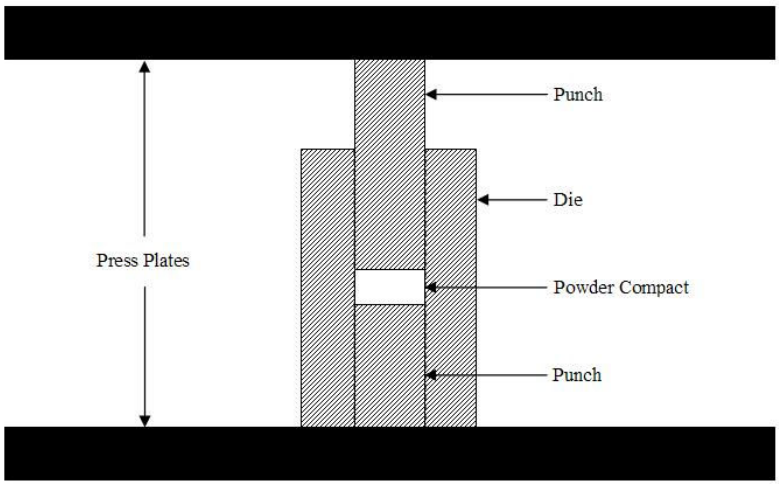

Figure 2.5 – Setup for uniaxially pressing a powder compact using a punch and die set.

During compaction, residual stresses build within a powder compact and result in a dimensional relaxation or springback. Vertical springback during pressing is not a major issue when using automated press equipment as it is much easier to maintain a constant compact pressure until ejection. In manual hydraulic pressing, vertical springback may manifest itself as a drop in peak pressing pressure when allowed to sit at maximum pressure. Horizontal springback generally occurs shortly after ejection of a powder compact from a die. Springback increases with higher pressing pressure and may cause fracture and delamination within a compact during ejection.[9, 13, 14]

Isostatic pressing uses force applied in all directions within a forming mold or pattern to produce high density net-shape bodies. Isostatic presses rely on pressurization of a fluid surrounding a mold to create pressure in every direction. Isostatic pressing may be performed cold (Cold Isostatic Pressing – CIP) or with heat applied (Hot Isostatic Pressing – HIP). CIP will produce a green body, which must then be heat treated to achieve theoretical or near theoretical density while HIP will produce a theoretically or near theoretically dense final body. Isostatic pressing allows for formation of very complex shapes but requires complex mold design and expensive equipment.[9, 13, 14, 29]

Slip casting is a method for producing complex shapes from many ceramic-based materials. A slip is a colloidal suspension of powders within an immiscible liquid. Slip is cast by pumping or pouring slip into a permeable mold. Capillary suction forces pull liquid from the slip into the mold and leaves behind a densely packed layer of particles on mold walls. Drain casting and solid casting are two common methods for slip casting and involve casting for a specified time period then draining off all excess slip (drain casting) or continually adding slip until a solid cast is made (solid casting). Slip casting is generally limited by design and production of a casting mold or creation of a slip for casting.[9, 13, 14, 29]

2.4 Design of Experiments (DOE)

This section covers principals behind DOE including fundamentals, methodology, analytical tools, and prediction of response function. DOE is often used in industrial experimentation but may be easily modified for laboratory experimentation. In industrial settings, experiments are conducted in a series of tests producing some quantifiable output to aid in improvement of product or process quality. In laboratory environments, experiments are performed to understand data from a process, determine effects of process variables on output performance, and verify predicted results obtained from experimentation. Understanding relationships between input variables (factors) and output performance (quality) is of great interest in most cases.[66, 67]

It is common for engineers and scientist to employ One Variable At a Time (OVAT) experimentation where all factors are fixed except the one being tested. OVAT experimentation provides a limited amount of process data and may consume large quantities of resources. In DOE, changes are made to multiple factors and quality is analyzed to determine relationships between individual factors and quality. Not all factors will affect quality equally; some may

have strong influences, some medium influences, and others no influence at all on quality. An interaction occurs when varying levels of one factor changes the effect of another factor on quality and cannot be tested using OVAT experimentation.[66, 67]

The primary objective of DOE is understanding which factors in a process affect quality most and then determine what levels of each factor will produce highest quality results. DOE requires many skills including planning, statistical, teamwork, and engineering skills. Planning skills are required for determining significance of experimentation, time, and budget required for an experiment. Statistical skills are required to adequately analyze experimental data, assigning factors and factor interactions in the experimental layout, interpretation of experimental results, and for making appropriate decisions for improvement. Team work skills are important when an experiment is being conducted by more than one person. Communication is an important part of team work skills and is vital in ensuring each team member understands experimental objectives and goals to be completed. Engineering skills are needed to determine an appropriate number of factors and levels to test, range for variation of each factor, and what factors can and cannot be controlled during experimentation.[66, 67]

2.4.1 Design of Experiments Fundamentals

This section covers basic principals of design of experiments including randomization, replication, blocking, Degrees Of Freedom (DOF), confounding, design resolution, selection of Quality Characteristics (QC), and factorial design. DOE is a process of planning, designing, and analyzing a series of experiments to efficiently draw valid and objective conclusions. Implementation of statistical methods into experimental design methodology ensures conclusions drawn from an experiment are statistically sound.[66, 67]

In DOE, two primary types of factors exist: qualitative and quantitative. Qualitative factors are discrete in nature and would include manufacturer of raw material, type of wire used, pressing configuration, etc. Quantitative factors involve ranges of quantifiable settings and must be measured and controlled during experimentation. For DOE, a level is a specified value of an individual factor being examined during experimentation. Each factor may have different levels based on the factors nature as qualitative or quantitative; but quantitative factors tend to be capable of more levels than qualitative factors. A trial is a specific combination of factor levels whose effect on quality is of interest.[66, 67]

Principles of DOE such as randomization, replication, and blocking help improve experimental efficiency. Each is an effective tool in reducing or removing experimental bias caused by process warm-up, differences in experimenters, or system instability. Large experimental bias may lead to an incorrect understanding of factor significance and wrong optimal setting determinations.[66, 67]

2.4.1.1 Randomization

Randomization is a method used by experimenters to reduce effects of experimental bias by randomly selecting the order in which trials will be performed. Randomization averages out effects of noise directly attributed to a process by giving all levels of a factor an equal chance of being effected by process noise effects. If experimentation is performed on a completely stable process, then randomization is unnecessary. However, if a process is unstable, then randomization is required to ensure experimental results are not meaningless or misleading. Experimentation on very unstable systems may make randomization impossible, in which case, efforts should be made to bring the process into statistical control before any further experimentation is performed. A classical DOE approach uses complete randomization of experimental trials while Taguchi's approach to experimentation incorporates noise factors into the experimental layout and does not require randomization.[66, 67]

2.4.1.2 Replication

Replication is repetitious performance of an entire experiment or a portion of an experiment under more than one condition. Replication allows a researcher to estimate experimental errors and to more precisely estimate factor and interaction effects. Factor or interaction effects may be insignificant based on experimental error and low replicate numbers would make it impossible to make conclusions about factor and interaction effects on quality. Substantially increased time and material costs are required for replication and should be considered when deciding replication requirements for an experiment.[66, 67]

2.4.1.3 Blocking

Blocking is used to remove effects of variations from noise factors improving overall efficiency of experimental designs. Similar trials may be arranged into groups (or blocks) and run all together to eliminate unwanted sources of variability. Any observations made under identical experimental conditions are considered part of a block. Variability between blocks may be eliminated from experimental error leading to increased precision of an experiment.[66, 67]

2.4.1.4 Degrees of Freedom

According to statistics, DOF are the number of independent fair comparisons possible from a set of data. For DOE, a variable's DOF is equal to its number of levels minus one. For an entire experiment, it is equal to the total number of data points minus one. When dealing with interactions, DOF is equal to a product of DOF for each factor of the particular interaction.[66, 67]

2.4.1.5 Confounding and Design Resolution

Confounding is a combining influence from multiple factor effects into a single measured effect. An example of confounding is factor effects (A and B) and the interactions of factors (AxB) are incapable of independent estimation. Another name for confounded effects is aliases. An alias structure is a list of confounding effects occurring in a particular experimental design and is also referred to as a confounding pattern.[66, 67]

Design resolution is a method for summarizing amounts of aliasing inherent with an experimental design. Aliasing amounts between main effects and interaction effects are represented by the resolution of a particular experimental design. Design resolution is a key tool in deciding selection of a fractional factorial design. It is desirable to have a design of resolution III or higher for a designed experiment. A resolution III design means no main effects are confounded with any other main effect; but, interactions are confounded with each other and main effects are confounded with two factor interactions. A resolution IV design means no main effects are confounded with other main effects or two-factor interactions but interactions are confounded with each other. In a resolution V design, no main effects are confounded with any other main effects, two factor interactions, or three factor interactions but two factor interactions are confounded with three-factor interactions.[66, 67]

2.4.1.6 Selection of Quality Characteristics

Vital to success of any designed experiment is selection of an appropriate QC. To determine a solid QC it is necessary to begin with engineering and economic goals of the experiment. After identifying goals, it is important to identify any fundamental mechanisms or physical laws affecting the goals. A QC should be chosen based on an ability to increase understanding of the mechanisms and physical laws. Ideally, QCs should be easy to measure with precision, accuracy, and stability and should cover all aspects of a process input-output relationship. In addition, QCs should be additive (meaning no interaction exists between them) and monotonic (meaning regardless of factor settings each factor's effect on robustness should

be in a consistent direction). Every reasonable effort should be made to collect data relating an engineering function rather than a symptom of variability.[66, 67]

2.4.1.7 Factorial Design

Factorial designs are a method for researchers to determine joint effects of factors on a quality characteristic. In experimental design, it is most common to use either full or fractional factorial designs with two or three levels to setup an experiment. A full factorial design contains every possible combination of factors and levels and assumes, for factors at two levels, QC response is linear over a chosen range of factor levels. Full factorial designs often require a large amount of time and resources to complete.[66, 67]

Fractional factorial experiments are an alternative to be considered when researches do not have adequate time, resources, or budget to complete a full factorial experiment. A fractional factorial experiment may be used to obtain data on main effects and two-order interactions in a fraction of experiments required by a full factorial experiment, if it can be reasonably assumed the higher order interactions are not important. A fractional factorial design uses an orthogonal array to allow researcher to study main effects and interactions in a minimum number of trials. Examples of full and fractional factorial arrays may be found in Appendix A.[66, 67]

2.4.2 Design of Experiments Methodology

This section covers a methodology for DOE and gives detailed insight into each of its stages. The methodology is divided into four stages: planning, designing, conducting, and analyzing. There are many variations on DOE methodology; however, most follow the same four stages.[66, 67]

2.4.2.1 Planning Stage

The planning stage focuses on determination of a problem, selecting an appropriate QC, selection and classification of factors, choosing factor levels, and deciding which interactions to study. Recognizing a problem within a process and succinctly stating what the problem is creates a better understanding of what to study during experimentation. A problem statement should be specific, measurable, and yield some practical value.[66, 67]

Selecting an appropriate QC is critical to success of any designed experiment. QCs may be variable or attribute responses but variable responses such as density and strength provide more information than attribute responses like pass/fail. Variable QCs tend to have similar levels of statistical significance as attribute QCs but requiring fewer samples.[66, 67]

Selection of factors and design parameters is a very important part of planning a designed experiment and should be based in engineering knowledge of a process, historical data, cause and effect analysis, and extensive brainstorming. Results of an experiment may not be as accurate or useful for improving a process if important factors are not included in experimentation. Each factor identified should be categorized as controllable or uncontrollable. Controllable factors can be controlled by a researcher in a laboratory environment. Uncontrollable (noise) factors are difficult or expensive to control and may have immense impact on process variability. The noise factors must not be ignored if enhanced understanding of a process is to be gained. Randomization, replication, and blocking may be used to minimize effects of uncontrolled factors on QCs.[66, 67]

A level is a value held by a factor during an experiment and depends on the nature of the factor as qualitative or quantitative. In early phases of experimentation, two levels are usually appropriate for quantitative factors. However, more than two levels may be required for qualitative factors depending on what quality is being varied. Three or more levels should be used for any factor believed to have a non-linear relationship with its QC.[66, 67]

Interaction between factors is common in experimentation and should be taken into consideration when planning a designed experiment. Having a good understanding of interactions between factors may be important for effective interpretation of experimental results. In DOE, two order interactions are generally studied while third or higher order interactions are rarely considered. Most two factor interactions do not need to be studied during initial phases of experimentation. Selection of experimental size will be largely dependent on the number of factors and interactions which are of interest.[66, 67]

2.4.2.2 Designing and Conducting Stages

The designing stage is used to determine the most appropriate design for experimentation and creation of an experimental design matrix. Statistical experiment designs tend to be based on a classical approach developed by Sir Ronald Fisher or an orthogonal array approach developed by Dr. Genichi Taguchi. Experimental size, budget, time, and resources should all be considered in selection of a design approach. Confounding structure and design resolution are also very important to consider when designing an experiment.[66, 67]

The conducting stage is where a designed experiment is carried out and results are evaluated. Prior to execution of any experiment it is important to select a suitable location with

as few noise factors as possible, to determine availability of necessary resources, and to determine viability of each action in terms of time, cost, and benefit. It may also be necessary to conduct an evaluation to verify an experiment is the only possible solution for a particular problem or benefits gained from experimentation will exceed experimental costs.[66, 67]

To ensure experiments are performed according to a prepared experimental design matrix it is important for the primary researcher be present throughout experimentation. It is best to perform experimentation with identical personnel for each trial but the presence of the primary researcher should help reduce variability due to different operators. Monitoring each experimental trial should help find any discrepancies occurring during an experiment. If a discrepancy is found, then the experiment should be stopped immediately and should not be repeated until all sources of discrepancy have been corrected. It may also be helpful to have a prepared data sheet or computer present for recording observed values so a permanent record exists for each experiment.[66, 67]

2.4.2.3 Analyzing Stage

After all experiments have been performed, analysis and interpretation of results should be performed so valid conclusions may be determined. During the analyzing stage it should be possible to determine which factors affect selected QCs and performance variability. It is also possible to determine optimum level settings to maximize performance of a system or process. Based on a complete analysis of collected experimental data, it is possible to determine whether further improvements to a process are possible, which may lead to further experimentation.[66, 67]

2.4.3 Analytical Tools

This section covers some statistical tools including main effect plots, Pareto plots, normal probability plots, and Analysis Of Variance (ANOVA) may be used to analyze and interpret data from a designed experiment. Each of the tools may be used to determine valid conclusions on which factors affect a QC from a process. Employment of multiple statistically based analytical tools helps to ensure confidence in analysis and interpretation of results from a designed experiment.[66, 67]

2.4.3.1 Plotting Techniques

A main effect plot graphically displays a factor's mean response value at each level tested. Main effect plots may be used for comparison of relative effect strengths of various factors. Each main effect plot's sign determines if the average response value increases or

decreases as factor levels are changed; and magnitude provides insight on a factor's effect strength. If a factor effect is positive, then average response will increase with increasing level; but if a factor effect is negative, then average response will decrease with increasing level. Factor effects (E_f) may be calculated by subtracting average response at low level (F_1) from average response at high level (F_2) as shown in Equation 2.7.[66, 67]

$$E_f = F_2 - F_1 \tag{2.7}$$

Pareto plots allow for detection of which factor and interaction effects are most important to a process for optimization. Each plot displays absolute values of effects and a reference line is created on the plot. Any effect extending beyond the reference line is a potentially important factor for process optimization. Pareto charts should be checked against a Normal Probability Plot (NPP). For NPPs, main effects and interactions are plotted against calculated cumulative probability percents. Inactive effects form an approximately straight line while active or important effects are displayed as extreme or outlying plot points and are statistically significant. A factors significance level in DOE is the probability than an observed effect is due purely to chance.[66, 67]

2.4.3.2 Analysis of Variance

ANOVA is a mathematical representation of effect plots relying on a Sum of Squares (SS) of collected data and DOF (ν) to determine variance (V) in quality due to a change in factor level. ANOVA may be used to determine what factors are responsible for variations in quality during a process and relies on the statistical F-test. Many calculations are required for ANOVA but spreadsheets or programs may be used to reduce time required for calculation and analysis.[66, 67]

A total SS (SS_T) may be calculated by squaring each observation (y_i), adding all squared terms together, and subtracting the sum of all observations (T) squared divided by the total number of observations (N) as shown in Equation 2.8. A SS term may be calculated with a sum of observations under a factor and level (A_i), total number of observations under each factor and level (n_{Ai}), T, and N as shown in Equation 2.9. Additionally, a sum of observations under each configuration (AxB_i), a total number of observations under each configuration (n_{AxBi}), and a total number of interactions observed (r) are required to calculate a SS of an interaction as shown in Equation 2.10. Since a total SS for a designed experiment is unable to separate out error effects

from factor effects, a SS for experimental error may be calculated by subtracting SSs of all factors and interactions from SS_T as shown in Equation 2.11.[66, 67]

$$SS_T = \sum_{i=1}^{N} y_i^2 - \frac{T^2}{N} \tag{2.8}$$

$$SS_A = \frac{A_1^2}{n_{a1}} + \frac{A_2^2}{n_{a2}} + \frac{A_3^2}{n_{a3}} + \ldots - \frac{T^2}{N} \tag{2.9}$$

$$SS_{A\times B} = \left[\sum_{i=1}^{r} \frac{(A\times B)_i^2}{n_{(A\times B)_i}} \right] - \frac{T^2}{N} - SS_A - SS_B \tag{2.10}$$

$$SS_e = SS_T - SS_A - SS_B - \ldots - SS_Y - SS_Z - SS_{A\times B} \ldots - SS_{Y\times Z} \tag{2.11}$$

Total DOF (ν_T) is calculated by subtracting one from the total number of observations as shown in Equation 2.12. DOF for a factor (ν_A) may be calculated by subtracting one from a factor's total number of levels (K_A) as shown in Equation 2.13. For an interaction, DOF (ν_{AxB}) is equal to a product of each factor's DOF as shown in Equation 2.14. DOF due to experimental error (ν_e) is calculated by subtracting all factor and interaction DOF from the total DOF as shown in Equation 2.15.[66, 67]

$$\nu_T = N - 1 \tag{2.12}$$

$$\nu_A = K_A - 1 \tag{2.13}$$

$$\nu_{A\times B} = \nu_A \cdot \nu_B \tag{2.14}$$

$$\nu_e = \nu_T - \nu_A - \nu_B - \ldots - \nu_Y - \nu_Z - \nu_{A\times B} - \ldots - \nu_{Y\times Z} \tag{2.15}$$

After all DOFs have been calculated, variance due to a factor (V_A) may be calculated by dividing a factor's SS by its DOF as shown in Equation 2.16. Variance due to an interaction (V_{AxB}) may be calculated by dividing an interaction's SS by its DOF as shown in Equation 2.17. Variance due to experimental error (V_e) may be calculated by dividing SS due to error by its DOF as shown in Equation 2.18. F-values are then easily calculated by dividing individual factor and interaction variance by variance due to experimental error as shown in Equations 2.19 and 2.20. Calculated F-values may be compared with published F-tables to determine a confidence level for significance of a factor or interaction.[66, 67]

$$V_A = \frac{SS_A}{\nu_A} \tag{2.16}$$

$$V_{A\times B} = \frac{SS_{A\times B}}{\nu_{A\times B}} \tag{2.17}$$

$$V_e = \frac{SS_e}{\nu_e} \tag{2.18}$$

$$F_A = \frac{V_A}{V_e} \tag{2.19}$$

$$F_{AxB} = \frac{V_{A\times B}}{V_e} \tag{2.20}$$

It is important to remember the variance for any factor or interaction is a combination of true variation due to a factor or interaction and variation due to error. In order to provide a more accurate representation of SS, it is common to calculate the pure sum of squares (SS') using Equation 2.21. After calculating SS', it is possible to determine percent contribution (P) or how much each factor contributes to total quality response using Equation 2.22. An example using ANOVA calculations may be found in Appendix B.[66, 67]

$$SS'_A = SS_A - V_e \cdot \nu_A \tag{2.21}$$

$$P = \frac{SS'_A}{SS_T} \times 100 \tag{2.22}$$

2.4.3.3 Error Pooling

Error pooling is a method for dealing with potentially insignificant main factors and interactions by lumping them together into one error term. If error pooling is used, then SS_T is simply a summation of all SS values for all factors and interactions tested and SS_e becomes a summation of all SS values for potentially insignificant factors and interactions. There are two main methods for pooling error: pooling down and pooling up.[67]

Pooling down means all factors and interactions except the one with largest SS value are pooled into error, F-values for the factor or interaction are calculated, and then calculated values are compared with F-table values to determine significance of the factor or interaction. If the factor or interaction is found to be significant than the factor or interaction with next largest SS

value is considered and the process is repeated until a factor is found to be insignificant. When pooling down, it is more likely a factor will be deemed insignificant when it actually is significant to controlling a quality characteristic.[67]

Pooling up means the factor with smallest value of SS is pooled into error and all remaining factors and levels are tested for significance. If factors are still found to be insignificant, then the factor with next smallest SS is pooled into error and pooling continues until all remaining factors are found to be significant. When pooling up it is more likely a factor will be deemed significant when it is actually insignificant to controlling a quality characteristic. Examples of error pooling may be found in Appendix B.[67]

2.4.4 Predicting Response Function and Confirmation Experiment

Regression modeling may be used to predict QC response to various combinations of factors and levels. Predicted Response (PR) calculations are based on a summation of average QC response at each selected combination of factors and levels (A_i term from Equation 2.9) minus the average QC response for all factors and levels ($\overline{T}$) as shown in Equation 2.23. Based on PRs calculated using Equation 2.23, it is possible to estimate which configurations will have the best or worst QC response.[66, 67]

$$PR = \overline{A_i} + \overline{B_i} + \ldots\overline{A \times B} - 2\overline{T} \tag{2.23}$$

After PR has been calculated, it is important to run a confirmation experiment to confirm predictions, validate the response model, and confirm an understanding of the process being studied. Multiple confirmation trials are often run with the best QC response predicted configuration. After confirmation trials have been performed an average QC response is calculated but it is also important to calculate Confidence Intervals (CIs) for the average QC response. CIs are a measure of variation around PR based on control of factors used for calculating PR. Mean QC response from confirmation trials ($\overline{y}$), Standard Deviation (SD) of confirmation trials, and number of tests run under predicted optimum conditions (n) are required to calculate CIs at a 99% confidence limit for a PR as shown in Equation 2.24.[66, 67]

$$CI = \overline{y} \pm 3\left(\frac{SD}{\sqrt{n}}\right) \tag{2.24}$$

2.5 Modeling of the Densification Process

This section explains how models may be used to determine Sintering Time Constants (STCs) and effects of a second phase on densification of a composite. Using models before performing experimentation may provide information about what may be expected from experimentation. Several models of powder compact densification have been developed. Models for determining STCs, the effect of a second phase on densification, diffusion mechanism, and activation energy may be very important in understanding densification behavior of CMCs.[15, 16]

2.5.1 Determination of Sintering Time Constants

The time required to achieve full density by sintering of a materials system is known as the "sintering time constant." An STC is determined by plotting the natural logarithm of one minus densification factor ($\Delta\rho_f/\Delta\rho_{max}$) versus heat treatment time (t), then calculating the slope. An example of a plot used to calculate STCs is shown in Figure 2.6.

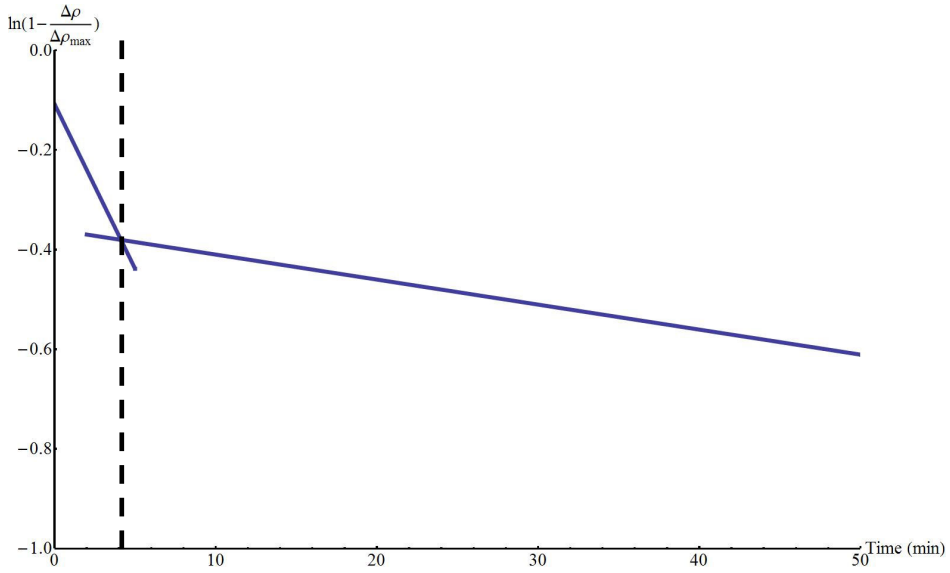

Figure 2.6 – Example of an STC curve showing two time constants with a change in slope at ~ 4 minutes.

According to Bordia and Raj, STCs are based on size of pores, spacing between pores, and diffusion rate required to fill pores in a compact; therefore, it is probable for a material's time constant to change during densification. As a result, multiple time constants are possible and the time constant with lowest value of densification factor will dominate. Changes in densification rate may be linked to different stages of densification for a ceramic; and, therefore,

changes in STC may correlate to changes in densification stage. The sintering equation yielding STCs is shown in Equation 2.25.[68]

$$1 - \frac{\Delta\rho_f}{\Delta\rho_{\max}} = e^{-t/\tau} \tag{2.25}$$

The term $\Delta\rho_f$ is change in density of a ceramic from its green state to its final state (after heat treatment) while $\Delta\rho_{max}$ is change in density from its green state to its fully (theoretically) dense state. For Equation 2.25, heat treatment time is defined as t and STC is defined as τ. The expression on the left side of Equation 2.25 represents a densification factor.[68]

2.5.2 Ceramic Matrix Composite Sintering

A model of the sintering of CMCs was developed by Raj and Bordia. Raj and Bordia's model incorporates volume fraction of a reinforcement phase (f), STC (τ), heat treatment time (t), densification factor ($\Delta\rho_f/\Delta\rho_{max}$), and a parameter based on effect of inhomogeneities on sintering behavior (β) as shown in Equation 2.26. The β-parameter provides insight into the effect of the reinforcement phase on the densification of the matrix.[68]

$$\frac{\Delta\rho_f}{\Delta\rho_{\max}} = 1 - \exp\left(-\frac{9\beta}{4f + 9\beta}\frac{t}{\tau}\right) \tag{2.26}$$

According to Raj and Bordia, if $\beta > 1$, the sintering behavior adheres to the composite rule of mixtures and STC remains unchanged. On the other hand, if $\beta < 1$, then the sintering rate may be considerably slower than the rate determined by the rule of mixtures. As β approaches zero, sintering slows and essentially stops when β is very close to zero. However, as β approaches infinity, the composite behaves similarly to its matrix material as if no reinforcement phase were present. Plotting densification factor ($\Delta\rho_f/\Delta\rho_{max}$) versus heat treatment time over time constant (t/τ) for various values of β for a composite of given volume fraction clearly shows the concept as shown in Figure 2.7.[68]

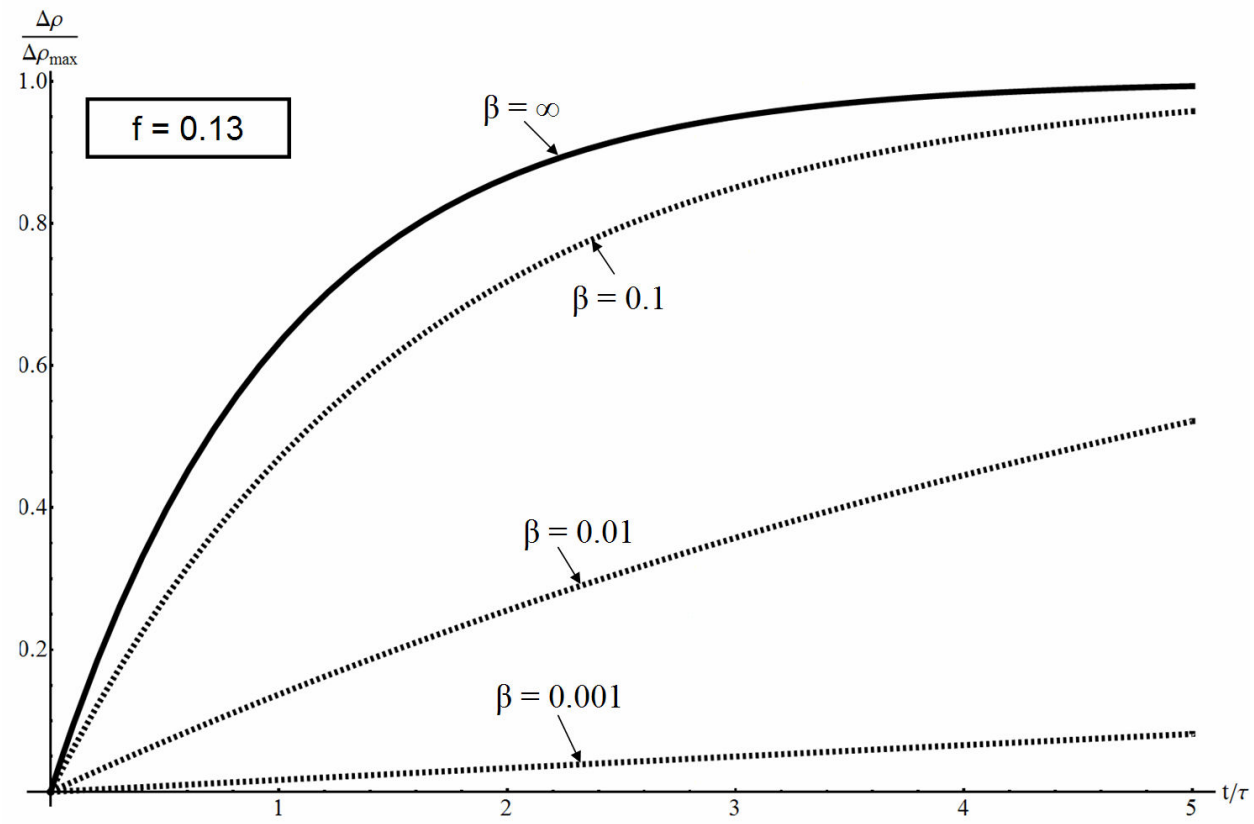

Figure 2.7 – An example plot demonstrating the effect of the beta factor on densification.

In Al_2O_3/TiB_2 composites TiB_2 is considered a reinforcement phase and in sintering TiB_2 is limited by low self diffusion of Ti and B, as well as, covalent bonding and high melting temperature. Sinterability of TiB_2 seems to be hindered severely by oxides that may be present during densification and often sintering aids must be employed to densify TiB_2 at temperatures below 2000°C. Based on TiB_2's limitations in sintering it is probable β will not approach infinity for Al_2O_3/TiB_2 composites.[5, 21, 31, 57, 69-71]

2.6 Densification by Diffusion

This section includes information on mass transport, effect of chemical reaction on diffusion, and microstructure considerations. Diffusion of species within a powder compact is the means for densification in most ceramic systems. One driving force for densification is reduction of surface and interfacial energy within a material system. Reduction in energy is generally achieved by reducing or eliminating the chemical potential gradient within a material system. A material system's preferred state is one with the least amount of surface and interfacial energy for a given temperature and pressure. Transport of material towards pores in a

powder compact is a primary mechanism for volume reduction or shrinkage. A reduction in sample volume without reduction of sample mass results in an increase in sample density making volumetric shrinkage a reasonable measurement technique for densification.[9, 13, 14, 61, 72-77]

2.6.1 Mass Transport

Diffusion is a kinetic process usually leading to homogenization of chemical components within a phase. Diffusion in solids is observed on atomic or molecular length scales only. During diffusion, chemical homogeneity increases with time until all phases have reached thermodynamic equilibrium at which point diffusion stops altogether. Several parallels exist between treatments of heat transport and mass transport; however, numerical calculations of mass transport are severely limited by availability of diffusion data.[75-77]

Diffusion laws are mathematical relationships relating diffusion rates to gradients responsible for net mass transfer. A vector form of Fick's first law relates mass flux (**J**) to a concentration gradient (∇C) by a diffusion coefficient (D) as shown in Equation 2.27. However, the form of Fick's law in Equation 2.27 uses concentration gradient as an approximation of chemical potential gradients as a primary driving force for diffusion. In certain cases, like "uphill" diffusion, the use of an expanded form of Fick's first law may be needed. In the expanded form of Fick's first law, mass flux of a species ($\mathbf{J}_i$) may be more appropriately expressed as a function of local concentration (C_i), molar mobility tensor ($\{\mathbf{B}_i\}$), and chemical potential gradient as a function of position ($\nabla\mu_i(\mathbf{r})$) as shown in Equation 2.28. Densification by sintering relies on mass accumulation in pore spaces during diffusion. Mass accumulation rates at any point in a material may be thought of as total mass inflow minus total mass outflow for a point within the material.[75-77]

$$\mathbf{J} = -D\nabla C \tag{2.27}$$

$$\mathbf{J}_i = -C_i\{\mathbf{B}_i\}\cdot\nabla\mu_i(\mathbf{r}_i) \tag{2.28}$$

2.6.2 Effect of Chemical Reaction on Diffusion

For fundamental diffusion, chemical reactions and other processes are ignored to simplify calculations of mass transport. Diffusion-reaction removes assumptions about diffusants being immutable in regard to chemical processes (such as phase change) and adds complexity to transport kinetics. Diffusional transport through materials at elevated temperatures may result in reaction with a material's bulk or surface.[75-77]

The rate controlling step in diffusion-reaction processes is generally either diffusion limited or reaction-limited.[76] If a diffusion-reaction process is reaction limited in a material, then the concentration throughout the material's bulk will remain constant; however, if the process is diffusion controlled or mixed controlled, then the concentration through the material's bulk will vary. Diffusion fields for steady state linear flow by mixed diffusion-reaction processes may be described in terms of concentration at a starting position (C_0), concentration at fixed second position (C_2), defined diffusion length (l), and distance from starting position (x) as shown in Equation 2.29. Steady state mass flux (J_{ss}) may be expressed in terms of an equilibrium concentration (C_{eq}), reaction velocity (α), D, C_0, and l as shown in Equation 2.30.[75-77]

$$C(x) = C_0 + \frac{C_2 - C_0}{l} x \tag{2.29}$$

$$J_{ss} = \alpha \frac{C_0 - C_{eq}}{1 + \alpha l / D} \tag{2.30}$$

The dimensionless quantity αl/D is known as the Péclet number (Pe) and may be thought of as a ratio of reaction velocity to diffusion speed (D/l); or, as a ratio of physical thickness to a characteristic diffusion length (D/α) as shown in Equations 2.31 and 2.32. Different problems may favor a velocity approach over a length approach and vice versa. When Pe is small (Pe<<1), reaction-diffusion is considered to be reaction limited and may be approximated by Equation 2.33. In the reaction limited case, mass flux leaving a material's surface is independent of diffusivity and is not determined by diffusional transport. When Pe is large (Pe>>1), reaction diffusion is considered to be diffusion limited and is approximated by Equation 2.34. In the diffusion limited case, mass flux is proportional to diffusivity and concentration gradient; meaning mass flux no longer depends on reaction velocity.[75-77]

$$Pe \equiv \frac{\alpha}{D / l} \tag{2.31}$$

$$Pe \equiv \frac{l}{D / \alpha} \tag{2.32}$$

$$J_{ss} \cong \alpha\left(C_0 - C_{eq}\right) \tag{2.33}$$

$$J_{ss} \cong \frac{D\left(C_0 - C_{eq}\right)}{l} \tag{2.34}$$

Between reaction and diffusion limits exists an intermediate region known as mixed kinetics, which occurs when Pe is on the order of one. Therefore, steady state diffusion for diffusion-reaction processes may be generally represented by Equation 2.35. In mixed kinetics both diffusion coefficient and reaction velocity significantly affect mass transport. However, Pe still determines the relative importance of volume diffusion versus surface chemical reaction.[75-77]

$$J_{ss} = \frac{\alpha\left(C_0 - C_{eq}\right)}{1 + Pe} \tag{2.35}$$

2.6.3 Microstructure Considerations

Full thermodynamic equilibrium in a microstructure containing two or more phases would contain massive phase domains, large length scales for each domain, and a minimum of interfacial area to achieve a state of minimum free energy. However, in two phase crystalline materials, mass transport is primarily achieved by diffusion and full thermodynamic equilibrium is virtually never attained. Since diffusion is generally the rate limiting process for mass transport, phase separation in engineered crystalline materials tends to be below a few hundred micrometers in length scale.[75-77]

When fine grains of one phase (β) are dispersed in a matrix of a different phase (α) there is generally excess energy stored at the interfaces. The energy associated with α/β interfaces is typically less than 1% of initial free energy available for nucleation and phase growth.[76] However, reduction of α/β interfacial energy can be a primary driving force for total phase separation by phase coarsening and grain growth.[75-77]

Phase coarsening requires growth of large phase domains and shrinkage of smaller ones by diffusion. The gradual removal of smaller particles and growth of larger particle causes increases in dispersed phase particle size and decreases in total particle number. As size distributions of dispersed particles increase, the material's mechanical, electrical, and chemical properties will change.[75-77]

2.7 Microstructure Formation by Diffusion

This section covers some general diffusion mechanisms and information on solid, liquid, and gas phase diffusion mechanisms. There are several ways for matter to move through a powder compact during densification including volume (or bulk) diffusion, grain boundary diffusion, liquid phase diffusion, and evaporation-condensation. Diffusion mechanisms leading to densification are accompanied by compact shrinkage.[8, 78-85]

For the case of atom diffusion, interstitial diffusion is only possible if diffuser atoms are sufficiently small relative to host or lattice atoms. If diffuser atoms are significantly small, then it is possible for diffuser atoms to jump between interstitial sites and diffuse through a material. Resistance to lattice strain by bonds between lattice atoms is a major restrictive force for interstitial diffusion. As atomic radii ratios between diffuser and lattice atoms decrease, interstitial diffusion becomes more difficult. Maximum local in-plane or saddle-point strain (ε) may be approximated using in-plane lattice parameter (a_o), interatomic spacing (h), and diffuser atomic radius (d_i) as shown in Equation 2.36.[75-77]

$$\varepsilon = \frac{d_i - h}{a_o} \tag{2.36}$$

Probabilities for significant matter transport by interstitial diffusion are very low even for light atoms in very open lattices.[76] An energy barrier must be overcome before any diffusion process may begin. The energy barrier is known as activation energy and is generally dependent on atomic radii of diffuser and host lattice atoms, crystal structure, diffusion mechanism, and temperature. As diffuser atomic radii approach or exceed host lattice atomic radii, saddle-point strains become too large for interstitial diffusion to occur. Based on atomic radii, oxygen (O) and boron (B) are the most probable diffusants for interstitial diffusion contributing to mass transport in Al_2O_3/TiB_2 systems as shown in Table 2.5.[75-77]

Table 2.5 – Atomic Radii for Elements in Al_2O_3/TiB_2 Composites[86]

Element	Atomic Radius (pm)
O	48
B	87
Al	118
Ti	176

Ring diffusion is a cyclic exchange diffusion mechanism for similar-sized atoms. When compared with interstitial diffusion, ring diffusion decreases required local lattice distortions but increases the amount of necessary cooperative motion. As more atoms become involved in ring motion, elastic distortion energies decrease dramatically but required correlation of atom motions also increases. For ring groupings of four and larger it is highly unlikely for ring diffusion to occur due to lack of necessary cooperative motion. Cyclic exchange energetics required for ring diffusion are not favorable eliminating it as a primary mechanism for lattice diffusion.[75-77]

Lattice vacancies are considered the most important thermally induced equilibrium lattice defects in crystals and vacancy-assisted diffusion is an accepted mechanism for atomic diffusion in solids. At elevated temperatures, vacancy-assisted diffusion is the dominant diffusion mechanism for substantial atoms in close packed metals.[76] Distortion energy required for vacancy-atom exchange is larger than the required strain energy for interstitial diffusion; however, energy needed to dilate neighboring atoms is generally much less than the required energy for atomic movement from an equilibrium site to a vacant site. The low energy requirement for dilation of neighboring atoms compared to the energy required for atom movement to a vacant site means many more "window openings" occur than vacancy - atom pair exchanges in vacancy-assisted diffusion.[75-77]

Interstitialcy diffusion is a type of defect assisted diffusion exhibited in amorphous materials and some ionic crystals and requires a change in lattice coordination. A crowdion diffuser is an example of a displacement interstitialcy occurring in soft crystals along certain close-packed planes. The interstitialcy requires movement of several atoms in one direction through many locally distorted lattice positions and ends with all atoms in normal lattice positions after diffusion is complete. It is necessary for diffuser atoms not to be equal in size to the hosts for interstitialcy mechanisms to operate efficiently.[75-77]

2.7.1 Volume or Bulk Diffusion and Grain Boundary Diffusion

Volume or bulk diffusion is a common diffusion mechanism for densification of ceramics. Diffusion in the solid state may be thought of as "random" atom motion within a material's bulk. Diffusion is not a truly random process and depends on a driving force that is normally the chemical potential gradient within a material. However, when diffusion is considered as a "random" walk process, transport of atoms from one site to another may be very slow.[8, 9, 75-77, 79-81, 84, 87-89]

If volume diffusion is the RCDM, then mass transport of the diffusing species is fastest through the material's bulk. When volume diffusion is the RCDM, the microstructure of a heat treated ceramic should exhibit a clear and identifiable grain structure when observed using microscopy. When mass transport of diffusing species is fastest through grain boundaries then grain boundary diffusion is the RCDM. Grain boundary diffusion has been observed to dominate densification in many common ceramics including Al_2O_3 making it a very important diffusion mechanism. However, the microstructure accompanying densification by grain boundary diffusion looks very similar to the microstructure when volume diffusion is the RCDM.[8, 9, 75-77, 79-81, 84, 87-89]

Materials densified by volume or grain boundary diffusion undergo three stages of densification. Initial stage densification is indicated by a microstructure with large curvature gradients, small neck size ratios, and no apparent difference in grain size compared to particle size. Only small amounts of shrinkage occur during the initial densification stage making shrinkage a potential indicator of densification progress. In intermediate stage densification, unsmoothed pores become smooth and towards the intermediate stage's end grains begin to grow in size. Density is usually between 70% and 92% of theoretical when densification is in its intermediate stage; meaning usually appreciable shrinkage has taken place during the intermediate stage. In final stage densification, grain growth is evident, as grain sizes tend to noticeably exceed starting particle sizes. In the final stage, pores become spherical and porosity transitions from open to closed.[8, 9, 15, 80, 81, 83, 88, 90]

2.7.2 Liquid Phase Diffusion

The presence of a liquid in the microstructure at elevated temperatures provides an additional diffusion path for mass transport. Mass transport in fluids may occur by diffusion down a chemical potential gradient or by bulk fluid flow. In general, diffusion through a liquid will be faster than through a solid; making liquid phase diffusion rate controlling in most cases where a liquid is present. The microstructure for densification by liquid phase diffusion may appear amorphous or disordered. However, in some cases the liquid phase may crystallize during cooling and the microstructure may look more like a material densified by volume diffusion.[9, 75, 77, 82, 83]

Liquid phase densification may be divided into three stages based on what the rate controlling mechanism for densification is during each stage. Densification mechanisms

sequentially advance from rearrangement to solution-precipitation to final pore removal. Densification rates tend to significantly decrease as sintering progresses and may range from 10^{-3}/s to 10^{-6}/s.[9, 75, 77, 82, 83]

Many processes occur during initial liquid phase densification and may include melting, wetting, spreading, and liquid redistribution. During the rearrangement stage, both particles and liquid rearrange to achieve higher density and reduced porosity. Once a closed pack structure is achieved, particle rearrangement ends.[9, 75, 77, 82, 83]

Solution-precipitation involves dissolving of solid particles into a liquid phase providing rapid diffusion to an uncompressed surface where precipitation of particles occurs. Towards the end of solution-precipitation, interconnected pore structures begin to pinch off creating closed porosity. Solution-precipitation is complete when 90% to 95% theoretical density has been reached.[9, 75, 77, 82, 83]

During pore closure, gas from the furnace atmosphere and vaporized liquid is often trapped inside of pores. Once pores have become closed, densification becomes dependent on a driving stress (D.S.), which can be calculated using liquid-vapor interfacial energy (γ_{lv}), pore radius (r_p), and pore vapor pressure (σ_p) as shown in Equation 2.37. Densification will proceed if pore radius and vapor pressure remain small. However, pore growth will proceed if gas evolution leads to increased vapor pressure or pore radius.[9, 75, 77, 82, 83]

$$D.S. = \frac{2\gamma_{lv}}{r_p} - \sigma_p \tag{2.37}$$

2.7.3 Evaporation-Condensation

Under certain temperature conditions, one or more diffusing species may evaporate, which provides an alternative to diffusion through the species' bulk. Evaporated species travel through the furnace atmosphere or pore atmosphere and condense elsewhere on the material or surrounding furnace environment. The microstructure for evaporation-condensation may be very porous and exhibit structures of individual grains attached to each other and bridging pore spaces. There are no distinct and observable stages for evaporation-condensation mechanisms.[9, 83]

2.8 Rate Controlling Diffusion Mechanism

This section explores a method for determining RCDM for diffusion controlled densification processes. There are many methods for materials transport within a given material system but most methods may be categorized between solid and fluid state diffusion. Solid state diffusion mechanisms include volume/bulk and grain boundary diffusion, while fluid state diffusion mechanisms include liquid phase diffusion and evaporation-condensation processes. It is possible for any material system to have more than one diffusion mechanism active during densification. However, rate of transport is controlled by the most rapid diffusion mechanism active within a system.[77, 78, 80-83, 85, 90]

The RCDM model uses a volume based densification factor and various heat treatment times at a constant heat treatment temperature to produce a curve of densification factor versus heat treatment time. A diffusion mechanism may be determined based on the resultant curve's shape. The method was developed by Levin, Dirnfeld, and Shwam (LDS) and the equation for determining RCDM is shown in Equation 2.38.[84]

$$\eta = \frac{V_g - V_f}{V_f - V_{th}} = (kt)^n \tag{2.38}$$

For the LDS equation, η is a volume based densification factor, V_g is green body volume, V_f is final body volume, V_{th} is theoretical body volume, k is a reaction constant, t is heat treatment time, and n is the RCDM parameter. The LDS equation is based on an idea of vacancy migration and is similar in approach to the Larson-Miller equation. Plotting densification factor versus heat treatment time on logarithmic x and y axes allows determination of n from the plot's slope. The LDS equation has been modeled for volume/bulk diffusion, grain boundary diffusion, liquid phase diffusion, and evaporation-condensation.[5, 84]

2.9 Activation Energy

This section covers basics of activation energy, a method for calculating activation energy for densification, and difficulties in confirming activation energy. A specific energy input is required in most systems to initiate densification. The minimum energy input is generally referred to as the activation energy for densification. There are several methods for calculating activation energy for densification. However, it is difficult to confirm if calculated

activation energies are correct using conventional characterization methods because there are few methods for directly measuring activation energy.[5, 9, 84, 90]

Expansion of the LDS reveals the presence of activation energy (Q) as a variable within the reaction constant (k from Equation 2.38) as shown in Equation 2.39. Activation energy may be calculated by plotting densification factor (η) versus heat treatment temperature (T) on logarithmic axes and determining slope. Once the slope of the curve has been determined, activation energy may be calculated from Equation 2.40. Levin et al. used 48 data points over four different temperatures (12 data points per temperature) to confirm their model for sintering of an iron-copper alloy. The calculation assumes a constant n-value (diffusion mechanism) and constant heat treatment time (t) during experiments being performed. The equation also depends on the ideal gas constant (R) and pre-exponential factor (A). [5, 84]

$$\eta^{1/n} = A\exp\left(-\frac{Q}{RT}\right)t \tag{2.39}$$

$$slope = \frac{Q}{2.3R} \tag{2.40}$$

2.10 Densified Sample Characterization Techniques

This section describes methods for determining density, shrinkage, and microstructure. After compacts have been heat treated, a variety of characterization techniques exist for determining how a material may have changed during heat treatment. Use of XRD may reveal compound changes and changes in compound morphology, while density measurements and shrinkage may give indications of densification stage or active diffusion mechanisms. When SEM is used to analyze cross-section and surfaces of heat treated compacts, it is possible to gain insight into the method of densification of a compact.[9, 29, 62]

2.10.1 Density and Shrinkage Measurements

In this section, geometric density measurements, determination of density using Archimedes' method shrinkage, and shrinkage measurement are described. Density of a heat treated powder compact is important in determining degree of densification taking place during heat treatment. Several methods for determining density of a material exist including physical dimension and mass measurement, and Archimedes' methods. Neither is able to quantifiably account for closed porosity should it be present within a material. Shrinkage is a measure of

dimensional change from a compact's green state to its final state and provides indications of mass transport. In addition, determination of volume required for shrinkage calculations is also necessary for calculating densification factor (η).[9, 13, 14, 29, 62]

2.10.1.1 Geometric Density Measurements

Measurement of density (ρ) may be performed by measuring physical dimensions and object mass (m). Physical dimensions may then be used to calculate object volume (V). Object mass may then be divided by its volume to calculate object density as shown in Equation 2.41. The simple method of calculating density works well for objects with simple shapes and no distortions, but becomes increasingly complicated with increasing geometric complexities. In addition, geometric density measurement is unable to provide any quantitative information on object porosity.[9, 14, 29, 62]

$$\rho = \frac{m}{V} \tag{2.41}$$

2.10.1.2 Archimedes' Methods

Archimedes' method requires three steps to determine volume and density of an object with an irregular shape. The first step is to measure object mass completely dry (m_{dry}). Then the object is immersed in a fluid other than air, and object mass is measured while submerged in the fluid ($m_{suspended}$). Finally, the object is removed from the fluid, any remaining fluid is removed from the object's surface, and object mass is measured while filled with fluid ($m_{saturated}$). Once all three measurements have been taken, it is possible to calculate immersion bulk density ($\rho_{immersion}$), open pore volume (V_{open}), impervious volume ($V_{impervious}$), apparent porosity, and liquid absorption as shown in Equations 2.42 – 2.46. Fluid density (ρ_{fluid}) is important to each volume and density calculation. It may also be necessary to consider change in fluid density with respect to fluid temperature.[9, 62]

$$\rho_{immersion} = \frac{m_{saturated} - m_{suspended}}{\rho_{fluid}} \tag{2.42}$$

$$V_{open} = \frac{m_{saturated} - m_{dry}}{\rho_{fluid}} \tag{2.43}$$

$$V_{impervious} = \frac{m_{dry} - m_{suspended}}{\rho_{fluid}} \tag{2.44}$$

$$Apparent\ Porosity = \frac{m_{saturated} - m_{dry}}{m_{saturated} - m_{suspended}} \times 100 \tag{2.45}$$

$$Liquid\ Absorption = \frac{m_{saturated} - m_{dry}}{m_{dry}} \times 100 \tag{2.46}$$

If it is assumed there is no closed porosity within an object, then impervious volume represents the total volume of all solid matter within the object. Additionally, if it is assumed the object mass is due only to solid matter, then it is possible to approximate an object's theoretical density as shown in Equation 2.47. However, it should be understood Equation 2.47 is a rough approximation of theoretical density and better methods for calculating theoretical density do exist.[9, 62]

$$\rho_{theoretical} = \frac{m_{dry}}{V_{impervious}} \tag{2.47}$$

2.10.1.3 Shrinkage

Shrinkage of an object is the volume decrease of the object from one state to another. For densification studies, green body volume (V_g) and heat treated body volume (V_f) should be measured. Shrinkage may then be calculated using Equation 2.48. Calculated shrinkage values may vary depending on methods used for determining volumes.[9, 62]

$$Shrinkage = \frac{V_g - V_f}{V_g} \times 100 \tag{2.48}$$

2.10.2 Microstructural Examination

Heat treated compacts may be observed using SEM to determine morphological features within the microstructure. Analysis along a fracture surface provides insight into the mode of fracture and features of the bulk microstructure. Pores within the microstructure are evidenced by very dark regions within SEM images. Identification of pores within the microstructure may be important in determining the presence of closed porosity. Imaging of heat treated compact surfaces may provide additional information on processes occurring during heat treatment.[9, 62]

3. Experimental Methods

This chapter presents the powder production, preliminary experiments, predicting densification behavior, Rate Controlling Diffusion Mechanism (RCDM), activation energy, and theoretical/experimental comparison. The powder production section covers the Al_2O_3/TiB_2 SHS reaction and milling procedures. The preliminary experiments section describes methods used in powder characterization, sample formation, heat treatment of carbothermic produced TiB_2, and preliminary heat treatments of SHS produced Al_2O_3/TiB_2.

The predicting densification behavior section explains development of programs in determining Sintering Time Constants (STCs) and predicting sintering behavior of SHS produced Al_2O_3/TiB_2. The RCDM and activation energy section presents preparation for experimentation, heat treatments, characterization, calculations, and analysis. The theoretical/experimental comparison section covers comparison of predictions from preliminary experimentation and modeling with final experimental results for STCs and sintering of Ceramic Matrix Composites (CMCs).

3.1 Powder Production

This section explains procedures used in powder production by SHS reaction and ball milling of product powder. The powder production by SHS reaction section explains how the Al_2O_3/TiB_2 composite was produced by resistive heating of a reactant mixture to initiate an SHS reaction. The ball milling of product powder section discusses dry milling, wet milling, sieving, and drying of SHS produced Al_2O_3/TiB_2 reaction product to produce a powder.

3.1.1 Powder Production by SHS Reaction

Approximately 500 g of Al_2O_3/TiB_2 composite material was produced by initiating an SHS reaction from a mixture of 187.84 g of Al (Alcoa Specialty Metals Grade: 123/17), 145.40 g of B_2O_3 (Fisher Scientific Laboratory Grade: A76-500), and 166.80 g of TiO_2 (Fisher Scientific: T315-500) in a fused silica crucible. The powder mixture was resistively heated using Nichrome wire driven by a 120 Volt/22 Amp manually operated variable transformer connected to the wire as shown in Figure 3.1. A simple electrical schematic of the SHS reaction setup may be found in Appendix C. Heating rate was controlled manually and voltage was increased by 2% every five seconds until reaction initiation was observed. The reaction product was cooled to room

temperature before any further processing was performed. After the reaction product was cooled, areas of the product that had reacted with the NiCr (indicated by a severe color difference in the reaction product) were removed before any subsequent processing was performed.

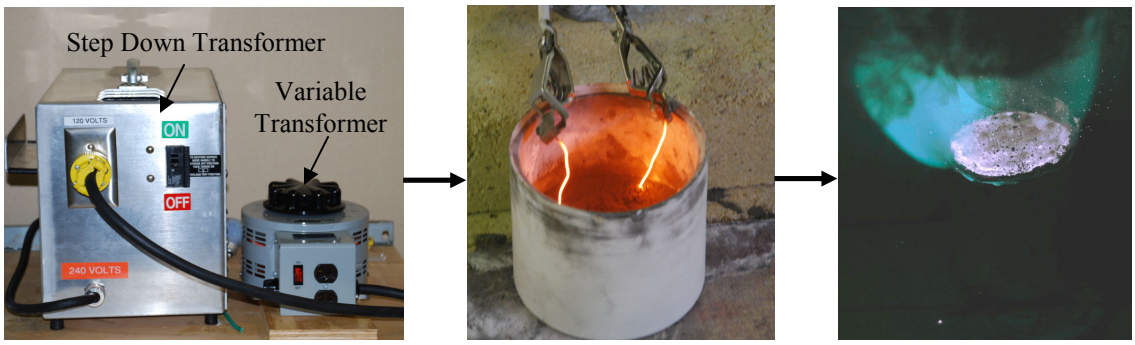

Figure 3.1 – The variable transformer (left) used to resistively heat a Nichrome wire (middle) and initiate an SHS reaction (right).

3.1.2 Ball Milling of Product Powder

The reacted mass was removed from the crucible and broken into smaller pieces. Pieces were placed inside an Al_2O_3 lined ball milling jar with Al_2O_3 milling media. The reaction product was then dry ball milled for 30 hours as shown in Figure 3.2. After 30 hours, the powder was inspected and sieved using a series of screens from 20 mesh (850 μm) to 325 mesh (45 μm).

Figure 3.2 – Reacted product that was broken into smaller pieces (left) was placed into a milling jar (middle) with milling media (not shown) and then placed on a rolling mill (right).

Any powder larger than 45 μm in size was returned to the milling jar and wet milled in polished deionized water for 70 hours. After milling, the powder was wet sieved through a series of screens from 20 mesh (850 μm) to 325 mesh (45 μm). The slurry that passed into the collection pan was then dried overnight at 110°C in a convective drying oven. The dried powder mass was reduced to powder using a mortar and pestle. The powder was then stored in a glass jar

labeled with powder sample number, chemical makeup, and total milling time. Powder samples were taken for characterization and analysis of compounds, particle size, structure, surface area, and pore volume.

3.2 Preliminary Experiments

This section covers methods used in powder characterization, sample formation, heat treatment of carbothermic produced TiB_2, and preliminary heat treatments of SHS produced Al_2O_3/TiB_2. Under powder characterization, procedures used for determining compounds, powder particle size, structure, morphology, particle surface area, and pore volume are explained. Sample formation discusses pressing experimentation including a designed pressing experiment and confirmation experiment. Heat treatment of carbothermic produced TiB_2 covers sample preparation, heat treatment conditions, and sample characterization used in experiments involving carbothermic TiB_2. Finally, preliminary heat treatments of SHS produced Al_2O_3/TiB_2 contains information on sample preparation, heat treatment conditions, and sample characterization used in preliminary experiments involving SHS produced Al_2O_3/TiB_2.

3.2.1 Powder Characterization

This section describes characterization techniques used for compound identification by X-Ray Diffraction (XRD), Particle Size Analysis (PSA), determination of structure and morphology by Scanning Electron Microscopy (SEM), and particle surface area/pore volume by gas adsorption. The compound identification section describes sample preparation and machine configuration for characterization. The PSA section explains processes used in determination of particle size by multi-laser PSA. The structure and morphology section covers use of SEM for determining particle surface structure and features. The particle surface area and pore volume section explains the procedures used for gas adsorption measurements and analysis.

3.2.1.1 Compound Identification

XRD was used to determine chemical compounds and approximate composition of powder samples. Samples were run in a Philips X'pert Pro as shown in Figure 3.3. The powder sample was poured into a sample holder on a specially designed sample preparation mount and flattened with a metal base plate. The sample holder was then sealed and placed into the XRD measurement chamber.

Figure 3.3 – Philips X'pert Pro diffractometer used for XRD analysis.[91]

The sample was X-rayed using a Cu filament run at 45 kV and 40 mA with both the source and the detector in motion during the scan. Diffraction was performed over a range of 2θ values from 10° to 110° with a step size of 0.01° and step changed every 0.54 seconds. Also, the sample stage was rotated at 15 rpm. The resulting diffraction patterns were analyzed using the X'Pert High Score software to index peaks and identify compounds.

3.2.1.2 Powder Particle Size

A Horiba Partica LA-950 Laser Diffraction Particle Size Analyzer, as shown in Figure 3.4, was used to determine particle size distribution of the processed powders. The unit was operated in wet mode using the index of refraction for Al_2O_3 (1.660), TiB_2 (2.500), and a rule of mixtures calculated value for Al_2O_3/TiB_2 composite (1.882). Water with 1 g per liter of sodium hexametaphosphate (NaHMP) was used as a dispersant and the machine reported distributions based on volume.

A configuration file was created and included information on sample name, index of refraction to be used, and distribution basis. Once the configuration file was set, dispersant was automatically fed into the sample chamber and dispersant in the sample chamber was circulated at a speed of "seven." The dispersant was then debubbled using the systems debubble function; and agitation of the dispersant was begun at an agitation level of "four." After waiting approximately one minute, an alignment of the two lasers (for determining particle size) was performed using the internal alignment function within the system.

Figure 3.4 – Horiba Partica LA-950 Laser Diffraction Particle Size Analyzer used for determining the particle size distributions of SHS-produced Al_2O_3/TiB_2 powder.[92]

After the alignment was completed, the background was blanked, effectively setting any noise to a zero level. Next a powder sample was added slowly until both red and blue lasers indicated transmittance was between 80-90% and 70-90% respectively. Then sample agglomerates were broken up using ultrasonic vibrations for 20 seconds at a system preset level of "two." Finally, at least three sample measurements were taken of each sample for statistical comparison. Once measurements were complete, distributions were electronically saved individually and overlaid with other distributions for comparison.

3.2.1.3 Structure and Morphology

SEM was used to analyze powder surface structure and morphological features. Powder sample imaging was performed with a Hitachi S-3700 Ultra Large Variable Pressure SEM (VP-SEM) as shown in Figure 3.5. A small amount of powder was placed into a glass test tube (15 x 85 mm) and diluted with a liquid solution of water and Trisodium Pyrophosphate (TSPP – Pfaltz & Bauer: S06993) to facilitate dispersion of particles. Double sided carbon tape was placed onto an SEM stub and a small pipette was used to deposit seven drops of the powder suspension onto the SEM stub. The SEM sample was then allowed to dry overnight.

Figure 3.5 – Hitachi S-3700 Ultra Large Variable Pressure SEM used for imaging powder samples.[93]

Once dry, the samples were placed into the VP-SEM chamber and pumped down to ~60 Pa. The VP-SEM was operated in backscattering mode with accelerating voltage set at 20.0 kV. Where appropriate, Electron Dispersive Spectroscopy (EDS) was performed on the samples to determine elemental make up of viewed regions. Also, measurements of individual particles were taken using VP-SEM systems software.

3.2.1.4 Particle Surface Area and Pore Volume

A 3 g sample of powder was prepared in a glass bulb sample holder and left to outgas in a Quantachrome Instruments Autosorb-1 Surface Area and Pore Size Analyzer, as shown in Figure 3.6, for several hours at 300°C. Once the sample had thoroughly outgassed, it was weighed. Sample weight was input into the Quantachrome computer software. Run parameters were then set and the machine's Dewars were filled with liquid nitrogen. The sample was secured into position and the run cycle was initiated. Once the run cycle was completed, Quantachrome software was used to calculate surface area of the particles measured and pore volume of the particles.

Figure 3.6 – Quantachrome Instruments Autosorb-1 Surface Area and Pore Size Analyzer used for determining surface area and pore volume.[94]

3.2.3 Sample Formation

This section describes information on a designed pressing experiment and confirmation experiment. The designed pressing experiment section details use of a designed experiment to determine significance of selected factors on powder compact green density. It also discusses

use of analytical tools such as Analysis Of Variance (ANOVA) calculations, error pooling, and main effect plots. The confirmation experiment section explains procedures and calculations used in confirming individual factor and system significance as determined by ANOVA.

3.2.3.1 Designed Pressing Experiment

It was determined that maximizing green density was an appropriate problem to solve with experimentation. Therefore, green density was chosen as a variable Quality Characteristic (QC) for the experiments. During planning for the experiment, several parameters were considered for testing including: hold time, powder drying (whether powder was dried or pressed straight from its container), maintaining peak pressure, pressing pressure, composition, and action type.

Pressing pressure, action type, and powder drying were considered factors of primary importance for testing. Pressing pressure was chosen to be varied between 10,000 and 20,000 psi; single action pressing was to be compared with dual action pressing as shown in Figure 3.7; and powder would be pressed after drying or straight from its container. All other factors that had been considered were held constant and no interactions were to be studied during experimentation.

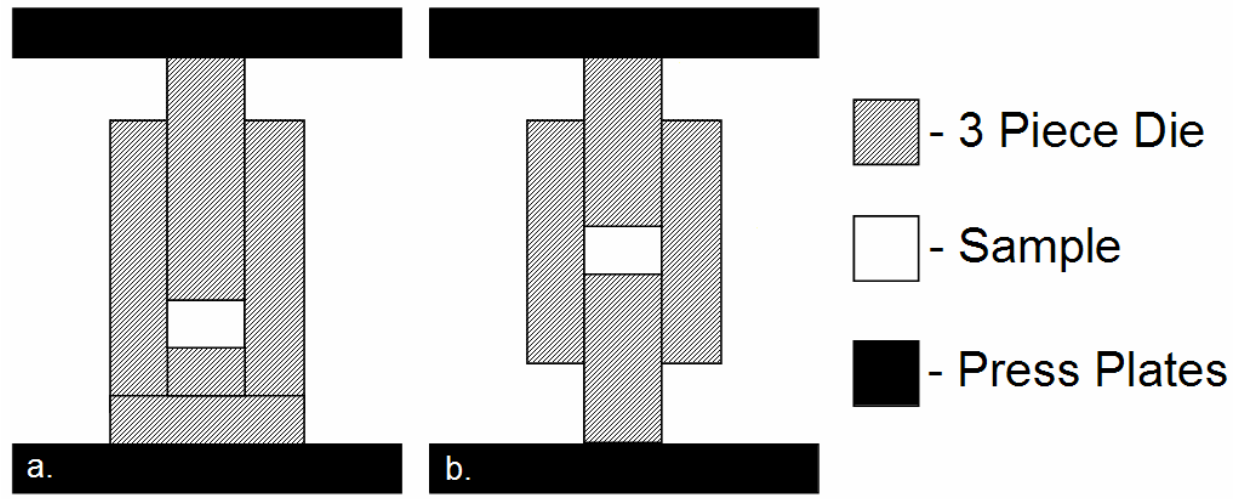

Figure 3.7 – Schematic comparison of a. single action and b. dual action pressing setups for Al_2O_3/TiB_2 powder compaction

Based on time and resources available, a fractional factorial design was chosen for implementation of experiments. An L4 orthogonal array was established for experimentation as shown in Table 3.1. Since there were three factors to be tested at two levels, it was determined

that the array had a resolution of III. Each experimental trial was performed five times in non-blocks using randomization to ensure a minimum impact of process noise on QC response.

Table 3.1 – Pressing Designed Experiment L4 Orthogonal Array

Trial	Pressing Pressure (psi)	Action Type	Powder Dried
1	10,000	Single	Yes
2	10,000	Double	No
3	20,000	Single	No
4	20,000	Double	Yes

After each sample was pressed, its physical dimensions and mass were measured and recorded into a lab notebook with a prepared data sheet. Green density of each sample was calculated from its mass and volume according to Equation 3.1. Sample data was then sorted by trial number in preparation for data analysis.

$$\rho = \frac{m}{V} \tag{3.1}$$

An Excel spreadsheet was created to perform most calculations required for ANOVA of designed experiment results, prediction of response at given factor/level combinations, and calculations associated with a confirmation experiment. Data from each individual trial was input into an experimental grid according to trial and repetition number. A sum of observations for each factor and level (A_i) and a total sum (T) of all observations (y_i) were calculated in the spreadsheet.

The spreadsheet used the calculated values, along with the total number of observations (N), to calculate a total sum of squares (SS_T) according to Equation 3.2. Additionally, Sum of Squares (SS) for individual factors were calculated using A_i, total number of observations for each factor and level (n_{ai}), T, and N according to Equation 3.3. From there, the spreadsheet calculated a SS due to error (SS_e) according to Equation 3.4.

$$SS_T = \sum_{i=1}^{N} y_i^2 - \frac{T^2}{N} \tag{3.2}$$

$$SS_A = \frac{A_1^2}{n_{a1}} + \frac{A_2^2}{n_{a2}} - \frac{T^2}{N} \tag{3.3}$$

$$SS_e = SS_T - SS_A - SS_B - SS_C \tag{3.4}$$

The spreadsheet also calculated Degrees Of Freedom (DOF). It calculated total DOF (ν_T) according to Equation 3.5. To calculate DOF of each factor (ν_A), the spreadsheet required a number of levels for each factor (K_A) and then calculated ν_A for each factor according to Equation 3.6. DOF due to error (ν_e) was calculated last according to Equation 3.7.

$$\nu_T = N - 1 \tag{3.5}$$

$$\nu_A = K_A - 1 \tag{3.6}$$

$$\nu_e = \nu_T - \nu_A - \nu_B - \nu_C \tag{3.7}$$

After DOF's were calculated, the spreadsheet was used to calculate variance due to individual factors (V_A) and error (V_e) according to Equations 3.8 and 3.9. From there it calculated F-values (F_A) for each factor according to Equation 3.10. The calculated F-values were compared with F-tables of 90%, 95%, and 99% significance to determine confidence in significance of each factor tested. The spreadsheet was used to calculate pure SS (SS') and SS' was used to calculate percent contribution (P) according to Equations 3.11 and 3.12. After all the calculations were performed, a table summarizing results was created.

$$V_A = \frac{SS_A}{\nu_A} \tag{3.8}$$

$$V_e = \frac{SS_e}{\nu_e} \tag{3.9}$$

$$F_A = \frac{V_A}{V_e} \tag{3.10}$$

$$SS'_A = SS_A - V_e \cdot \nu_A \tag{3.11}$$

$$P = \frac{SS'_A}{SS_T} \times 100 \tag{3.12}$$

Based on results of percent contribution of significant factors, error pooling was employed to ANOVA results. Error was pooled up to ensure no significant factors where pooled into error terms. Based on error pooling, a new ANOVA table was generated including new ν_e,

V_e, calculated F, SS' and P values reflecting results of error pooling. New calculated F-values were compared with F-tables of 90%, 95%, and 99% significance to determine confidence in significance of each factor tested. Main effect plots were constructed for each factor and compared with ANOVA results.

3.2.3.2 Confirmation Experiment

After ANOVA calculations were completed, the spreadsheet was used to calculate Predicted Response (PR) for various factor/level combinations and was based on average QC response for each factor ($\overline{A}_i$) and average QC response for all factors and levels ($\overline{T}$) as shown in Equation 3.13. The factor/level combination with highest PR value was chosen as the ideal configuration for a confirmation experiment. The chosen experimental configuration was used to press three powder compacts and each compact's physical dimensions and mass were measured directly after pressing. An average green density ($\overline{y}$) and standard deviation (SD) were calculated. The $\overline{y}$ and SD values were used in conjunction with the number of samples used in the confirmation experiment (n) to calculate confidence interval according to Equation 3.14.

$$PR = \overline{A}_i + \overline{B}_i + \overline{C}_i - 2\overline{T} \tag{3.13}$$

$$CI = \overline{y} \pm 3\left(\frac{SD}{\sqrt{n}}\right) \tag{3.14}$$

3.2.4 Heat Treatment of Carbothermic TiB_2

This section explains processes of sample preparation, heat treatment conditions, and characterization for heat treatment of carbothermic TiB_2. Sample preparation and heat treatment conditions covers pressing equipment, pressing conditions for formation of powder compacts, experimental sample configuration, equipment used for heat treatments, and individual sample heat treatment conditions. Characterization describes equipment and procedures used in determining density, shrinkage, and microstructural features.

3.2.4.1 Sample Preparation and Heat Treatment Conditions

Un-dried carbothermic produced TiB_2 (H.C. Starck Grade F: 12045-63-5) powders were uniaxially compacted in Model C Carver manual hydraulic press using 20,000 psi of pressure and a dual action pressing mode. Once samples were pressed, sample diameter and thickness

were measured using digital calipers; and mass was determined using a scale. From the physical measurements, each sample's geometric green density was calculated as shown in Equation 3.1.

Pressed compacts were placed onto a cylindrical graphite setter covered in loose carbothermic TiB_2 powder as shown in Figure 3.8. A reference mark was placed in the setter for identification of individual compacts after heat treatment. A custom ultra high temperature vacuum/inert atmosphere furnace was used for heat treatment of powder compacts and is shown in Figure 3.9. The furnace was capable of heat treatment temperatures up to 3000°C and was capable of being controlled by thermocouple at temperatures below 1100°C. For temperatures above 1100°C, the furnace was controlled by optical pyrometer. Compacts were heat treated at either 1800°C or 2100°C and held at temperature for 30 minutes and 60 minutes respectively. Helium line pressure was controlled at approximately 5 psig.

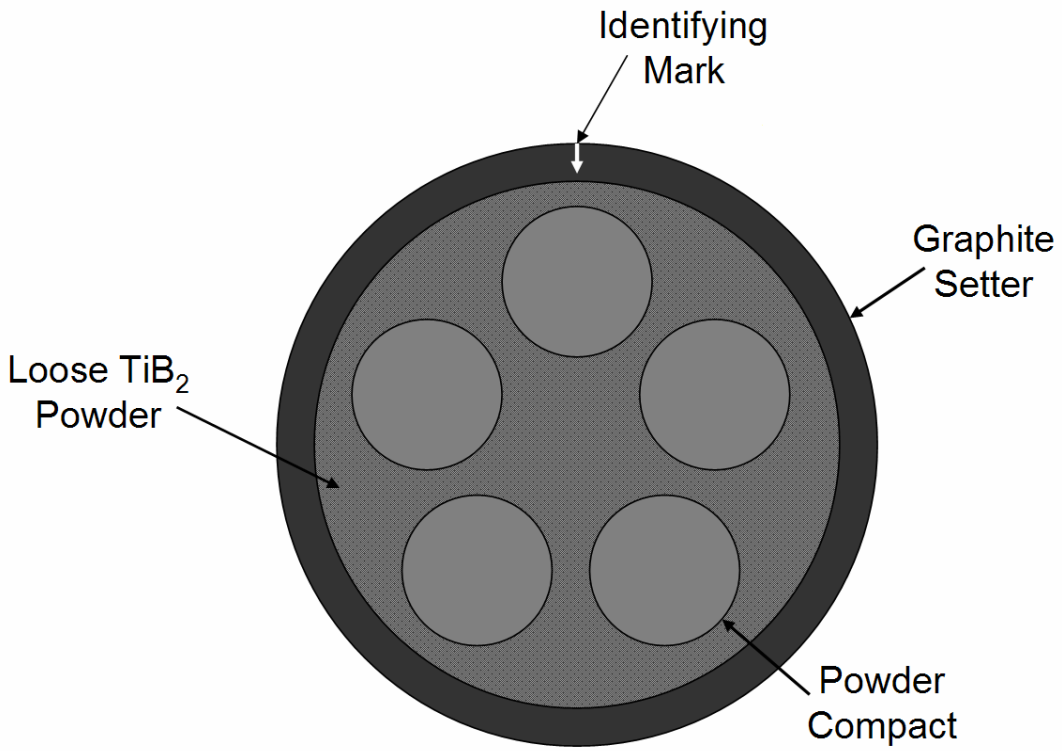

Figure 3.8 – Schematic representation of sample configuration used for heat treatment of TiB_2 powder compacts.

Figure 3.9 – Custom ultra high temperature vacuum/inert atmosphere furnace used for experimentation.

3.2.4.2 Characterization

Each heat treated sample was placed in a vacuum drying oven for 12 hours at 100°C to remove excess moisture. Dried samples were then weighed using a Sartorius LA120S balance (accurate to three decimal places) and the values for dry mass (m_{dry}) were recorded electronically. Once dry mass was obtained, the samples were placed into an aluminum sample holder the sample holder was placed inside a vacuum chamber. The chamber was pumped down to a vacuum of -15 psi and a water supply valve was opened allowing water to flow into the aluminum sample holder until samples were completely submerged. Equipment used for drying, weighing, and infiltrating of samples are shown in Figure 3.10.

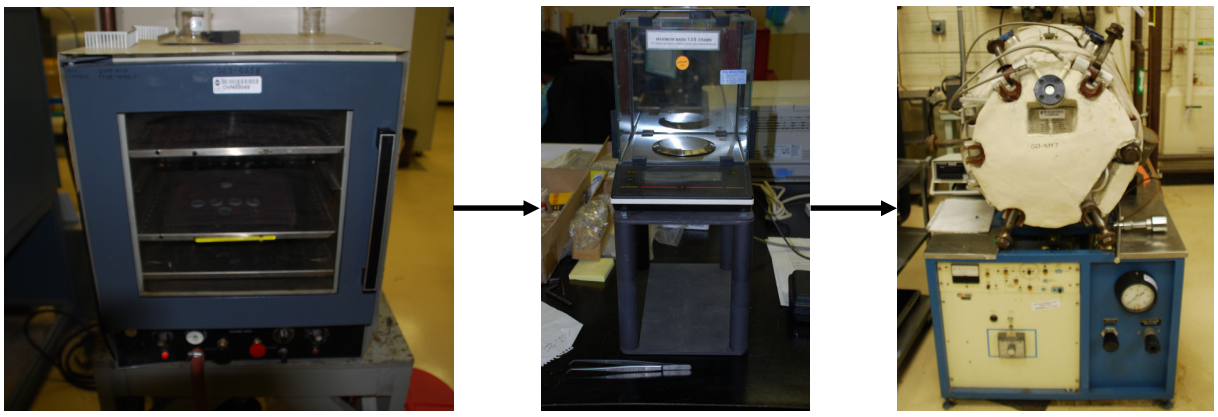

Figure 3.10 – Each sample was placed into the vacuum drying oven (left); once dried it was placed onto the balance and massed (middle); then placed into a vacuum chamber (right) and submerged in water.

After samples were submerged, the chamber was vented and samples were removed from the chamber. Suspended weights ($m_{suspended}$) of submerged samples were obtained using a hanging balance setup. Excess surface moisture was removed from each sample using a damp paper towel; then each sample was weighed with saturated weight ($m_{saturated}$) values being recorded electronically. From the mass measurements, immersion bulk density, pore volume, impervious volume, apparent porosity, liquid absorption, and shrinkage were calculated in an Excel spreadsheet using Equations 3.15 – 3.20.

$$\rho_{immersion} = \frac{m_{saturated} - m_{suspended}}{\rho_{fluid}} \tag{3.15}$$

$$V_{open} = \frac{m_{saturated} - m_{dry}}{\rho_{fluid}} \tag{3.16}$$

$$V_{impervious} = \frac{m_{dry} - m_{suspended}}{\rho_{fluid}} \tag{3.17}$$

$$\begin{matrix} Apparent \\ Porosity \end{matrix} = \frac{m_{saturated} - m_{dry}}{m_{saturated} - m_{suspended}} \times 100 \tag{3.18}$$

$$\begin{matrix} Liquid \\ Absorption \end{matrix} = \frac{m_{saturated} - m_{dry}}{m_{dry}} \times 100 \tag{3.19}$$

$$Shrinkage = \frac{V_g - V_f}{V_g} \times 100 \tag{3.20}$$

Heat treated samples were then imaged with a Hitachi S-3700 Ultra Large VP-SEM. Double sided carbon tape was placed onto an SEM stub and a sample was mounted onto the SEM stub. The uncoated SEM samples were then placed into the SEM chamber and the chamber was pumped down to operating vacuum. Imagining was performed at accelerating voltages of 10kV and 20kV. EDS was used to identify chemical compositions within phases of interest.

3.2.5 Preliminary Heat Treatment of SHS Produced Al_2O_3/TiB_2

This section describes processes of sample preparation, heat treatment conditions, and characterization for preliminary heat treatment of SHS produced Al_2O_3/TiB_2. Sample

preparation and heat treatment conditions covers pressing equipment, pressing conditions for formation of powder compacts, experimental sample configuration, equipment used for heat treatments, and individual sample heat treatment conditions. Characterization describes equipment and procedures used in determining density, shrinkage, and microstructural features.

3.2.5.1 Sample Preparation and Heat Treatment Conditions

Un-dried SHS produced Al_2O_3/TiB_2 powders were uniaxially compacted in a Model C Carver manual hydraulic press using 20,000 psi of pressure and a single action pressing mode. Once samples were pressed, sample diameter and thickness were measured using digital calipers; and mass was determined using a scale. From the physical measurements, each sample's volume and geometric green density were calculated.

Pressed SHS produced Al_2O_3/TiB_2 compacts were placed into a rectangular Al_2O_3 tray with its bottom covered in loose carbothermic TiB_2 powder as shown in Figure 3.11. A defect in one of the tray's side walls was used as a reference mark for identification of individual compacts after heat treatment. A Lindberg model 54434 1700°C tube furnace with an alumina tube was used for heat treatment of powder compacts and is shown in Figure 3.12.

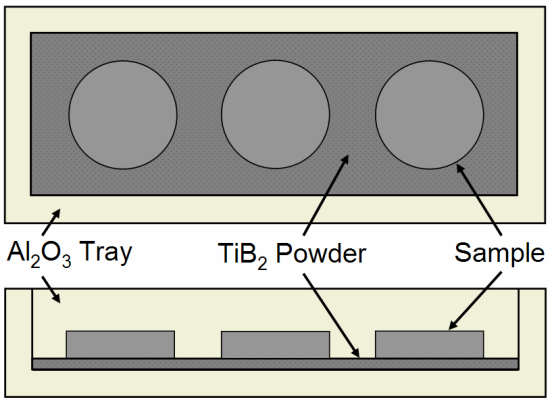

Figure 3.11 – Schematic representation of sample configuration used for heat treatment of SHS produced Al_2O_3/TiB_2 compacts.

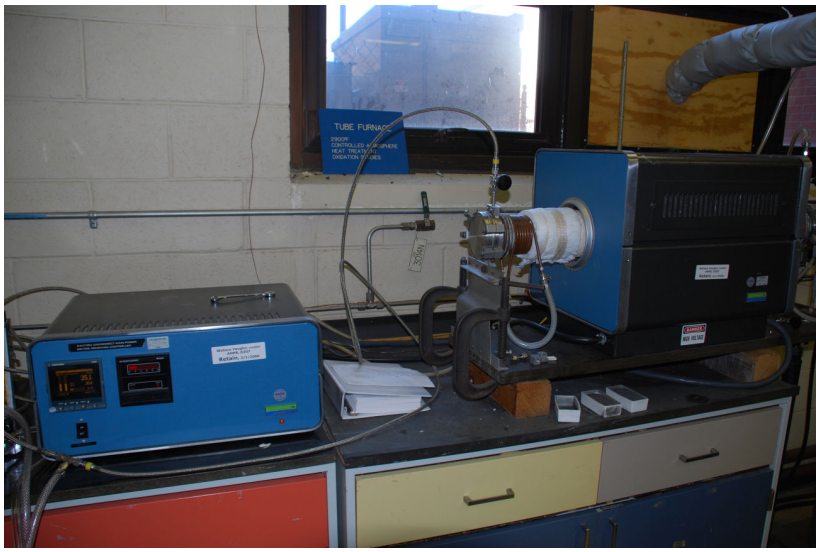

Figure 3.12 – Lindberg model 54434 1700°C tube furnace used for experimentation.

The furnace was capable of heat treatment temperatures up to 1700°C and was controlled by a thermocouple near the heating elements as shown in Figure 3.13. The setup also included a thermocouple positioned inside the tube with temperature values recorded using a chart recorder. Preliminary experiments used the two thermocouples to determine temperature correction required for accurate programming of the furnace.

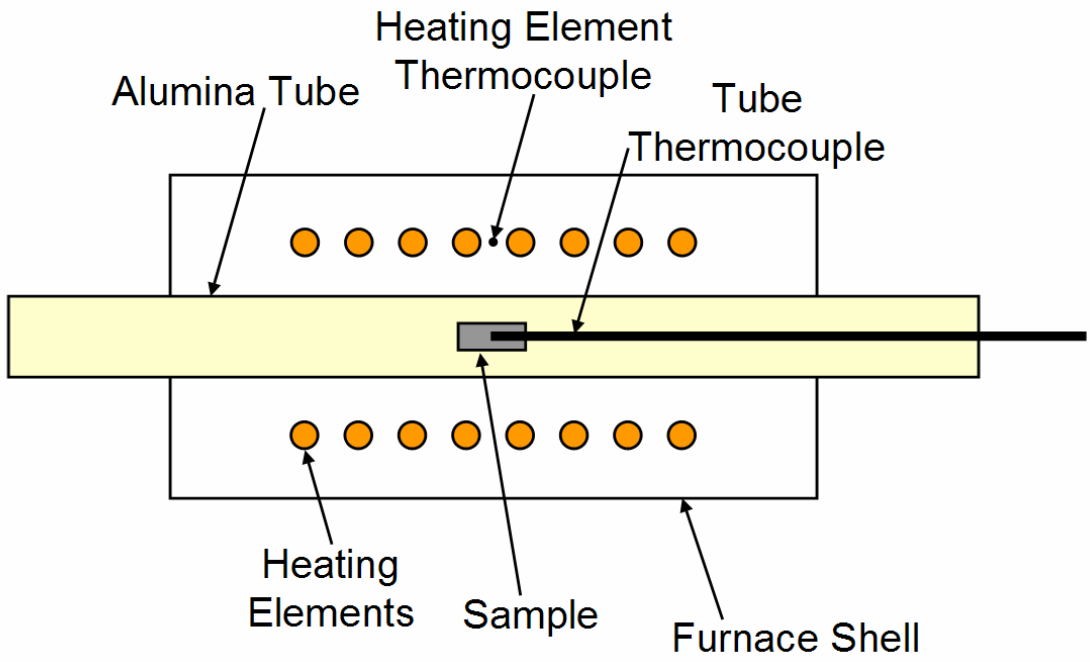

Figure 3.13 – Schematic representation of the furnace setup used for heat treatments of SHS produced Al_2O_3/TiB_2.

The furnace was programmed to reach a temperature of 1500°C (heating element thermocouple) with a helium line pressure of approximately 15 psig. Compacts were also heat treated at 1490°C (inside tube thermocouple) and held at temperature for 60 minutes. Helium line pressure was controlled at approximately 5 psig until approximately 1100°C during cooling, at which point, helium line pressure was essentially 0 psig.

3.2.5.2 Characterization

Each heat treated sample was placed in a vacuum drying oven for 12 hours at 100°C to remove excess moisture. Dried samples were then weighed using a Sartorius LA120S balance (accurate to three decimal places) and the values for dry mass were recorded electronically. Once dry mass was obtained, the samples were placed into an aluminum sample holder and the sample holder was placed inside a vacuum chamber. The chamber was pumped down to a vacuum of -15 psi and a water supply valve was opened allowing water to flow into the aluminum sample holder until samples were completely submerged.

After samples were submerged, the chamber was vented and samples were removed from the chamber. Suspended weights of submerged samples were obtained using a hanging balance setup. Excess surface moisture was removed from each sample using a damp paper towel; then each sample was weighed with saturated weight values being recorded electronically. From the mass measurements, immersion bulk density, pore volume, impervious volume, apparent porosity, liquid absorption, and shrinkage were calculated in an Excel spreadsheet using Equations 3.15 – 3.20.

Heat treated samples were then imaged with a Hitachi S-3700 Ultra Large VP-SEM. Double sided carbon tape was placed onto an SEM stub and a sample was mounted onto the SEM stub. Samples were sputter coated with a 4 nm layer of gold (Au) – palladium (Pd) using an Anatech LTD Hummer X. SEM samples were then placed into the SEM chamber and the chamber was pumped down to operating vacuum. Imagining was performed at accelerating voltages of 10kV and 20kV. EDS was used to identify chemical compositions within phases of interest.

3.3 Predicting the Densification Behavior of SHS Produced Al_2O_3/TiB_2

This section covers development of programs in determining STCs and predicting sintering behavior of SHS produced Al_2O_3/TiB_2. The STCs section describes how STCs were calculated and plotted using Excel and Mathematica (Ver. 6) for Students. The section sintering

of CMCs explains how Mathematica was used to plot curves of densification factor ($\Delta\rho_f/\Delta\rho_{max}$) versus heat treatment time at given heat treatment temperature for various volume fractions of TiB_2 in manually mixed Al_2O_3/TiB_2 composites. The models were used in predicting system response to heat treatment temperature, heat treatment time, and composition.

3.3.1 Sintering Time Constants

The model used for analyzing STCs was based on sintering of the matrix only. Data for sintering of submicron Al_2O_3 powders from the ASM Handbook of Materials Volume 4 was used to plot natural logarithm of one minus $\Delta\rho_f/\Delta\rho_{max}$ versus heat treatment time (t) for different time regimes and fixed heat treatment temperatures (1200°C, 1300°C, and 1350°C). An Excel built in fit function was used to determine slopes for each time regime and STCs were calculated from the slopes according to Equation 3.21.

$$1 - \frac{\Delta\rho_f}{\Delta\rho_{\max}} = e^{-t/\tau} \tag{3.21}$$

Due to difficulties in producing appropriate plots with compounded slopes in Excel, Mathematica was used to produce plots. From the plots, it was possible to determine if the matrix had a single STC or multiple STCs. The model was used to determine appropriate heat treatment times for determination of RCDM experiments. Preliminary STC values were later compared with STCs calculated from experimental results.

3.3.2 Sintering of Ceramic Matrix Composites

A Mathematica script for producing plots of $\Delta\rho_f/\Delta\rho_{max}$ versus heat treatment time (t) was developed. The script was used to plot data from Matsushita et al. based on Equation 3.22. The script first calculates $\Delta\rho_f/\Delta\rho_{max}$ from a single point or multiple points for change in density from green state to heat treated state ($\Delta\rho_f$) and change in density from green state to full theoretically dense state ($\Delta\rho_{max}$). From there it used calculated STCs (τ) to calculate β-factor with volume fraction of reinforcement (f).

The function was used to create several plots of densification versus time for different volume fraction Al_2O_3/TiB_2 composites. Finally, the script plots $\Delta\rho_f/\Delta\rho_{max}$ versus t for each volume fraction for which data has been input. The plots were used to predict amount of densification expected at different heat treatment times and volume fractions for a given heat

treatment temperature. Additionally, the plots were used to determine heat treatment temperatures for calculation of activation energy.

$$\frac{\Delta\rho_f}{\Delta\rho_{\max}} = 1 - \exp\left(-\frac{9\beta}{4f + 9\beta}\frac{t}{\tau}\right) \tag{3.22}$$

3.4 Rate Controlling Diffusion Mechanism and Activation Energy

This section covers preparation for experimentation, heat treatments, characterization, calculations, and analysis. The preparation and heat treatment section discusses the test matrix used, sample preparation, and heat treatment procedures. Characterization explains determination of density, shrinkage, microstructure, and phase. The calculations and analysis section describes the creation of a Mathematica script used for calculation of RCDM and activation energy. Experiments performed were focused on determination of activation energy and RCDM active within Al_2O_3/TiB_2 during heat treatment. The activation energy for densification and RCDM were determined using the Levin-Dirfield-Shwam LDS equation because the LDS method allowed both factors to be calculated using the same equation.

3.4.1 Preparation and Heat Treatment

To determine the RCDM using the LDS equation, three samples were heated at 2°C/min to 1500°C and held for 30 minutes, 60 minutes, and 90 minutes in a Lindberg model 54434 1700°C tube furnace with an alumina tube then furnace cooled as summarized in Table 3.2. Samples were heat treated on a bed of TiB_2 powder inside an Al_2O_3 tray as shown in Figure 3.11. After heat treatment, sample densities were measured using Archimedes' principle and the physical dimensions were measured to determine shrinkage.

Table 3.2 – Summary of Experiments for Calculating RCDM and Activation Energy

RCDM		Activation Energy	
Temperature	Time	Temperature	Time
1500°C	30 min	1370°C	30 min
1500°C	60 min	1435°C	30 min
1500°C	90 min	1500°C	30 min

To determine activation energy by the LDS equation, three samples were heated at 2°C/min to 1370°C, 1435°C, and 1500°C and held for 30 minutes in a Lindberg model 54434 1700°C tube furnace with an alumina tube then furnace cooled. A sample heat treatment profile for the samples heat treated at 1500°C for 30 minutes is shown in Figure 3.14. Samples were

heat treated on a bed of carbothermic TiB_2 powder inside an Al_2O_3 tray as shown in Figure 3.11. After heat treating, the sample densities were measured using Archimedes' principle and physical dimensions were measured to determine shrinkage.

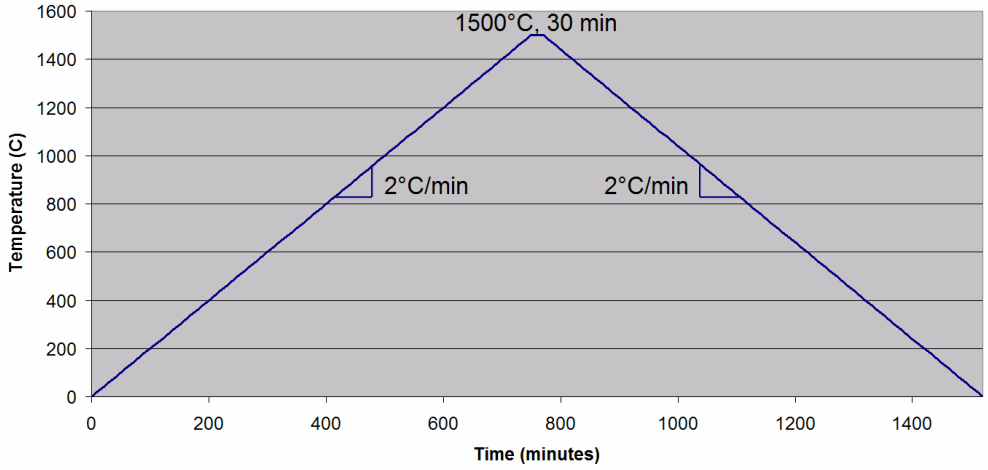

Figure 3.14 – Heat treatment profile for an Al_2O_3/TiB_2 composite heat treated at 1500°C for 30 minutes

3.4.2 Characterization

This section explains determination of density, shrinkage, microstructure, and phase. The density and shrinkage section describes use of Archimedes' method and physical dimensions to determine density and shrinkage. The microstructure section discusses use of SEM/EDS to determine features of top, bottom, and fracture surfaces for various samples. Compound identification covers use of XRD for determining chemical makeup of heat treated samples.

3.4.2.1 Density and Shrinkage

Each heat treated sample was placed in a vacuum drying oven for 12 hours at 100°C to remove excess moisture. Dried samples were then weighed using a Sartorius LA120S balance (accurate to three decimal places) and the values for dry mass were recorded electronically. Once dry mass was obtained, the samples were placed into an aluminum sample holder and then placed inside a vacuum chamber. The chamber was pumped down to a vacuum of -15 psi and a water supply valve was opened allowing water to flow into the aluminum sample holder until samples were completely submerged.

After samples were submerged, the chamber was vented and samples were removed from the chamber. Suspended weights of submerged samples were obtained using a hanging balance setup. Excess surface moisture was removed from each sample using a damp paper towel; then each sample was weighed with saturated weight values being recorded electronically. From the

mass measurements, immersion bulk density, pore volume, impervious volume, apparent porosity, liquid absorption, and shrinkage were calculated in an Excel spreadsheet using Equations 3.15 – 3.20. In addition, theoretical density ($\rho_{theoretical}$) was approximated according to Equation 3.23.

$$\rho_{theoretical} = \frac{m_{dry}}{V_{impervious}} \tag{3.23}$$

3.4.2.2 Microstructure

SEM was used to analyze heat treated samples. The heat treated sample imaging was performed with a FEI Quanta 600 FEG Environmental SEM (ESEM) as shown in Figure 3.15. Samples were fractured and mounted on SEM stubs for cross section and surface observations. Samples were sputter coated with a 4 nm layer of Au – Pd using an Anatech LTD Hummer X. The stubs were then placed into the SEM chamber and observed under high vacuum at an accelerating voltage of 20.0 kV. The chemical compositions of different phases within the microstructure were determined using EDS.

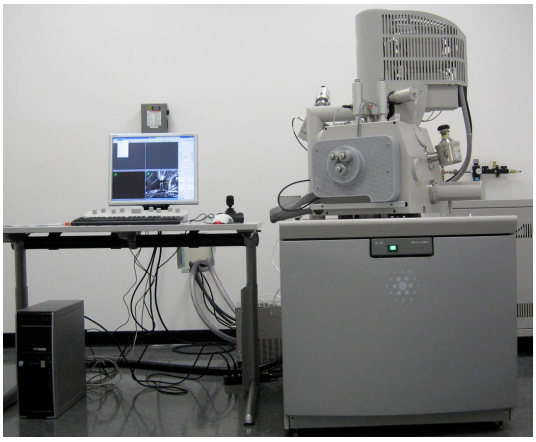

Figure 3.15 – FEI Quanta 600 FEG ESEM used to observe heat treated samples.[95]

3.4.2.3 Compound Identification

XRD was used to determine chemical compounds and approximate composition of powder samples. Samples were run in a Philips X'pert Pro as shown in Figure 3.3. The powder sample was poured into a sample holder on a specially designed sample preparation mount and flattened with a metal base plate. The sample holder was then sealed and placed into the XRD measurement chamber.

The sample was X-rayed using a Cu filament run at 45 kV and 40 mA with both the source and the detector in motion during the scan. Diffraction was performed over a range of 2θ values from 10° to 110° with a step size of 0.01° and step changed every 0.54 seconds. Also, the sample stage was rotated at 15 rpm. The resulting diffraction patterns were analyzed using the X'Pert High Score software to index peaks and identify compounds.

3.4.3 Rate Controlling Diffusion Mechanism and Activation Energy Calculations

A script was designed to determine RCDM parameter (n) and activation energy for densification from green body volume (V_g), heat treated volume (V_f), theoretical volume (V_{th}), heat treatment time (t), and heat treatment temperature (T) according to Equations 3.24 and 3.25. The first half of the script received inputs for V_g, V_f, V_{th}, and t for samples heat treated at a constant temperature. Next densification factor (η) for each heat treatment time was calculated by volume changes as shown in Equation 3.24. A solver function built into Mathematica was used to solve Equation 3.24 for k and n.

$$\eta = \frac{V_g - V_f}{V_f - V_{th}} = (kt)^n \tag{3.24}$$

$$\eta^{1/n} = A\exp\left(-\frac{Q}{RT}\right)t \tag{3.25}$$

Next, the script plotted its calculated fit function against entered experimental data to provide a visual check of fit reliability. An average n-value, standard deviation, maximum n-value, and minimum n-value were determined. The average n-value was used in a decision statement based on values for different diffusion mechanisms from literature. Finally, the RCDM is output in large bold text and the first half of the script is complete.

The second half of the script received inputs for V_g, V_f, V_{th}, and T for samples heat treated at a constant time. Next densification factor (η) for each heat treatment temperature was calculated by volume changes as shown in Equation 3.24. A solver function built into Mathematica was used to solve Equation 3.25 for A and slope (as defined in Equation 3.26).

$$slope = \frac{Qn}{R} \tag{3.26}$$

Next, the script plotted its calculated fit function against entered experimental data to provide a visual check of fit reliability. Finally, an average activation energy and standard deviation were calculated and output. The solver was used to determine RCDM and activation energy from results of experiments summarized in Table 3.2. The solver was run using two different values of V_{th}. The first value was based on a theoretical density of 4.12 g/cm^3 and the second was based on theoretical density as calculated in Equation 3.23.

3.5 Theoretical and Experimental Comparison

This section covers comparison of predictions from preliminary experimentation and modeling with final experimental results for STCs and sintering of CMCs. The STCs section explains how STCs were calculated from experimental results and what comparisons were made between modeling and final experimental results. The sintering of CMCs section discusses production of a prediction curve for densification factor ($\Delta\rho_f/\Delta\rho_{max}$) versus heat treatment time (t) for experimental results and comparison of predicted density with experimental density.

3.5.1 Sintering Time Constants

Experimental data for densification of SHS produced Al_2O_3/TiB_2 powders was used to plot the natural logarithm of one minus $\Delta\rho_f/\Delta\rho_{max}$ versus heat treatment time (t) for different time regimes at 1500°C. Excel's built in fit function was used to determine slopes for each time regime and STCs were calculated from the slopes according to Equation 3.21. Due to difficulties in producing appropriate plots with compounded slopes in Excel, Mathematica was used to produce plots. From the plots, it was possible to determine if SHS produced Al_2O_3/TiB_2 had a single STC or multiple STCs for a specific time regime at 1500°C. Calculated STCs for SHS produced Al_2O_3/TiB_2 were compared with STCs for submicron Al_2O_3 to determine accuracy of predictions and of assumptions used in modeling.

3.5.2 Sintering of Ceramic Matrix Composites

A Mathematica script for producing plots of $\Delta\rho_f/\Delta\rho_{max}$ versus heat treatment time (t) was used to plot experimental data based on Equation 3.22. The script calculated $\Delta\rho_f/\Delta\rho_{max}$ from a single point for change in density from green state to heat treated state ($\Delta\rho_f$) and change in density from green state to full theoretically dense state ($\Delta\rho_{max}$). From there, the script calculated the STC (τ) that was used to calculate β-factor with volume fraction of second phase. Finally, the script plotted $\Delta\rho_f/\Delta\rho_{max}$ versus t for data that was input. Densification values were

calculated from the plots for heat treatment times and temperatures corresponding to experimental data points. The calculated densification values were compared with experimental results to determine model accuracy and validity of using the model to predict densification behavior.

4. Results and Discussion

This chapter discusses results obtained from preliminary experimentation, predicting the densification behavior of SHS produced Al_2O_3/TiB_2, determination of Rate Controlling Diffusion Mechanism (RCDM), determination of activation energy, and model comparisons with experimental data. The preliminary experiments section includes results for SHS product powder characterization, sample formation, heat treatment of carbothermic TiB_2, and preliminary heat treatment of SHS produced Al_2O_3/TiB_2. The predicting densification behavior of SHS produced Al_2O_3/TiB_2 section covers estimation of Sintering Time Constants (STCs) for Al_2O_3/TiB_2 using data for Al_2O_3 and modeling the sintering behavior of Ceramic Matrix Composites (CMCs) using data for manually mixed Al_2O_3/TiB_2. The determination of RCDM and activation energy section describes density, shrinkage, compound identification, structure, morphology, RCDM, and activation energy results obtained from heat treatment of SHS produced Al_2O_3/TiB_2. The theoretical and experimental comparison section explains differences in models for STC and sintering of CMCs with experimental data obtained for heat treatment of SHS produced Al_2O_3/TiB_2.

4.1 Preliminary Experiments

This section focuses on SHS product powder characterization, sample formation, heat treatment of carbothermic TiB_2, and preliminary heat treatment of SHS produced Al_2O_3/TiB_2. The SHS product powder characterization section discusses powder compound identification, particle size measurement, structure, morphology, surface area, and pore volume. The sample formation section explains results obtained from a powder pressing designed experiment and includes results from analytical tools such as Analysis of Variance (ANOVA). The heat treatment of carbothermic TiB_2 section describes results for density, microstructure, and chemical composition within the microstructure for carbothermic TiB_2 heat treated at 1800°C and 2100°C. The preliminary heat treatment of SHS produced Al_2O_3/TiB_2 section covers density, shrinkage, compound identification, structure, and morphology results obtained from heat treatment of SHS produced Al_2O_3/TiB_2 with varied helium gas line pressure.

4.1.1 SHS Product Powder Characterization

This section describes results obtained from compound identification, particle size, structure, morphology, surface area, and pore volume analysis performed on SHS reaction product powders. The compound identification section discusses general XRD trace features and indexing of XRD pattern peaks to determine compounds present in the product powder. The particle size section explains particle size distributions obtained using three indices of refraction. The structure and morphology section covers results obtained from SEM for as milled Al_2O_3/TiB_2 powder particles produced by SHS reaction. The surface area and pore volume section discusses gas adsorption results.

4.1.1.1 Compound Identification

The powder XRD analysis yielded a well defined trace with many peaks as shown in Figure 4.1. Most of the primary peaks occurred between 25° and 70° (2θ). The pattern also showed a small peak at ~16.5° (2θ), which may have indicated trace amounts of a third compound. The large peak at ~44° (2θ) may have indicated a disproportionate amount of one compound within the powder or preferred orientation of the compound.

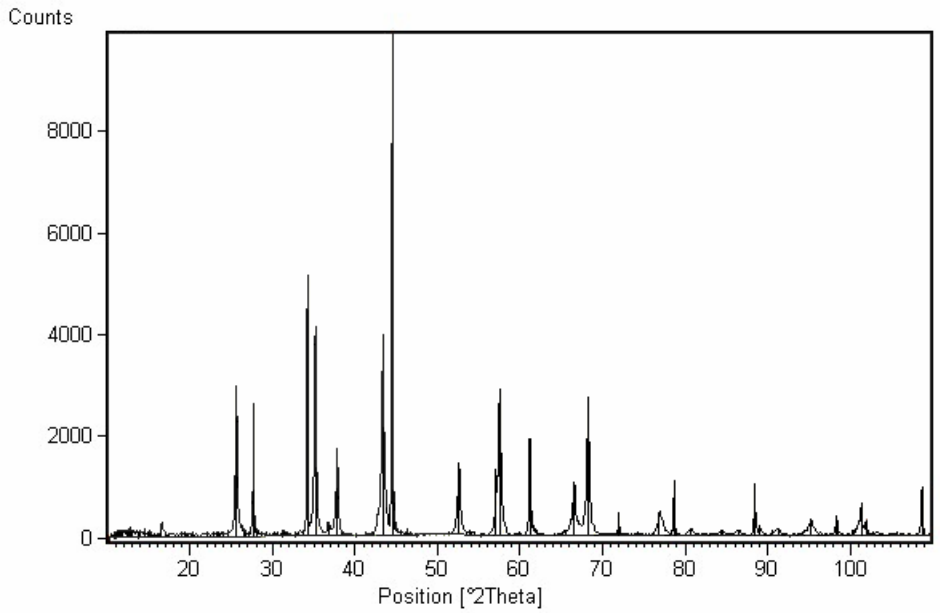

Figure 4.1 – X-ray diffraction pattern for the SHS produced Al_2O_3/TiB_2 dry milled for 30 hours and wet milled for 70 hours.

After indexing, the peaks were found to correspond with Al_2O_3, TiB_2, and $Al_{18}B_4O_{33}$ as shown in Figure 4.2. The pattern suggests the SHS reaction mixture used to produce the

Al_2O_3/TiB_2 product powder was off stoichiometry with excess B_2O_3; or some B_2O_3 reacted with Al_2O_3 producing $Al_{18}B_4O_{33}$ before B_2O_3 was reduced by Al present in the reactant mixture. The $Al_{18}B_4O_{33}$ peaks were observed to be considerably smaller than peaks for Al_2O_3 and TiB_2. The low intensities for $Al_{18}B_4O_{33}$ suggested only small amounts of $Al_{18}B_4O_{33}$ may have been present within the SHS produced Al_2O_3/TiB_2 powders.

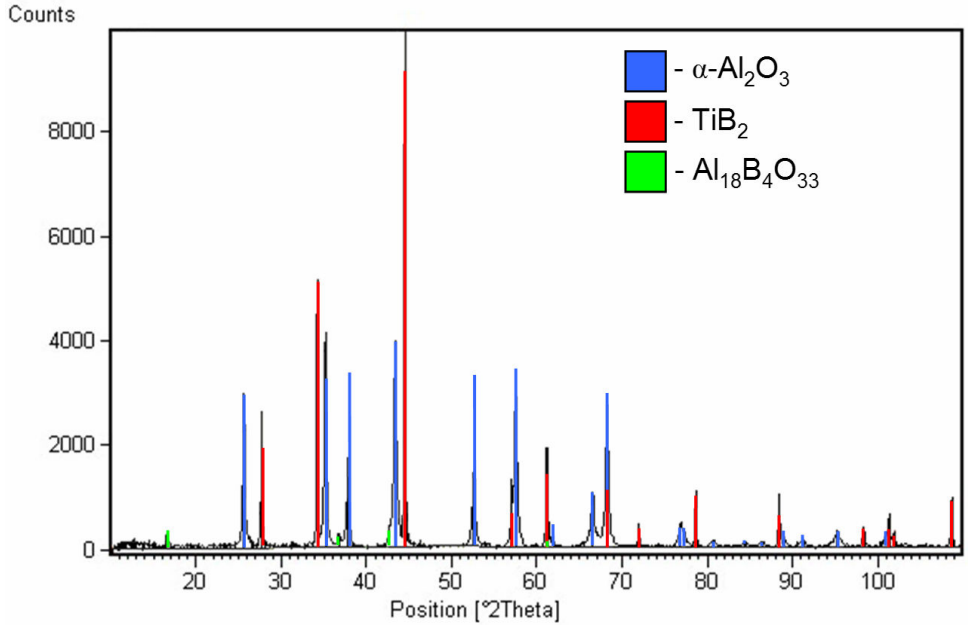

Figure 4.2 – Indexed pattern for SHS produced Al_2O_3/TiB_2 including reference patterns for Al_2O_3, TiB_2, and $Al_{18}B_4O_{33}$.

4.1.1.2 Particle Size

Particle Size Analysis (PSA) using refractive indices based on pure Al_2O_3, pure TiB_2, and a composite rule of mixtures calculation for Al_2O_3/TiB_2 were compared as shown in Figure 4.3. Each index showed a different characteristic behavior and all three indices exhibited wide particle size ranges (0.1 – 400 μm). All three PSA distributions showed bimodal or trimodal distribution.

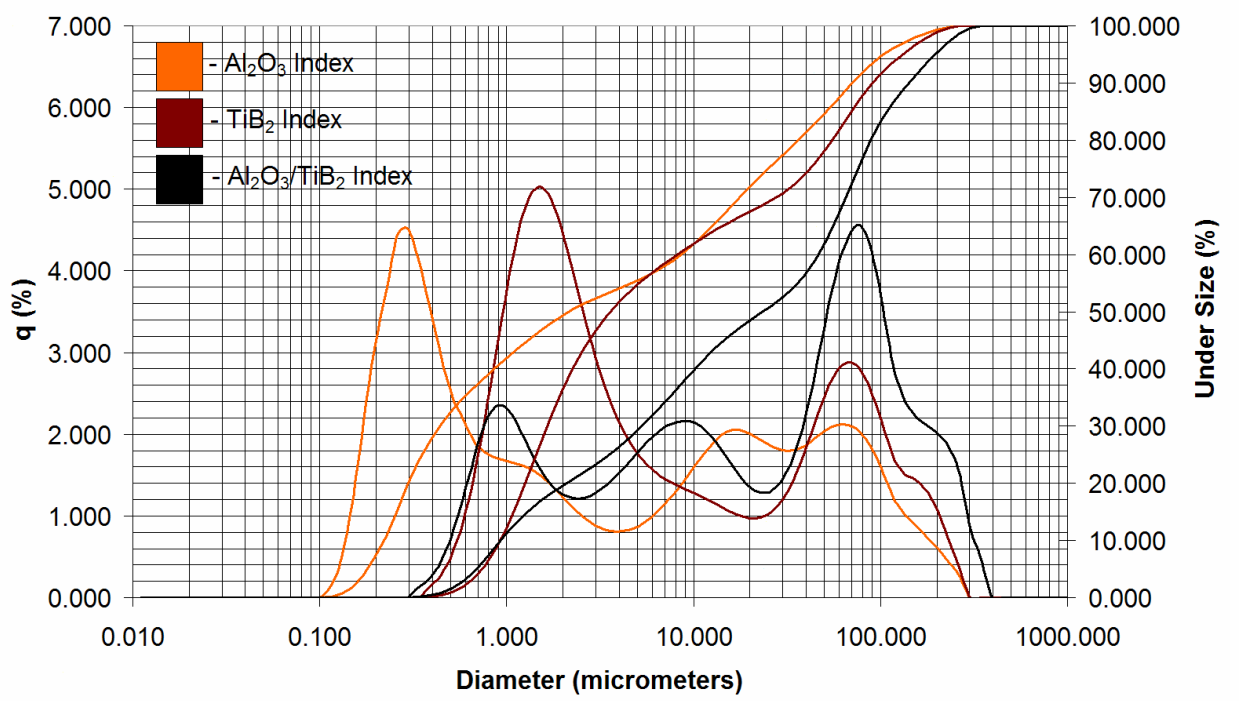

Figure 4.3 – Comparative particle size distribution for Al_2O_3 (orange), TiB_2 (maroon), and Al_2O_3/TiB_2 rule of mixtures (black) refractive indices.

The distributions based on the Al_2O_3 refractive index had peaks centered at 0.3 µm, 17.4 µm, and 67.5 µm. The particle size range for the Al_2O_3 refractive index was between 0.1 µm and 300 µm. The distributions based on the TiB_2 refractive index had peaks centered at 1.5 µm and 67.5 µm. The particle size range for the TiB_2 refractive index was between 0.4 µm and 300 µm. The distributions based on a composite rule of mixtures Al_2O_3/TiB_2 refractive index had peaks centered at 0.9 µm, 9.0 µm, and 750 µm. The particle size range for the Al_2O_3/TiB_2 refractive index was between 0.3 µm and 395 µm. Overall, the particle size distributions for each refractive index tended to be consistent with some fluctuation in the peak heights between samples. The consistency of the distributions meant the distribution shapes for indices used were accurate and followed the shapes shown in Figure 4.3

Average particle size for distributions based on Al_2O_3, TiB_2, and rule of mixtures (Al_2O_3/TiB_2) were 21.7 µm, 28.3 µm, and 48.9 µm respectively as shown in Table 4.1. However, the mode particle size distributions based on Al_2O_3, TiB_2, and rule of mixtures (Al_2O_3/TiB_2) were 0.3 µm, 1.4 µm, and 72.3 µm respectively. Based on the distributions, the percentages of particles under 1 µm for refractive indices of Al_2O_3, TiB_2, and Al_2O_3/TiB_2 were 41%, 12%, and 11% respectively. The percentages of particles under 10 µm for Al_2O_3, TiB_2,

and Al_2O_3/TiB_2 refractive indices were 63%, 62%, and 40% respectively. The percentages of particles under 25 μm for refractive indices based on Al_2O_3, TiB_2, and Al_2O_3/TiB_2 were 76%, 70%, and 51% respectively.

Table 4.1 – Statistical Summary of PSA for Al_2O_3, TiB_2, and Al_2O_3/TiB_2 Refractive Indices

Refractive Index Based On	Mean Particle Size	Mode Particle Size	Percentage Under 1 μm	Percentage Under 10 μm	Percentage Under 25 μm
Al_2O_3	21.7 μm	0.3 μm	41%	63%	76%
TiB_2	28.3 μm	1.4 μm	12%	62%	70%
Al_2O_3/TiB_2	48.9 μm	72.3 μm	11%	40%	51%

Based on analysis of all three distributions, the distributions based on indices for Al_2O_3 and TiB_2 seemed very similar. However, distributions based on the composite rule of mixtures for Al_2O_3/TiB_2 refractive index did not match well with distributions based on Al_2O_3 and TiB_2 refractive indices. The distribution based on the rule of mixtures (labeled Al_2O_3/TiB_2) may not have accurately represented the true distribution of particles for SHS produced Al_2O_3/TiB_2 powder.

The trimodal nature of the particle size distribution may have resulted from the use of ball milling as a particle size reduction technique. The presence of $Al_{18}B_4O_{33}$ and differences in hardness between Al_2O_3, TiB_2, and $Al_{18}B_4O_{33}$ may have created gradation of particle size based on compound. During milling, the $Al_{18}B_4O_{33}$ would have been reduced to the finest particle size because it had the lowest hardness (13.2 GPa) followed by Al_2O_3 (20 GPa) and TiB_2 (36 GPa).

It would be advantageous to determine methods for reducing particle sizes in SHS produced Al_2O_3/TiB_2 while maintaining a more uniform particle size distribution. Since a distribution like the one shown in Figure 4.3 may not be desired for production of uniform microstructures, methods like jet milling may be advantageous to explore. However, the various particle sizes may fill in void spaces within a powder compact resulting in higher green densities than may be possible with more uniform distributions.

4.1.1.3 Structure and Morphology

Initial observation of the SHS produced Al_2O_3/TiB_2 powder revealed that the powder was comprised of masses as shown in Figure 4.4. The masses were chosen to be called particles rather than agglomerates because of the smaller constituents being fused together rather than held together by attractive forces. Observation of individual particles using SEM showed each

individual particle had rough surface features with evidence of fusion. The particles appeared porous but held together by interconnecting bridges. Since the SHS reaction product may be characterized as a friable ceramic material, it was not surprising particles produced from the reaction product were also porous. All particles seemed not to achieve the absolute smallest size based on the high amounts of porosity evident within individual particles. The degree of porosity seen in the particles suggests even smaller particle sizes are highly probable with longer ball milling times or higher energy milling techniques.

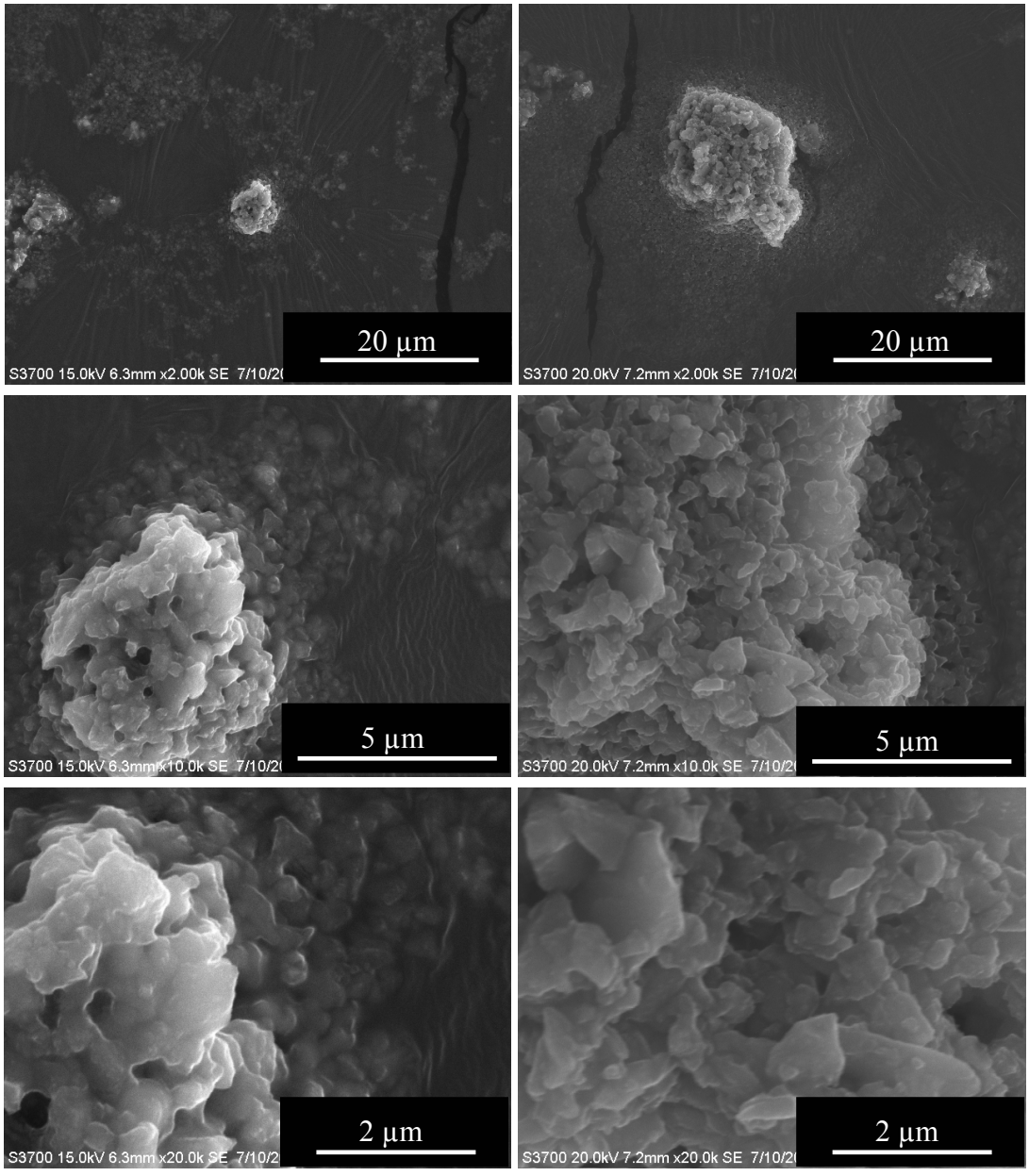

Figure 4.4 - SEM micrographs of a small (left) and a large (right) SHS produced Al_2O_3/TiB_2 particle at increasing magnifications.

Particles tended to be approximately spherical or elliptical in shape with many sharp edges. Based on SEM observations, the surface area for each particle should be large, potentially resulting in high surface energy for smaller particles. A high surface free energy for particles in a powder compact would be a driving force for densification since reducing surface area would reduce surface energy for a given surface energy density.

When compared with data from PSA, SEM micrographs confirmed a wide particle size range. In addition, it seemed probable the PSA results may have been influenced by agglomeration since no particles larger than 100 μm were found during SEM imaging. Based on the frequency of particle sizes observed using SEM, the particle size distribution based on Al_2O_3 seemed to be the most appropriate distribution.

4.1.1.4 Particle Surface Area and Pore Volume

Gas adsorption techniques for surface area and pore volume analysis of SHS produced Al_2O_3/TiB_2 powders showed a wide range of surface areas and pore volumes as shown in Table 4.2. A high variation in surface area and pore volume data confirmed the wide range of particle sizes seen in PSA and SEM. Data on pore volume also agreed with SEM and suggested SHS produced Al_2O_3/TiB_2 powder particles had a high degree of porosity. The ranges for surface area and pore volume seen in Table 4.2 were a result of various methods used by the analysis software for calculating surface area and pore volume based on gas adsorption data.

Table 4.2 – Surface Area and Pore Volume from Gas Adsorption

Milling Time	Surface Area (m^2/g)	Pore Volume (cm^3/g)
100 Hours	15.80 – 274.30	0.0217 – 0.128

4.1.2 Sample Formation

Pressed sample densities based on the experimental design array shown in Table 4.3 averaged 2.36 g/cm^3 (57.33% theoretical density), as shown in Table 4.4. Samples pressed using configuration 1 averaged 2.29 g/cm^3 (55.49% theoretical density), configuration 2 averaged 2.40 g/cm^3 (58.20% theoretical density), configuration 3 averaged 2.45 g/cm^3 (59.47% theoretical density), and configuration 4 averaged 2.31 g/cm^3 (56.17% theoretical density). Main effects plots were constructed for pressing pressure, action type, and drying of as processed powders as shown in Figures 4.5 – 4.7. The main effects plots suggested powder drying was the most significant factor tested followed by pressing pressure and action type.

Table 4.3 – Pressing Designed Experiment L4 Orthogonal Array

Configuration	Pressing Pressure (psi)	Action Type	Powder Dried
1	10,000	Single	Yes
2	10,000	Double	No
3	20,000	Single	No
4	20,000	Double	Yes

Table 4.4 – Al_2O_3/TiB_2 Designed Experiment Raw Data

Configuration	Run 1 (g/cm^3)	Run 2 (g/cm^3)	Run 3 (g/cm^3)	Run 4 (g/cm^3)	Run 5 (g/cm^3)	Average (g/cm^3)	% Theoretical
1	2.25	2.29	2.25	2.32	2.32	2.29	55.49%
2	2.43	2.40	2.38	2.39	2.39	2.40	58.20%
3	2.46	2.47	2.43	2.45	2.44	2.45	59.47%
4	2.45	2.23	2.15	2.42	2.32	2.31	56.17%

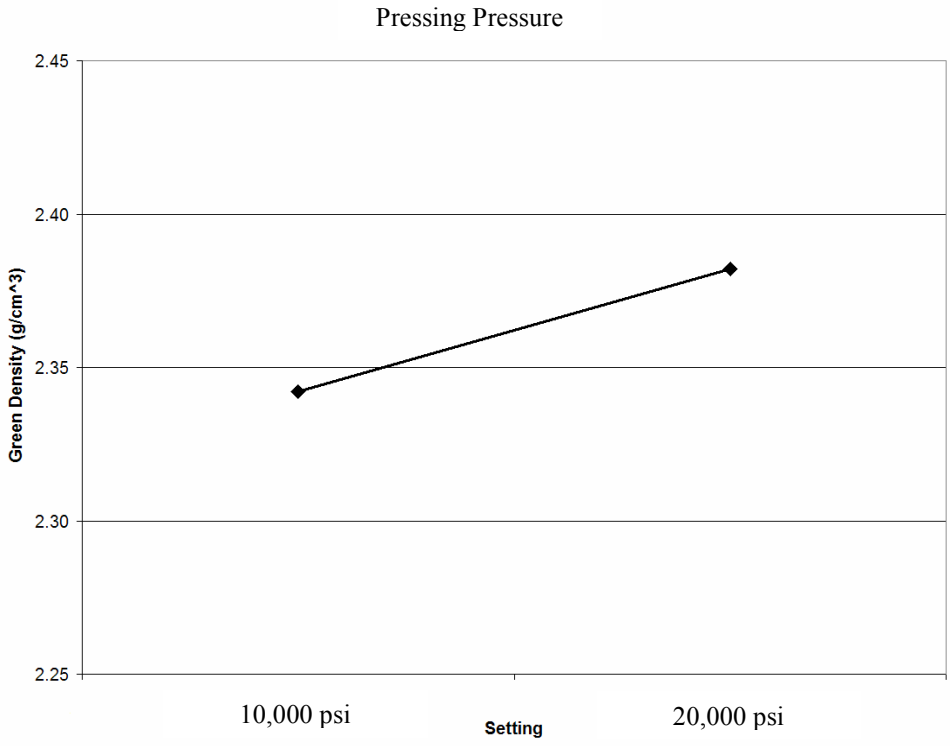

Figure 4.5 – Main effect plot for pressing pressure from the pressing designed experiment.

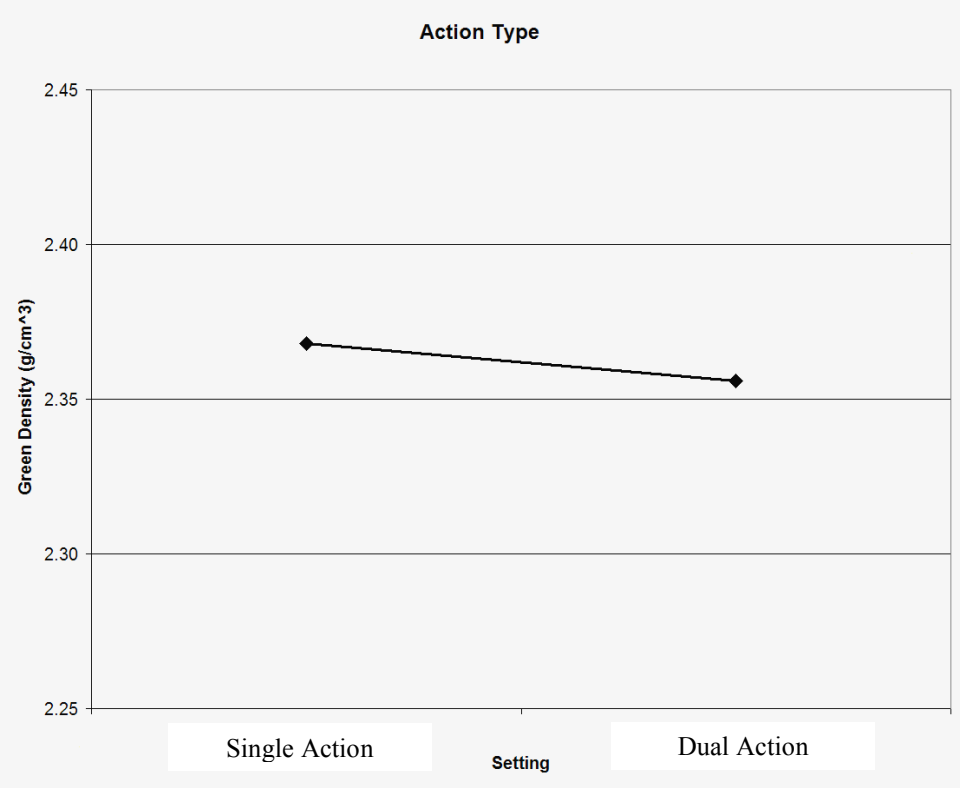

Figure 4.6 – Main effect plot for action type from the pressing designed experiment.

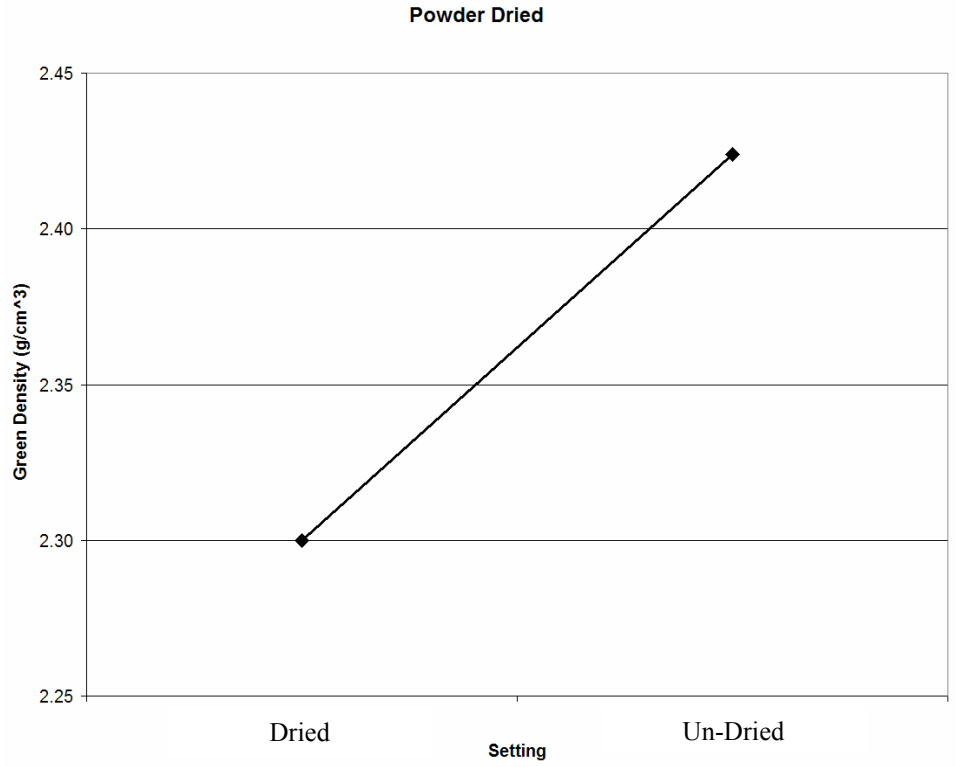

Figure 4.7 – Main effect plot for powder drying from the pressing designed experiment.

From the data in Table 4.4, ANOVA was completed and showed a variance of 0.008 for pressing pressure, 0.001 for action type, and 0.077 for drying the as processed powder as shown in Table 4.5. The data suggested action mode may not have been significant to the green density. According to ANOVA performed, powder drying had a 99% confidence interval for significance.

Table 4.5 - ANOVA Table for Al_2O_3/TiB_2 Pressing Experiments

Source	SS	DOF	V	$F_{calc.}$	Table F-Value Exceeded	C.I.	P
Pressing Pressure	0.008	1	0.008	1.80	-	-	2.27%
Action Type	0.001	1	0.001	0.16	-	-	-
Powder Dried	0.077	1	0.077	17.30	5.29	99%	46.22%
Error	0.071	16	0.004	-	-	-	-
Total	0.352	19	-	-	-	-	48.49%

The results showed moisture content of powder played a significant role in producing high green densities from pressing. Further experimentation would be needed to determine how much moisture content affected green densities in pressing Al_2O_3/TiB_2. The total influence percentage was found to be 48.49%; meaning 51.51% of the parameters affecting the green density of pressed Al_2O_3/TiB_2 pellets were not identified. When error was pooled, powder drying was still the only significant factor but calculated influence percentage increased to 97.48% as shown in Table 4.6.

Table 4.6 – ANOVA Table for Al_2O_3/TiB_2 Pressing Experiments with Error Pooled

Source	SS	DOF	V	$F_{calc.}$	Table F-Value Exceeded	C.I.	P
Pressing Pressure	0.008	1	0.008	11.11	-	-	8.50%
Powder Dried	0.077	1	0.077	106.78	49.50	90%	88.97%
Pooled Error	0.001	1	0.001	-	-	-	-
Total	0.086	3	-	-	-	-	97.48%

The optimal setting was calculated to be a pressing pressure of 20,000 psi using a single action pressing mode and as processed powder. From the analysis, a density of ~2.45 g/cm^3 (60.49% theoretical density) should be achieved using the settings as shown in Table 4.7. The

use of single action pressing versus dual action pressing seemed to have only a slight effect on predicted density as expected from ANOVA; however, the ease of using a single action mode made the optimum pressing settings more attractive.

Table 4.7 - Predicted Process Averages for Pressing Al_2O_3/TiB_2 Pellets

Pressing Pressure (psi)	Action Mode	Powder Dried	Predicted Density (g/cm^3)	Predicted Percent Theoretical
20,000	Single	No	2.45	60.49%
20,000	Dual	No	2.44	60.20%
10,000	Single	No	2.41	59.51%
10,000	Dual	No	2.40	59.21%
20,000	Single	Yes	2.33	57.43%
20,000	Dual	Yes	2.31	57.14%
10,000	Single	Yes	2.29	56.44%
10,000	Dual	Yes	2.27	56.15%

Data from the confirmation experiment showed a green density average of 2.46 ± 0.02 g/cm^3 as shown in Table 4.8. The prediction from Table 4.7 falls within the process average confidence interval range. Since the prediction falls within range, the prediction was good and the model was validated despite the system not being completely understood. Since the model was validated, the predicted optimal setting should produce the highest green densities from combinations of factors and levels studied.

Table 4.8. - Process Average and Confidence Interval for Pressing Al_2O_3/TiB_2

Green Density Average	2.46 g/cm^3
Standard Deviation	0.02 g/cm^3
Conference Interval (CI)	0.03 g/cm^3
CI Minimum	2.43 g/cm^3
CI Maximum	2.49 g/cm^3
Predicted Green Density	2.45 g/cm^3

When the hydraulic press was manually actuated to maintain peak pressing pressure during springback, density gradients were created in the sample as shown in Figure 4.8. Each additional application of pressure during springback increased the density of the bottom sample region. As density increased, the bottom region acted as an extension of the ram providing a hard surface for compaction of powders above. The gradients resulted in warped heat treated samples because rates of densification throughout the sample were affected by the density gradients. Allowing the samples to springback during pressing significantly reduced density

gradients within the samples resulting in samples with very little warping and virtually flat surfaces after heat treatment. However, when springback was allowed during pressing, the average green density of pressed samples decreased to 2.12 ± 0.02 g/cm^3 (~51.5% theoretical).

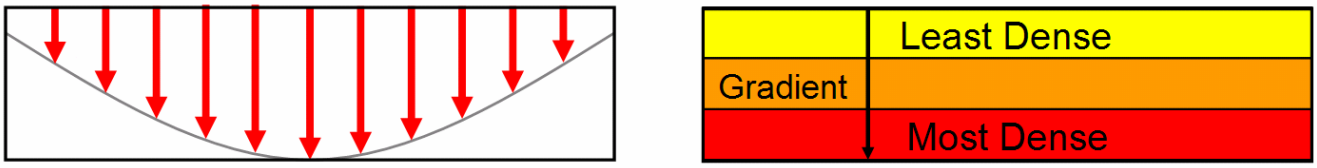

Figure 4.8 – Density gradients created from uniaxial pressing (left) and density layering (right) created by maintaining pressing pressure rather than allowing for springback.

4.1.3 Heat Treatment of Carbothermic TiB_2

Pressed carbothermic TiB_2 samples had an average green density of 2.50 g/cm^3. After heat treatment at 1800°C for 30 minutes, carbothermic TiB_2 samples had an average density of 2.50 g/cm^3 (55.30% theoretical density) as shown in Table 4.9. The samples seemed consistent in density with the exception of CT0100208002, which showed a higher density. There were no other noticeable differences between the samples. The sample's position on the sample holder may have affected final density; however, the data showed no observable trend.

Table 4.9 – Densities of Carbothermic TiB_2 Heat Treated at 1800°C for 30 Minutes

Sample ID	Density (g/cm^3)	% Theoretical
CT122107010	2.49	55.10%
CT122107017	2.49	54.98%
CT010208001	2.46	54.49%
CT010208002	2.61	57.67%
CT010208003	2.45	54.24%
AVERAGE	2.50	55.30%

Heat treated carbothermic TiB_2 sample porosity observed using SEM appeared to be open porosity as shown in Figure 4.9. The SEM images showed evidence of beginning stages of densification by bulk diffusion such as necking. If samples were held at temperature for longer times or if heat treatment temperature were increased more significant densification might be observed.

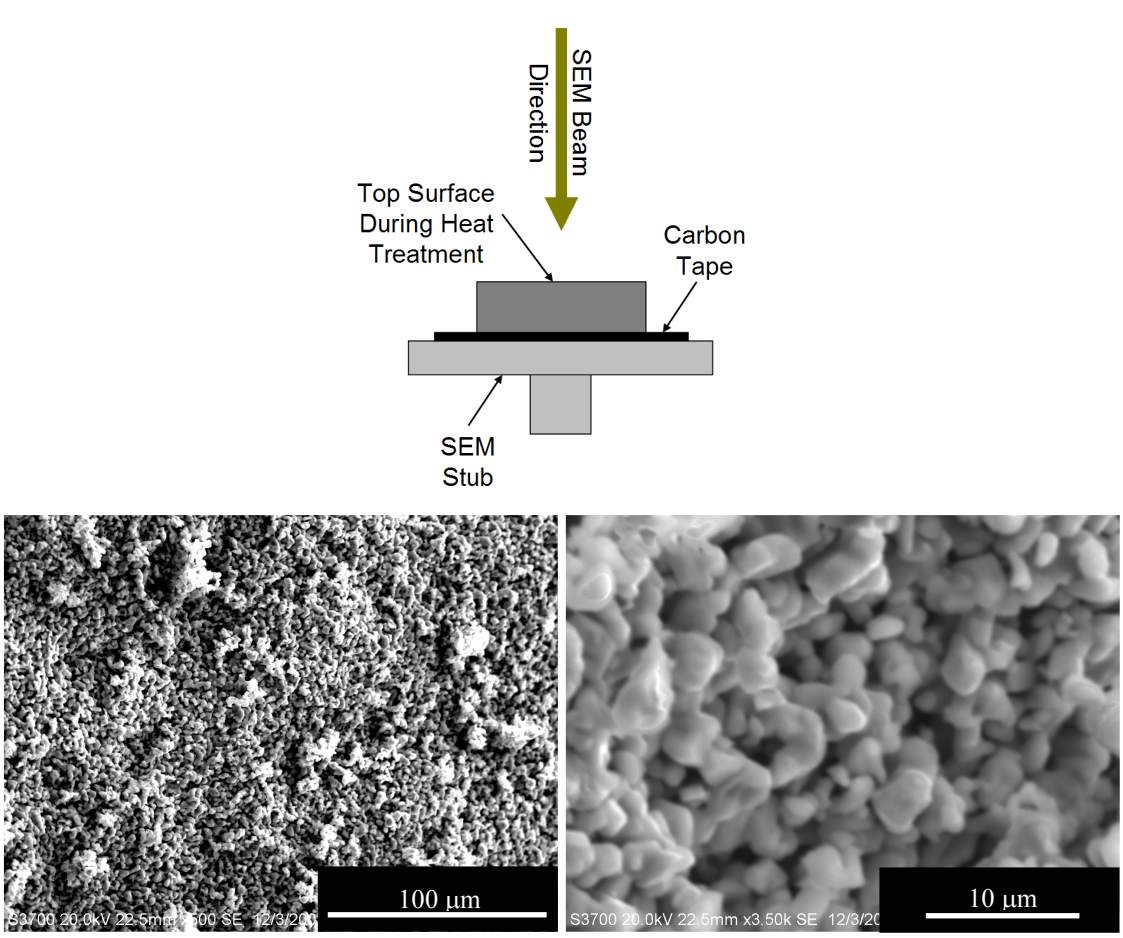

Figure 4.9 – Micrographs of general porosity (left) and evidence of densification in carbothermic TiB_2 (right) heat treated at 1800°C for 30 minutes.

EDS results at unique regions of the microstructure revealed carbon and oxygen contained in very interesting microstructural features as shown in Figure 4.10. Normally, the regions would be considered artifacts; however, the regions were observed in all heat treated carbothermic TiB_2 samples. Since the samples were made using carbothermic TiB_2 and both elements were found in the MSDS report included with the powder, the formations may be a result of carbothermic processing impurities.

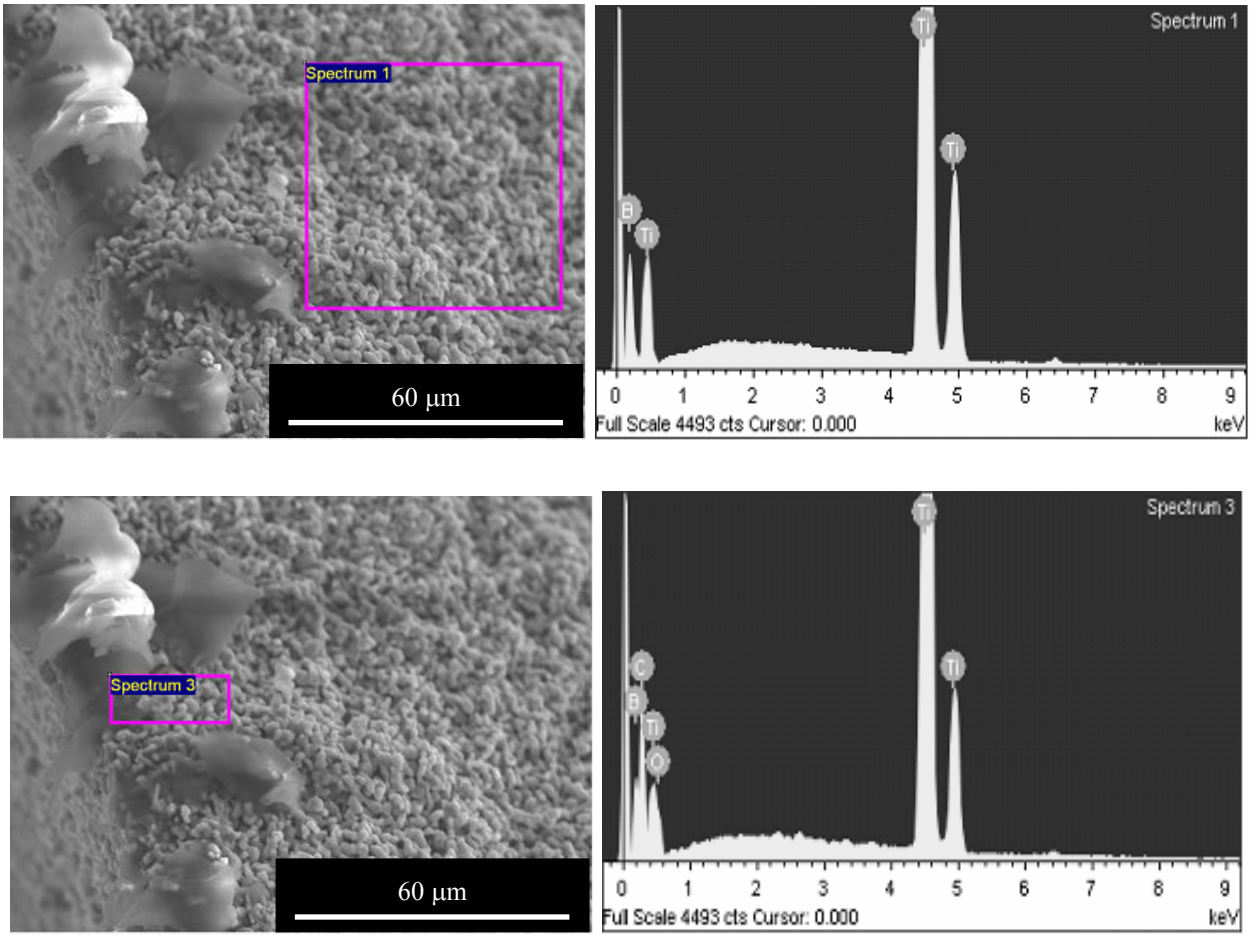

Figure 4.10 – Micrographs and EDS spectra near an impure region within the heat treated carbothermic TiB_2 microstructure.

After heat treating carbothermic TiB_2 at 2100°C for 60 minutes, samples had an average density of 2.65 g/cm^3, which is 58.65% of theoretical density as shown in Table 4.10. An apparent difference in final densities of the heat treated samples was observed; however, no noticeable differences in microstructure or physical appearance were observed. Further study may be required to determine the source of differences between the samples. The heat treated carbothermic TiB_2 samples still showed porosity. The microstructure for carbothermic TiB_2 samples heat treated at 2100°C for 60 minutes appeared to be very different from samples heat treated at 1800°C for 30 minutes, as shown in Figure 4.11.

Table 4.10 – Densities of Samples Heat Treated at 2100°C for 60 Minutes

Sample ID	Density (g/cm^3)	% Theoretical
CT113007002	2.55	56.42%
CT113007003	2.75	60.89%
AVERAGE	2.65	58.65%

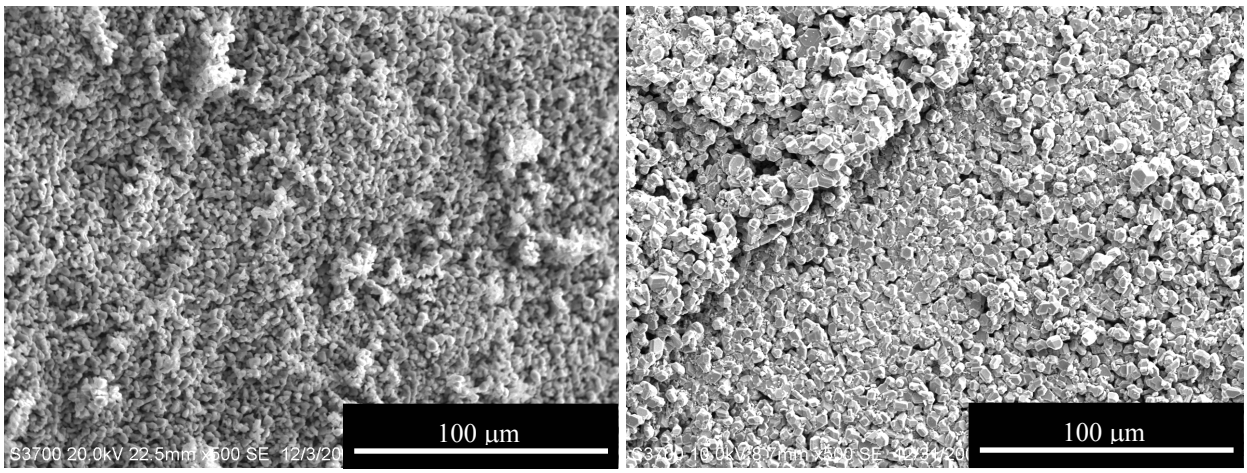

Figure 4.11 – SEM micrographs of the carbothermic TiB_2 microstructure after being heat treated at 1800ºC for 30 minutes (left) and 2100ºC for 60 minutes (right).

While observing carbothermic TiB_2 samples heat treated at 2100°C for 60 minutes using SEM, several areas showed masses larger than the initial particle size of the powders as shown in Figure 4.12. Upon further investigation, the masses showed significant evidence of densification taking place within the samples during heat treatment as evidenced by formation of large fused masses within the microstructure. However, the sample surface also showed evidence of formations with similar appearance and EDS traces as samples heat treated at 1800°C for 30 minutes as shown in Figure 4.13.

After EDS and further observation, the formations were found to have the same general morphology and EDS spectra in carbothermic TiB_2 samples heat treated at 1800°C for 30 minutes and 2100°C for 60 minutes. One major difference was impurity formations found in the samples heat treated at 1800°C for 30 minutes were only found on sample edges; however, formations were found throughout the surfaces of samples heat treated at 2100°C for 60 minutes.

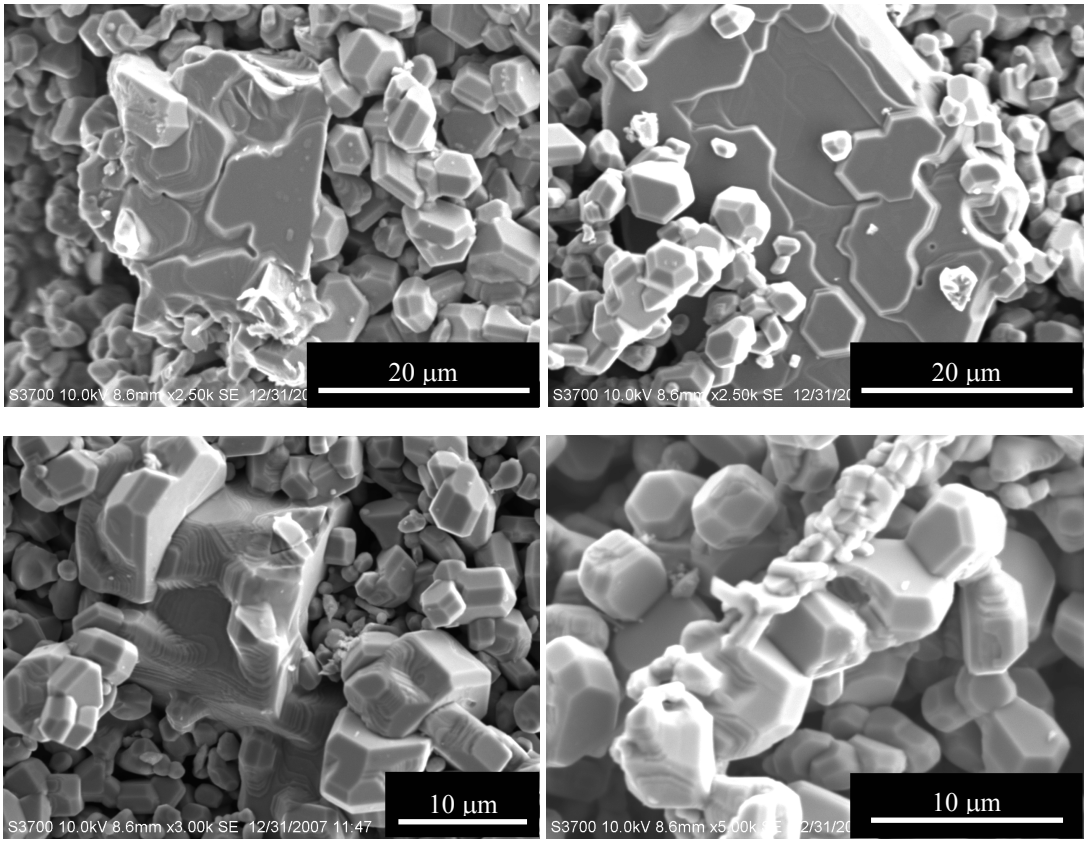

Figure 4.12 – SEM micrographs of carbothermic TiB_2 from a sample heat treated at 2100ºC for 60 minutes.

Higher temperatures, while improving densification conditions, may have provided the necessary energy for formation of the carbonaceous structures observed on the material's surface. Since sharp edges on a material have a higher surface energy than the rest of the free surface, the formations would be expected to appear along the material's edges first. The edge formations would also be expected to show up at lower temperatures than formations on other surfaces.

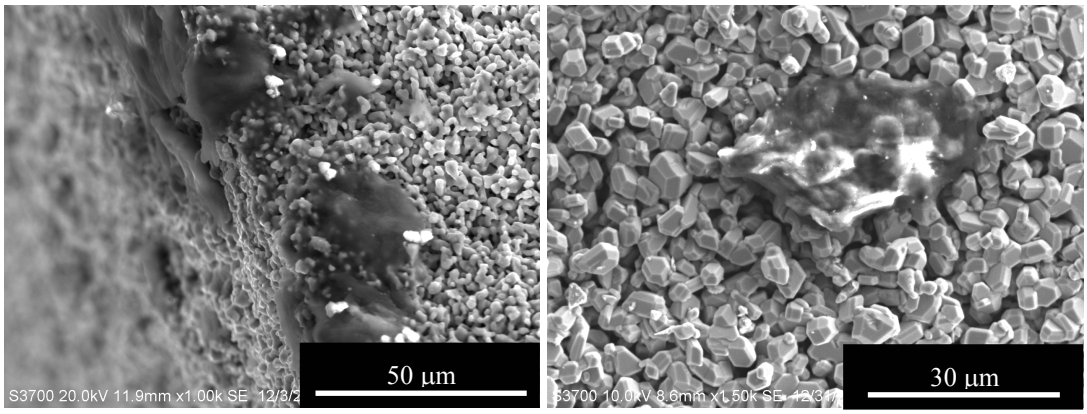

Figure 4.13 – Impurity formations in carbothermic TiB_2 samples heat treated at 1800°C for 30 minutes (left) and 2100°C for 60 minutes (right).

4.1.4 Preliminary Heat Treatment of SHS Produced Al_2O_3/TiB_2

This section discusses density, shrinkage, compound identification, structure, and morphology of SHS produced Al_2O_3/TiB_2 samples heat treated with different inert gas line pressures. The density and shrinkage section describes differences in density, shrinkage, and porosity based on changes in inert gas line pressures. The compound identification section discusses compounds formed within samples heat treated at very low line pressures where oxidizing conditions may have been present. The structure and morphology section displays microstructural features of samples heat treated at very low line pressures.

Based on observations from initially heated treated samples, inert gas line pressure was found to be critical in controlling tube temperature and final sample appearance. High line pressure of inert gas created a cooling effect within the tube requiring additional manual temperature correction to reach desired temperatures. However, when line pressure was too low, air was allowed into the tube and several white spots formed on the sample surface as shown in Figure 4.14.

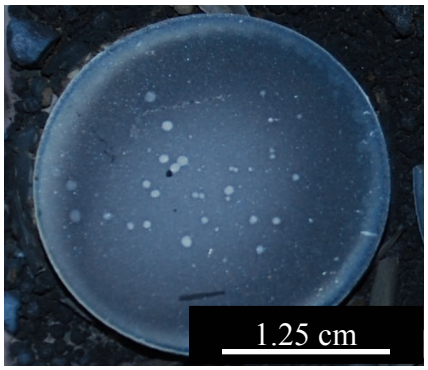

Figure 4.14 – Representative SHS produced Al_2O_3/TiB_2 sample after heat treatment at ~1500°C for 60 minutes at a line pressure below 5 psig.

A line pressure of 15 psig resulted in a temperature difference of 130°C between the thermocouple near the heating elements and the thermocouple inside the tube. It was believed the flowing gas was considerably cooler than the tube's atmosphere creating a cooling effect at higher inert gas line pressures. When line pressure was reduced below 5 psig, temperature difference between the thermocouple near the heating elements and the thermocouple inside the tube was reduced to 40°C and was consistently reproducible.

4.1.4.1 Density and Shrinkage

SHS produced Al_2O_3/TiB_2 samples heat treated with a line pressure of 15 psig had an average density of 2.86 ± 0.02 g/cm^3 and samples heat treated with a line pressure below 5 psig had an average density of 3.40 ± 0.07 g/cm^3 as shown in Table 4.11. As expected, the average density and impervious volume were highest for samples heat treated at lower line pressure because of reduced cooling effect. Similarly, samples heat treated at lower line pressure had lowest pore volume, apparent porosity, and liquid absorption.

Table 4.11 – Average Archimedes' Calculations for Preliminary SHS Produced Al_2O_3/TiB_2 Experiments

Line Pressure	Average Immersion Bulk Density (g/cm^3)	Average Pore Volume (cm^3)	Average Impervious Volume (cm^3)	Average Apparent Porosity (%)	Average Liquid Absorption (%)	Average Volume Shrinkage (%)
< 5 psig	3.40 ± 0.07	0.06 ± 0.05	1.67 ± 0.01	3.63 ± 2.87	1.08 ± 0.88	38.87 ± 1.98
15 psig	2.86 ± 0.02	0.50 ± 0.01	1.55 ± 0.01	24.39 ± 0.47	8.53 ± 0.21	27.49 ± 1.31

4.1.4.2 Compound Identification

Analysis from a SHS produced Al_2O_3/TiB_2 sample exposed to an oxidizing environment during furnace cooling showed the presence of Al_2O_3, TiB_2, and intense peaks for $Al_{18}B_4O_{33}$ as shown in Figures 4.15 and 4.16. The diffraction pattern also showed a hump centered around 12°. The hump seemed to indicate the presence of an amorphous compound within the sample.

Based on analysis, the amorphous compound may be from residual B_2O_3 from the initial SHS reaction or from the aluminum borate separating into an $Al_{18}B_4O_{33\ (s)} + B_2O_{3\ (l)}$ above 1000°C. Since B_2O_3 was not found in the SHS reaction product powders, the amorphous compound was probably due to $Al_{18}B_4O_{33\ (s)} + B_2O_{3\ (l)}$ formation. When the SHS produced Al_2O_3/TiB_2 was exposed to an oxidizing environment, the preferred oxide compound formation appeared to be $Al_{18}B_4O_{33}$. However, it was unclear whether the $Al_{18}B_4O_{33}$ formed directly during oxidation or if TiB_2 oxidized to form B_2O_3 and then reacted with Al_2O_3 in the sample to create $Al_{18}B_4O_{33}$.

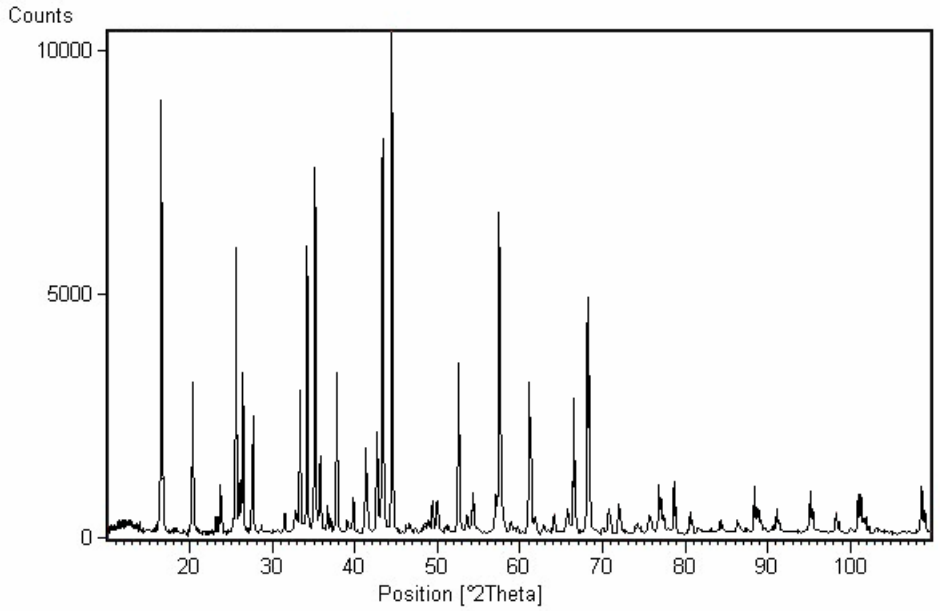

Figure 4.15 – Pattern for SHS produced Al_2O_3/TiB_2 heat treated at ~1500°C for 60 minutes and exposed to air (line pressure below 5 psig) above 1000°C on cooling.

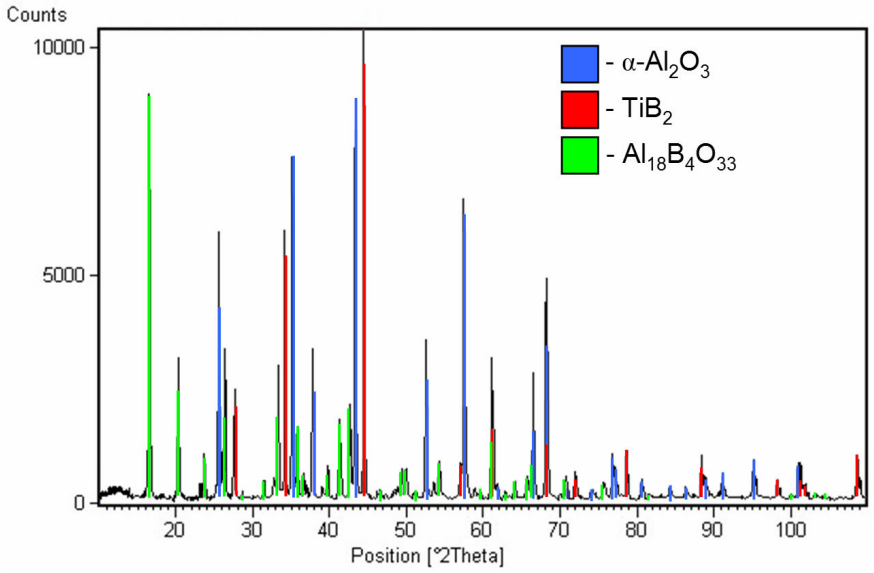

Figure 4.16 – Pattern for SHS produced Al_2O_3/TiB_2 heat treated at ~1500°C for 60 minutes and exposed to air (line pressure below 5 psig) above 1000°C on cooling with patterns for Al_2O_3, TiB_2, and $Al_{18}B_4O_{33}$.

4.1.4.3 Structure and Morphology

Samples exposed to an oxidizing environment during cooling were observed using SEM. The oxidized samples showed a significant amount of amorphous structure on sample top and bottom surfaces with seemingly crystalline features underneath. Oxidized samples top surfaces were observed using SEM and were compared with bottom surfaces as shown in Figure 4.17.

Both surfaces showed signs of amorphous structure covering a more crystalline structure. The top surface seemed considerably more porous and exhibited smoother sub-surfaces than the bottom surface. The top surface also showed evidence of crystallite formation. It seemed probable the amorphous structure observed was from $Al_{18}B_4O_{33\ (s)} + B_2O_{3\ (l)}$ formed above 1000°C. Since samples were exposed to an oxidizing environment, excess oxygen was present to allow formation of boron oxides and aluminum borates along sample surfaces. Additional micrographs including cross sections of samples exposed to an oxidizing environment during heat treatment may be found in Appendix E.

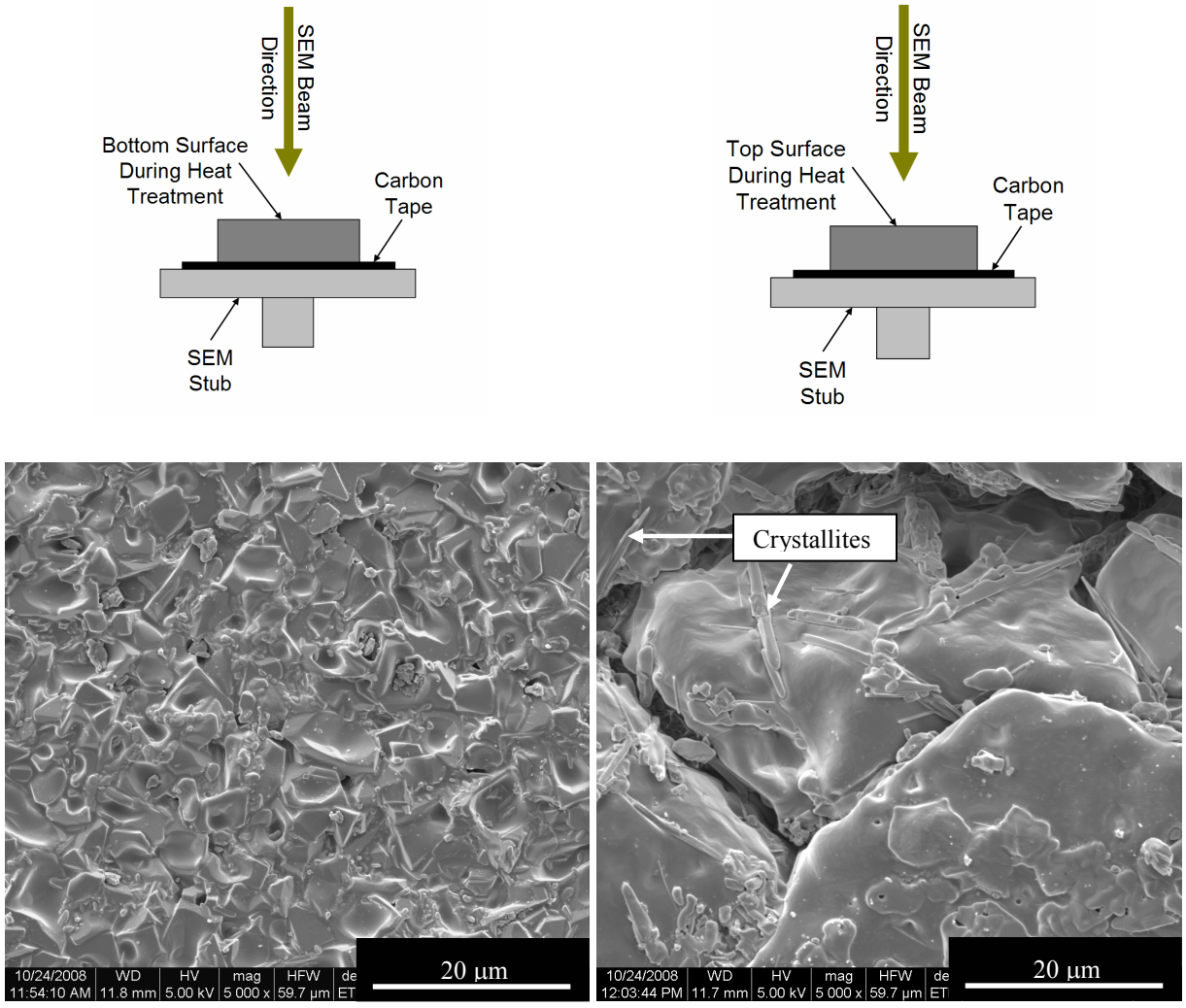

Figure 4.17 – Micrographs of the bottom surface (left) and top surface (right) of a sample of SHS produced Al_2O_3/TiB_2 exposed to air during cooling from 1500°C.

The amorphous layers observed on the oxidized samples were probably responsible for the low calculated pore volume, apparent density, and liquid absorption determined by Archimedes' methods (Table 4.10). Since Archimedes' methods were based on infiltration of pore spaces by a fluid, the presence of the amorphous surface layer may have prevented penetration of the fluid into pores within the sample resulting in low liquid absorption. The amorphous layer may have provided protection against further oxidation by filling in open porosity and sealing off direct oxygen access to the samples' bulk. Further research should be pursued to determine if pressurelessly densified SHS produced Al_2O_3/TiB_2 may form a passivating layer in oxidizing environments.

4.2 Predicting the Densification Behavior of SHS Produced Al_2O_3/TiB_2

This section describes results obtained from models for STCs and sintering of CMCs. The STCs section discusses results from calculations of STCs for Al_2O_3 at 1200°C, 1300°C, and 1350°C. The sintering of CMCs section explains the expected densification behavior for Al_2O_3/TiB_2 at 1700°C and 1800°C based on data for manually mixed Al_2O_3/TiB_2.

4.2.1 Sintering Time Constants

The time constant models run for Al_2O_3 at 1200°C, 1300°C, and 1350°C showed the presence of a short and long time constant as shown in Figure 4.18. The long STCs calculated for Al_2O_3 were 666.7. min, 199.2 min, and 49.4 min. The short STCs calculated were 204.1 min, 61.0 min, and 15.1 min. Since two constants were present, the heat treatment time should determine which constant is dominant; and therefore, which stage of densification samples will reach. STCs decreased with increased heat treatment temperature; indicating higher heat treatment temperatures, should lead to more rapid progress through densification stages. Based on figure 4.18, the long STC should dominate for heat treatment times greater than 30 minutes and heat treatment temperatures greater than 1300°C if the TiB_2 phase is non-densifying. Since the particle size of the SHS produced Al_2O_3/TiB_2 is larger than for the Al_2O_3, the SHS produced Al_2O_3/TiB_2 should densify more slowly than the smaller Al_2O_3. The slower densification of Al_2O_3/TiB_2 should result in long STCs for the SHS produced Al_2O_3/TiB_2 as predicted by modeling of Al_2O_3.

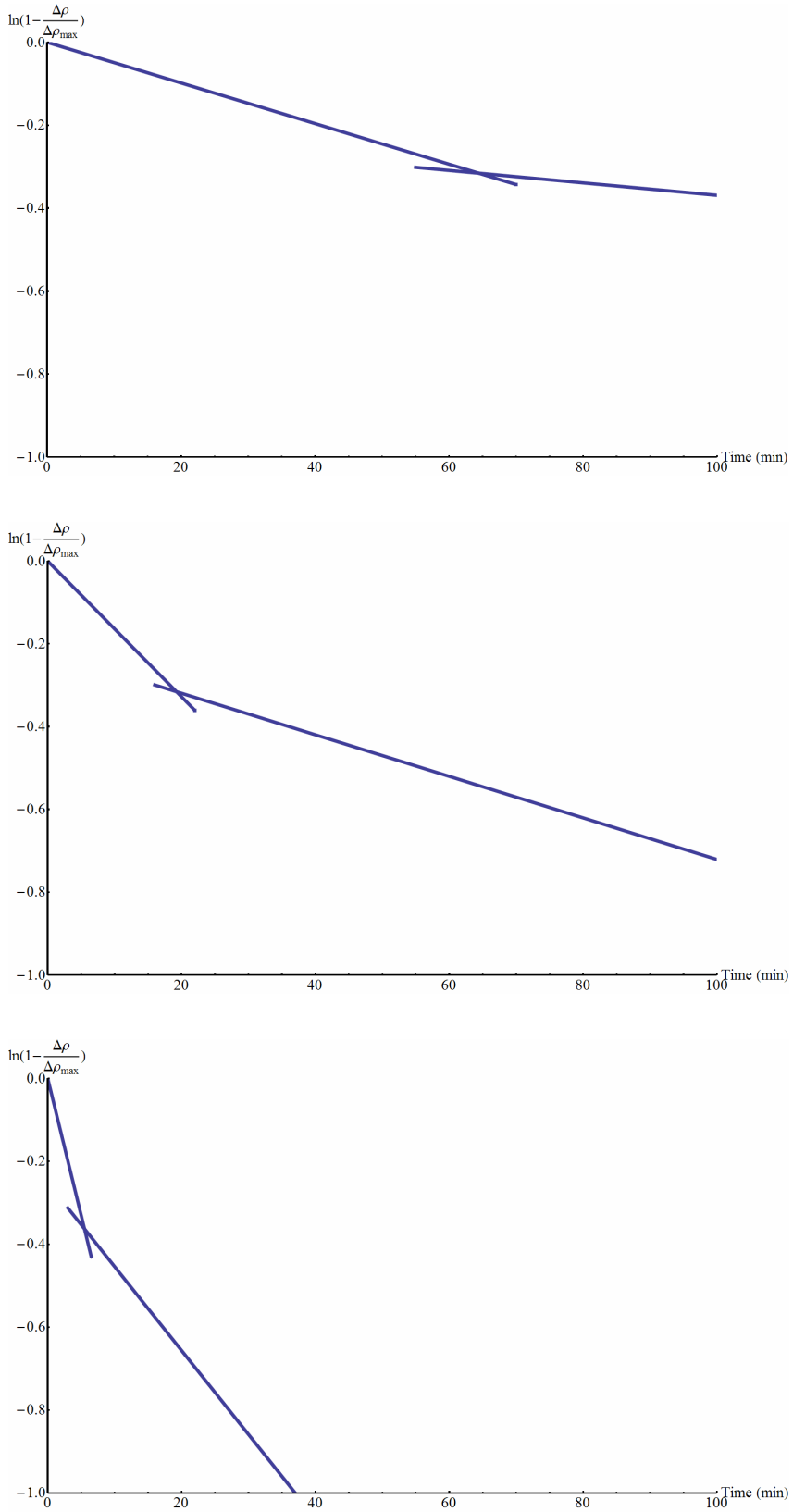

Figure 4.18 – Plots used to calculate STCs for Al_2O_3 heat treated at 1200°C (top), 1300°C (middle), and 1350°C (bottom) based on data from the ASM Materials Handbook: Volume 4.

4.2.2 Sintering of Ceramic Matrix Composites

Based on data from Matsushita et al., STCs for manually mixed Al_2O_3/TiB_2 of various TiB_2 volume fractions (f) were calculated for heat treatments at 1700°C and 1800°C. STC plots and equations for each volume fraction considered are shown in Figures 4.19 and 4.20. STC values calculated for manually mixed Al_2O_3/TiB_2 heat treated at 1700°C were 19.4 min (f = 0), 25.7 min (f = 0.09), 34.8 min (f = 0.13), and 52.9 min (f = 0.47). For heat treatments of manually mixed Al_2O_3/TiB_2 at 1800°C, STC values were calculated to be 19.4 min (f = 0), 25.7 min (f = 0.09), 31.7 min (f = 0.13), 38.0 min (f = 0.47).

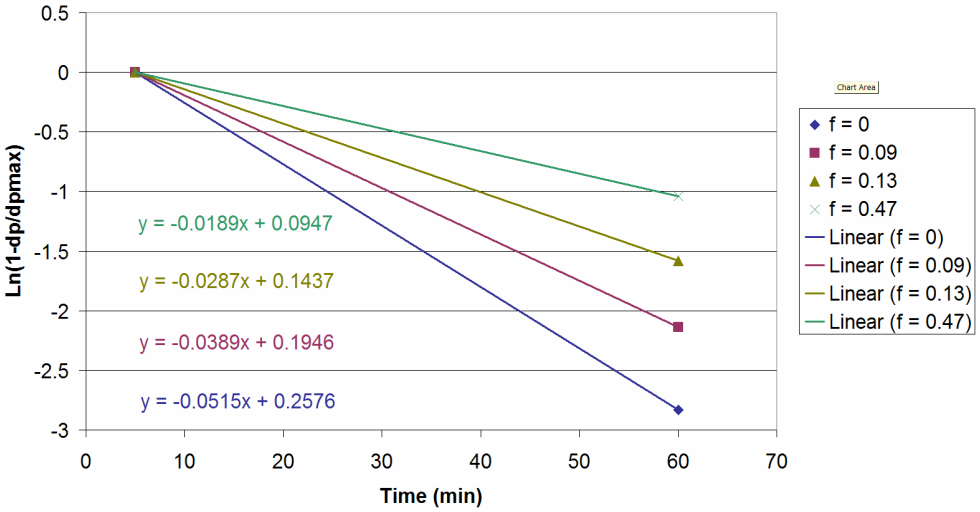

Figure 4.19 – Plots used to calculate STCs for manually mixed Al_2O_3/TiB_2 heat treated at 1700°C based on data from Matsushita et al.

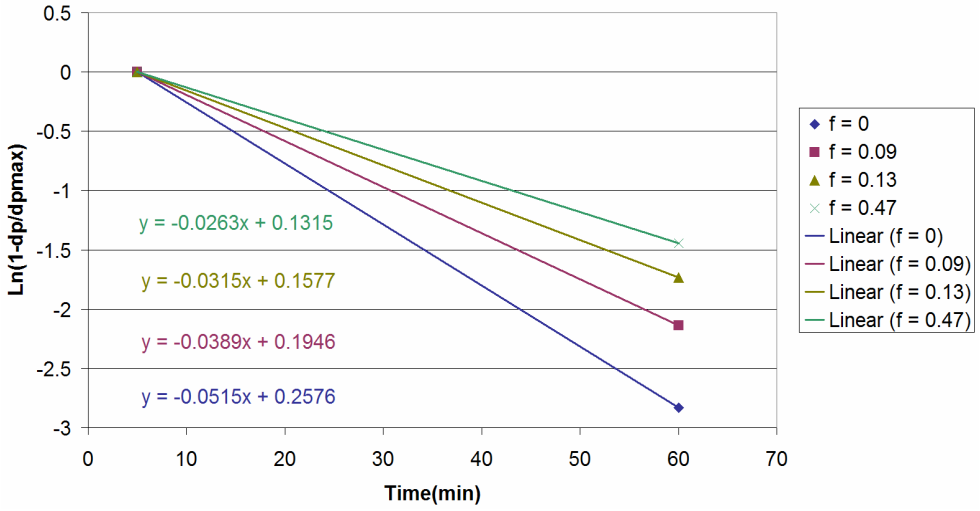

Figure 4.20 – Plots used to calculate STCs for manually mixed Al_2O_3/TiB_2 heat treated at 1800°C based on data from Matsushita et al.

Increasing heat treatment temperature seemed to have greater effect on STCs for volume fractions above 0.10. Based on preliminary heat treatments of TiB_2, change in STC with temperature for volume fractions above 0.10 may be due to localized densification of the TiB_2 reinforcement. If localized densification of TiB_2 occurred, the STC values could be reduced because densification occurred simultaneously in both matrix and reinforcement. Based on calculated STCs for manually mixed Al_2O_3/TiB_2, the effect of a reinforcement phase on densification may be clearly seen. However, due to lack of intermediate or longer heat treatment time data, it was not possible to determine the presence of multiple STCs within manually mixed Al_2O_3/TiB_2 heat treated at 1700°C and 1800°C.

Since STC data for manually mixed Al_2O_3/TiB_2 showed decreased densification of Al_2O_3/TiB_2 with increased volume fraction of TiB_2, derived plots of densification factor versus heat treatment time were created for various volume fractions as shown in Figure 4.21 and 4.22. As heat treatment temperature increased, the effect of second phase on densification seemed to decrease. Based on predicted model data and preliminary experimental results, it seemed probable TiB_2 could be considered as non-densifying for temperatures of 1500°C and below.

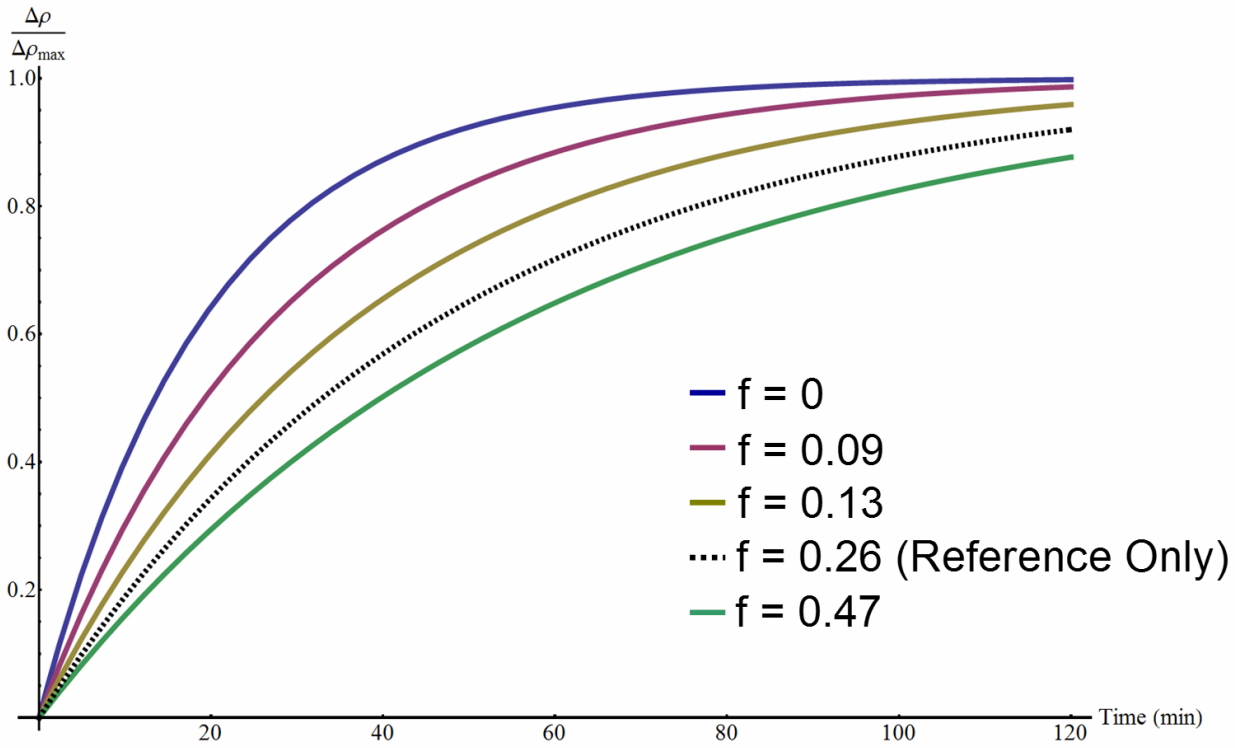

Figure 4.21 – Plots of densification factor versus heat treatment time based on the ceramic matrix composites sintering model developed by Bordia and Raj and data from Matsushita et al. for manually mixed Al_2O_3/TiB_2 heat treated at 1700°C.

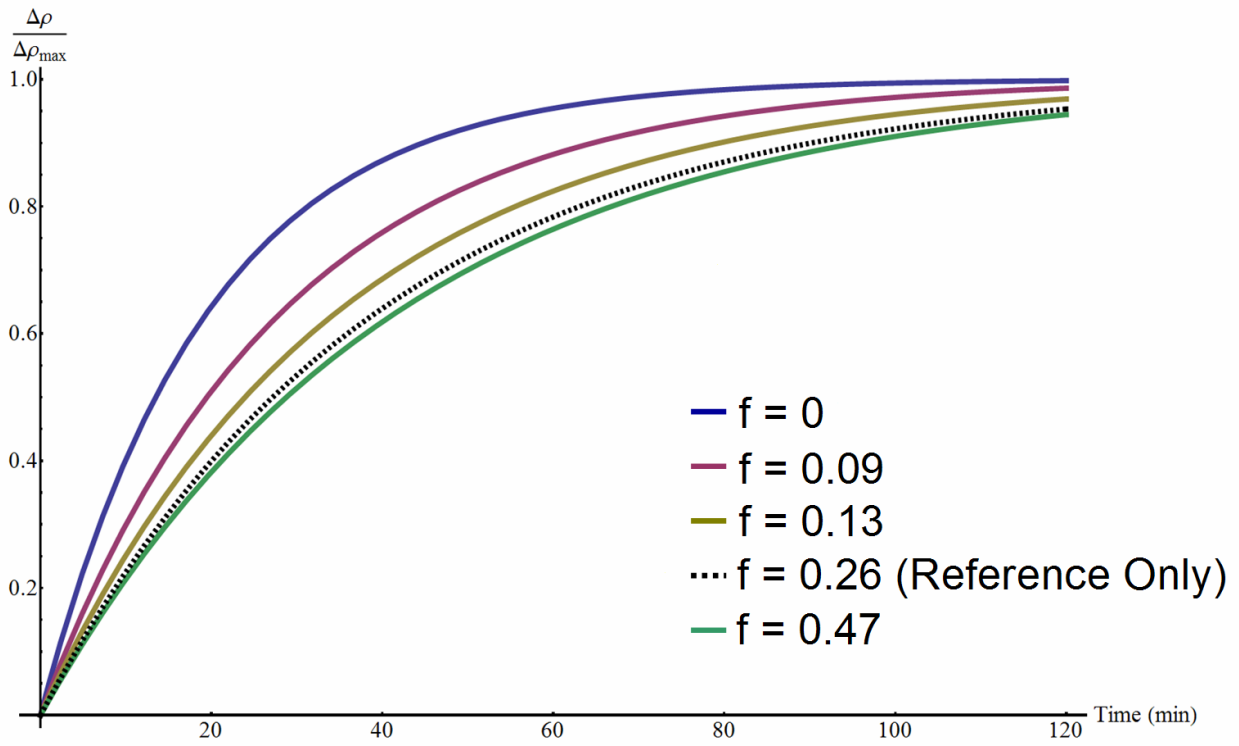

Figure 4.22 – Plots of densification versus heat treatment time based on the ceramic matrix composites sintering model developed by Bordia and Raj and data from Matsushita et al. for manually mixed Al_2O_3/TiB_2 heat treated at 1800°C.

4.3 Determination of the Activation Energy and Rate Controlling Diffusion Mechanism for Densification of SHS Produced Al_2O_3/TiB_2

This section discusses density, shrinkage, compound identification, structure, morphology, RCDM, and activation energy results from heat treatments of SHS produced Al_2O_3/TiB_2. The density and shrinkage section shows calculated densities, porosities, and shrinkage for SHS produced Al_2O_3/TiB_2 samples heat treated to determine RCDM and activation energy. The compound identification section describes compounds identified in heat treated SHS produced Al_2O_3/TiB_2. The structure and morphology section explains differences in microstructure for SHS produced Al_2O_3/TiB_2 heat treated at short versus long time, high versus low temperature, and inert versus oxidizing atmosphere.

4.3.1 Density and Shrinkage

SHS produced Al_2O_3/TiB_2 samples heat treated at 1500°C for 30, 60, and 90 minutes had an average density of 3.19 ± 0.06 g/cm^3, 3.30 ± 0.01 g/cm^3, 3.39 ± 0.01 g/cm^3 as shown in Table 4.12. As expected, the average density and impervious volume were highest for samples heat

treated for 90 minutes. Similarly, samples heat treated for 90 minutes had lowest pore volume, apparent porosity, and liquid absorption.

SHS produced Al_2O_3/TiB_2 samples heat treated for 30, 60, and 90 minutes at 1500°C increased in density by 29.7%, 34.1%, and 37.8% respectively. Increasing heat treatment time at temperature from 30 to 60 minutes or 60 to 90 minutes seemed to result in similar changes in density. However, increasing in heat treatment time from 60 to 90 minutes resulted in less volume shrinkage than increasing heat treatment time from 30 to 60 minutes. Slowing of shrinkage between 60 and 90 minutes may have indicated a shift in densification stage at heat treatment times longer than 60 minutes at 1500°C.

Table 4.12 – Average Archimedes Calculations for Determining Rate Controlling Diffusion Mechanism (1500°C)

Heat Treatment Time	Average Immersion Bulk Density (g/cm^3)	Average Pore Volume (cm^3)	Average Impervious Volume (cm^3)	Average Apparent Porosity (%)	Average Liquid Absorption (%)	Average Volume Shrinkage (%)
30 min	3.19 ± 0.06	0.23 ± 0.03	1.67 ± 0.01	12.66 ± 1.38	3.98 ± 0.51	34.54 ± 0.71
60 min	3.30 ± 0.01	0.22 ± 0.01	1.55 ± 0.01	12.51 ± 0.27	3.79 ± 0.09	37.66 ± 0.69
90 min	3.39 ± 0.01	0.13 ± 0.01	1.58 ± 0.01	7.71 ± 0.49	2.27 ± 0.15	39.19 ± 0.58

SHS produced Al_2O_3/TiB_2 samples heat treated at 1370°C, 1435°C, and 1500°C for 30 minutes had an average density of 2.86 ± 0.02 g/cm^3, 2.87 ± 0.02 g/cm^3, 3.19 ± 0.06 g/cm^3 as shown in Table 4.13. As expected, the average density and impervious volume were highest for samples heat treated at 1500°C. Similarly, samples heat treated at 1500°C had lowest pore volume, apparent porosity, and liquid absorption.

SHS produced Al_2O_3/TiB_2 samples heat treated at 1370°C, 1435°C, and 1500°C increased in density by 16.2%, 16.6%, and 29.7% respectively. Increasing heat treatment temperature from 1370°C to 1435°C resulted in only a small increase in density and shrinkage. However, increasing heat treatment temperature from 1435°C to 1500°C resulted in a much larger increase in density and shrinkage. Based on the larger changes in density and shrinkage observed from 1435°C to 1500°C, it seemed a barrier to densification may exist between 1435°C and 1500°C.

Table 4.13 – Average Archimedes Calculations for Determining Activation Energy (30 minutes)

Heat Treatment Temperature (°C)	Average Immersion Bulk Density (g/cm^3)	Average Pore Volume (cm^3)	Average Impervious Volume (cm^3)	Average Apparent Porosity (%)	Average Liquid Absorption (%)	Average Volume Shrinkage (%)
1370°C	2.86 ± 0.02	0.50 ± 0.01	1.55 ± 0.01	24.39 ± 0.47	8.53 ± 0.21	27.49 ± 1.31
1435°C	2.87 ± 0.02	0.41 ± 0.02	1.65 ± 0.02	19.94 ± 1.07	6.95 ± 0.40	27.23 ± 0.79
1500°C	3.19 ± 0.06	0.23 ± 0.03	1.67 ± 0.01	12.66 ± 1.38	3.98 ± 0.51	34.54 ± 0.71

4.3.2 Compound Identification

XRD traces showed many peaks for 2θ angles between 10° and 90° as shown in Figure 4.23. Analysis of the diffraction patterns revealed Al_2O_3, TiB_2, and $Al_{18}B_4O_{33}$ were present. However, peak intensities for $Al_{18}B_4O_{33}$ were different from the $Al_{18}B_4O_{33}$ peak intensities for the SHS product starting powder. Comparison of typical SHS produced Al_2O_3/TiB_2 sample heat treatment conditions with the samples exposed to an oxidizing environment during cooling showed noticeable differences in the peak intensities for $Al_{18}B_4O_{33}$.

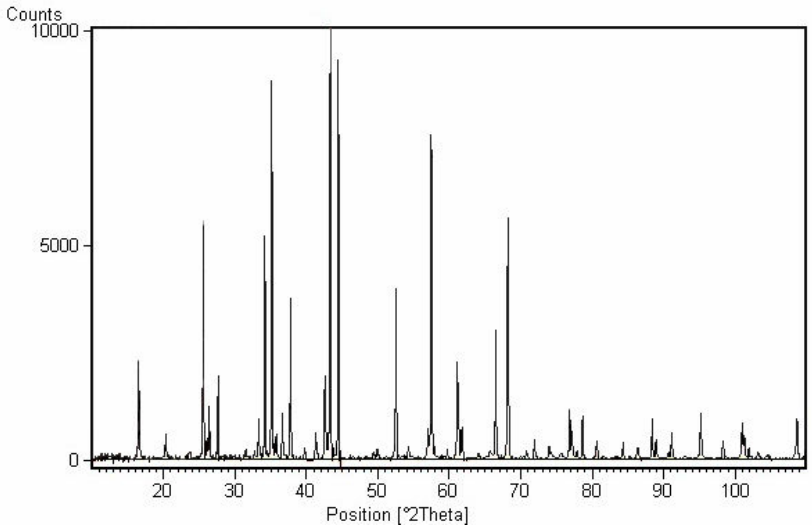

Figure 4.23 – X-ray diffraction pattern for SHS-produced Al_2O_3/TiB_2 heat treated at 1500°C for 30 minutes.

Based on SHS reaction product XRD analysis, the initial SHS reaction forms some $Al_{18}B_4O_{33}$ as shown in Figure 4.2. Analysis of a sample heat treated at 1500°C for 30 minutes showed the presence of Al_2O_3 and TiB_2 but also revealed considerably larger peak intensities for $Al_{18}B_4O_{33}$ than were seen for the starting powder as shown in Figure 4.24.

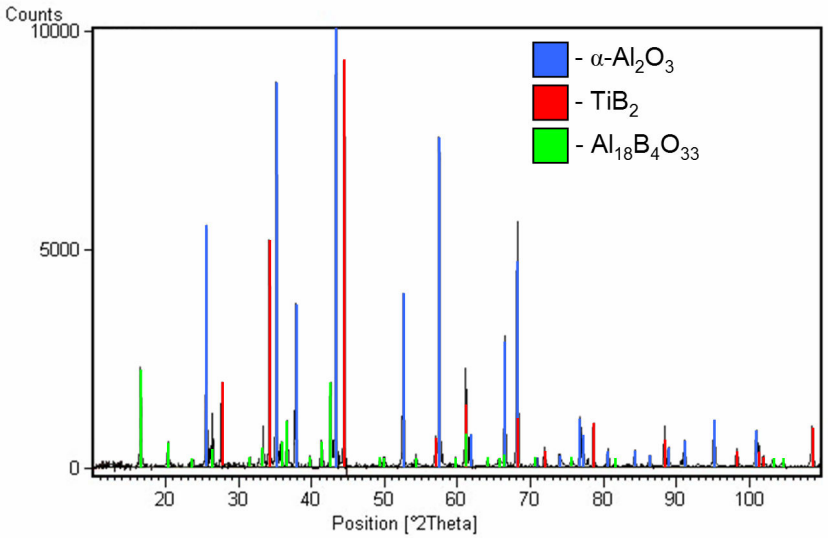

Figure 4.24 – Indexed diffraction pattern for SHS produced Al_2O_3/TiB_2 heat treated at 1500°C for 30 minutes.

The increased intensity of $Al_{18}B_4O_{33}$ may mean $Al_{18}B_4O_{33}$ formed by reaction of Al_2O_3 with TiB_2 at 1500°C according to Equation 4.1. The presence of Ti_2O_3 was not observed in the XRD pattern but may have been below the limits of detection or confused with pattern background noise during automated analysis. Another possibility for formation of $Al_{18}B_4O_{33}$ would be the presence of an oxidizing furnace environment during heat treatment or the existence of air trapped within the compact after pressing. However, since Ti_2O_3 was not observable within the XRD pattern produced, the method of formation for $Al_{18}B_4O_{33}$ was not able to be determined.

$$9\,Al_2O_3 + 4\,TiB_2 \rightarrow 9Al_2O + 2Ti_2O_3 + 4\,B_2O_3 \qquad (4.1)$$

4.3.3 Structure and Morphology

This section discusses microstructural differences between samples heat treated at low versus high temperature, short versus long time, crystallite formation, and normal versus low line pressure. Examination of the microstructure provided valuable insight into physical, structural, and chemical characteristics of SHS produced Al_2O_3/TiB_2 samples heat treated under varying conditions. Micrographs collected using SEM allowed for comparisons between different heat treatment temperatures and times. SEM and EDS provided better understanding of possible mechanisms for the formation of $Al_{18}B_4O_{33}$ seen in XRD analyses of heat treated SHS produced Al_2O_3/TiB_2. Comparisons of samples heat treated in inert atmosphere with samples exposed to

an oxidizing environment during furnace cooling revealed interesting characteristics of both samples.

4.3.3.1 Low Temperature versus High Temperature

Observation of samples heat treated at low temperature (1370°C) versus samples heat treated at higher temperature (1500°C) showed little difference in bulk microstructure at low magnification as shown in Figure 4.25. However, samples heat treated at 1500°C showed some distinct regions even at low magnification. The surface of the high temperature sample appeared to be highly porous with a dense region just below the surface and a moderately porous bulk region. Based on the general features shown in Figure 4.25, high magnification micrographs of each sample were taken.

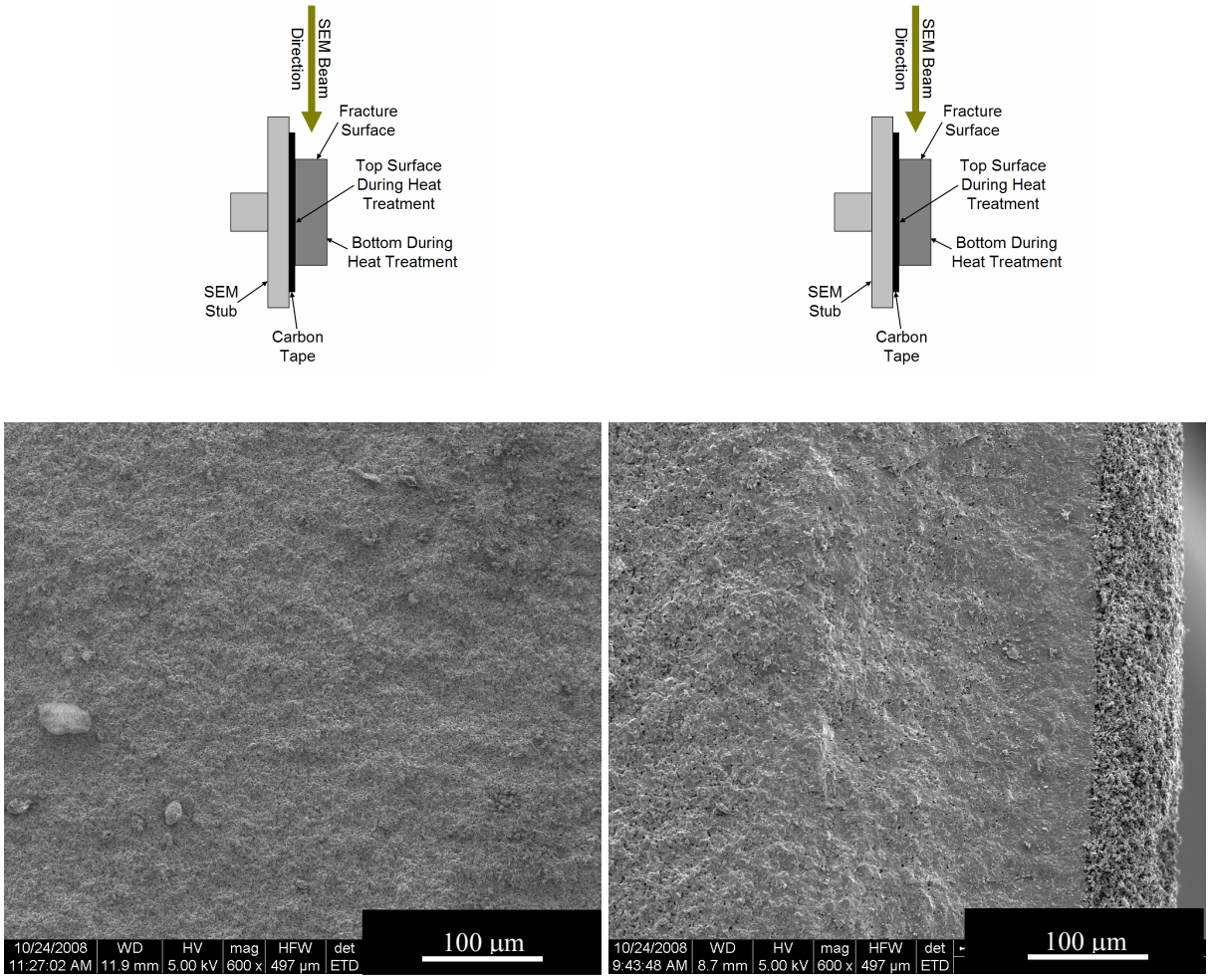

Figure 4.25 – Representative low magnification general microstructures of bulk region from samples of SHS produced Al_2O_3/TiB_2 heat treated at 1370°C (left) and 1500°C (right) for 30 minutes.

Observation of the low and high temperature microstructures at higher magnification showed interesting differences in general sample features as shown in Figure 4.26. The low temperature microstructure showed a greater degree of crystallinity while the high temperature microstructure showed more amorphous features. Pores in the lower temperature microstructure appeared to be smaller than in the higher temperature microstructure but the higher temperature microstructure seemed to have fewer pores. Also, the distribution of pores seemed to be more uniform at lower heat treatment temperature.

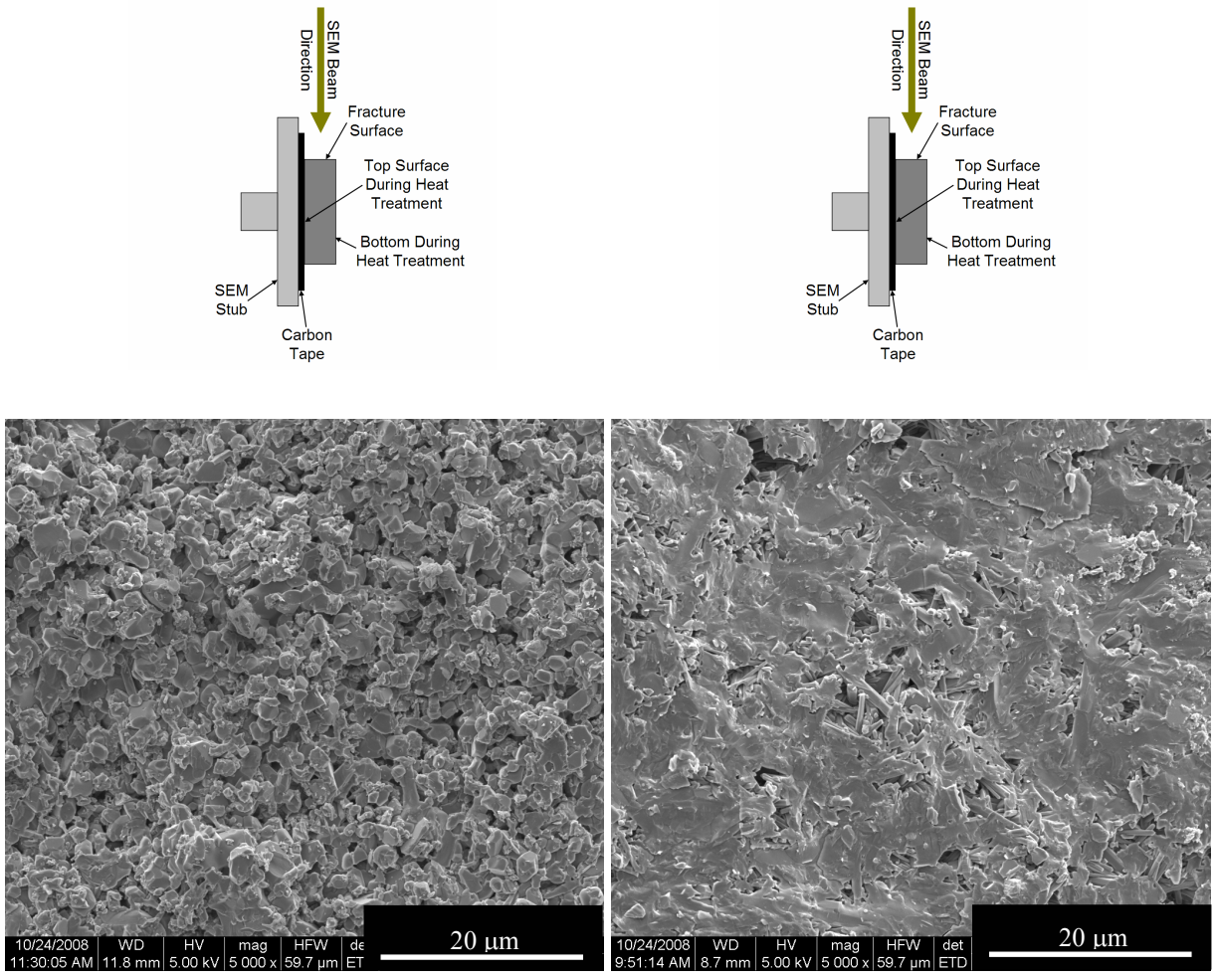

Figure 4.26 – Representative high magnification general microstructures from samples of SHS produced Al_2O_3/TiB_2 heat treated at 1370°C (left) and 1500°C (right) for 30 minutes.

The higher temperature may have activated a different diffusion mechanism within the samples, which resulted in the differences in sample microstructure. Increases in heat treatment temperature may have provided enough energy to create an amorphous structure within the constituent components. The presence of an amorphous compound after heat treatment may

indicate a liquid formed during heat treatment. Liquid formation at heat treatment temperature would have provided a rapid path for diffusion in the facilitation of liquid phase densification.

4.3.3.2 Short Time versus Long Time

SHS produced Al_2O_3/TiB_2 samples heat treated at shorter time versus samples heat treated at longer times appeared similar at low magnification with the exception of some apparent differences in surface regions as shown in Figure 4.27. At low magnification, both samples appeared to be porous but it was necessary to view the samples at higher magnifications to determine porosity and other unique microstructural features. The higher magnification microstructures did not appear to be very different from one another in appearance as shown in Figure 4.27. The biggest differences in the samples appeared to be the degree of porosity, smoothness of surface, and crystallite formations.

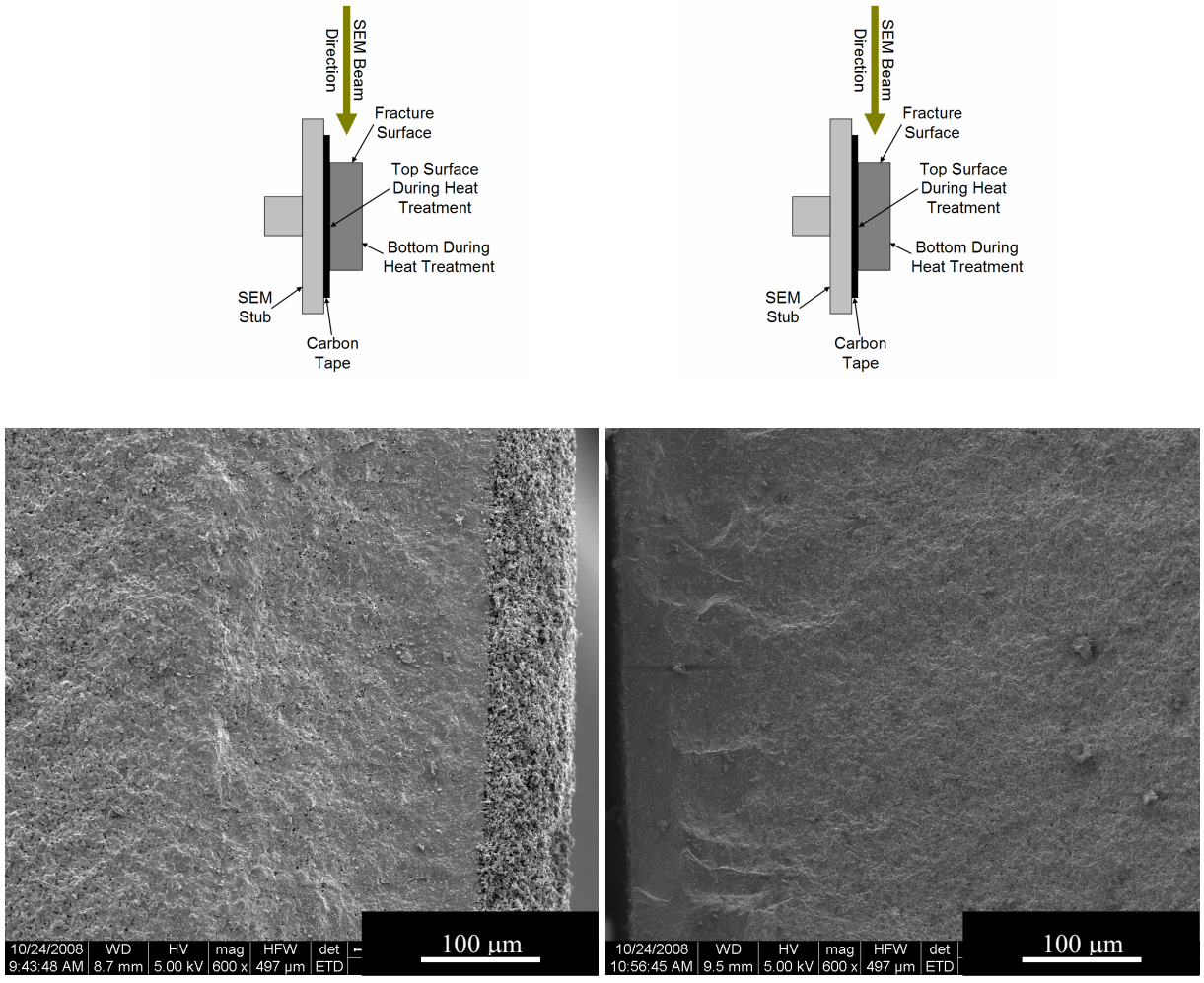

Figure 4.27 – Representative low magnification general microstructures from samples of SHS produced Al_2O_3/TiB_2 heat treated at 1500°C for 30 minutes (left) and 60 minutes (right).

SHS produced Al_2O_3/TiB_2 samples heat treated at 1500°C for 30 minutes seemed to have larger and less evenly distributed pores than samples heat treated for 60 minutes as shown in Figure 4.28. Sample heat treated for longer times were expected to have fewer and smaller pores than samples heat treated for shorter times at the same temperature. Samples heat treated for 30 minutes also appeared to have smoother fracture surfaces than samples heat treated for 60 minutes. It appeared samples heat treated for 60 minutes may be approaching the final stage of densification by liquid phase diffusion. The samples seemed to be exhibiting mostly closed porosity with a small degree of open porosity as shown in Table 4.11.

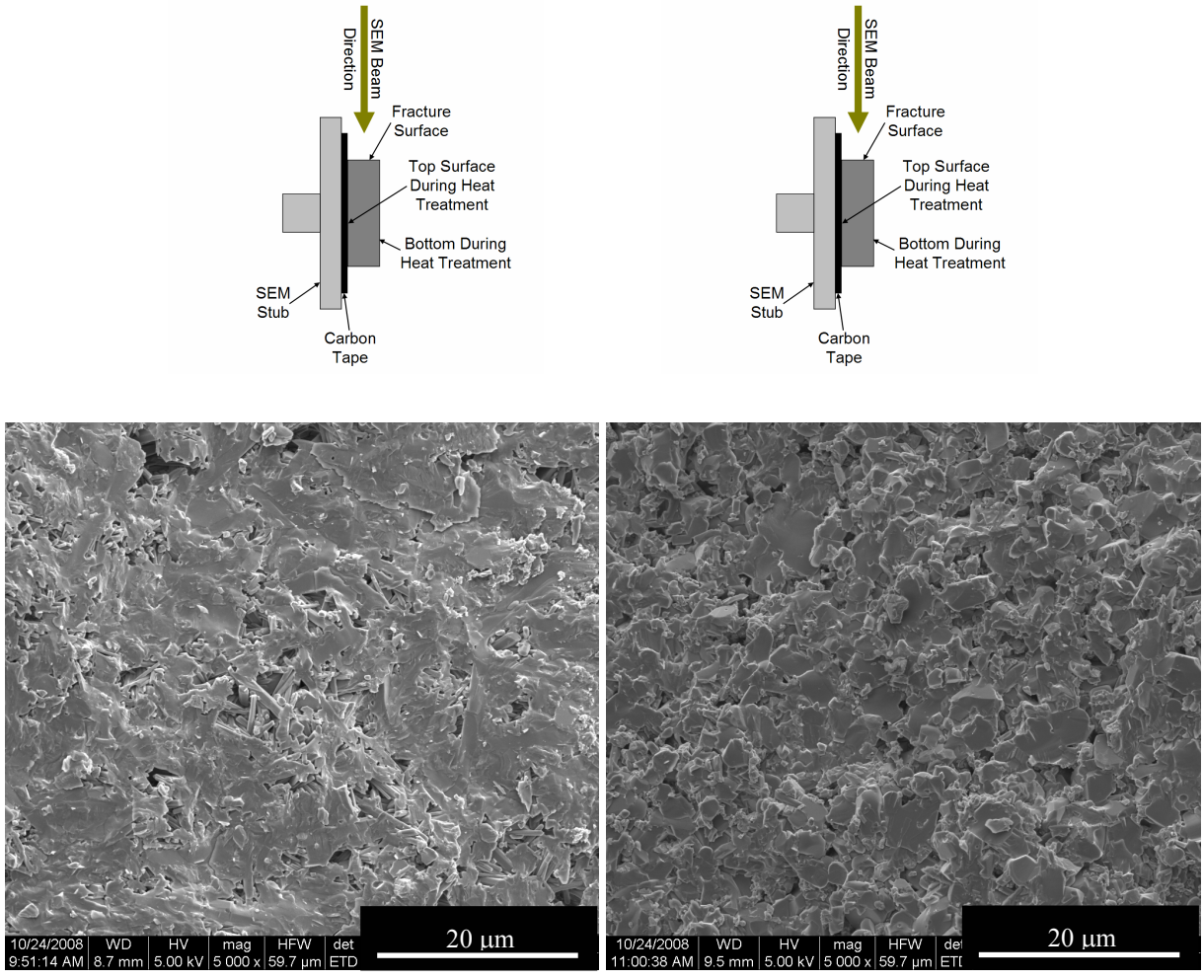

Figure 4.28 – Representative high magnification general microstructure from samples of SHS produced Al_2O_3/TiB_2 heat treated at 1500°C for 30 minutes (left) and 60 minutes (right).

4.3.3.3 Crystallite Formation

Within SHS produced Al_2O_3/TiB_2 samples heat treated at 1500°C for 30 minutes several areas were observed along fracture-surfaces. Areas closest to the sample's bottom exhibited the

most difference in structure as shown in Figure 4.29. The very bottom surface region displayed the most variety in microstructure with the very bottom taking on the structure of loosely fused powder with acicular crystallites bridging the sample and the powder. The next region appeared to be mostly amorphous followed by the bulk sample microstructure.

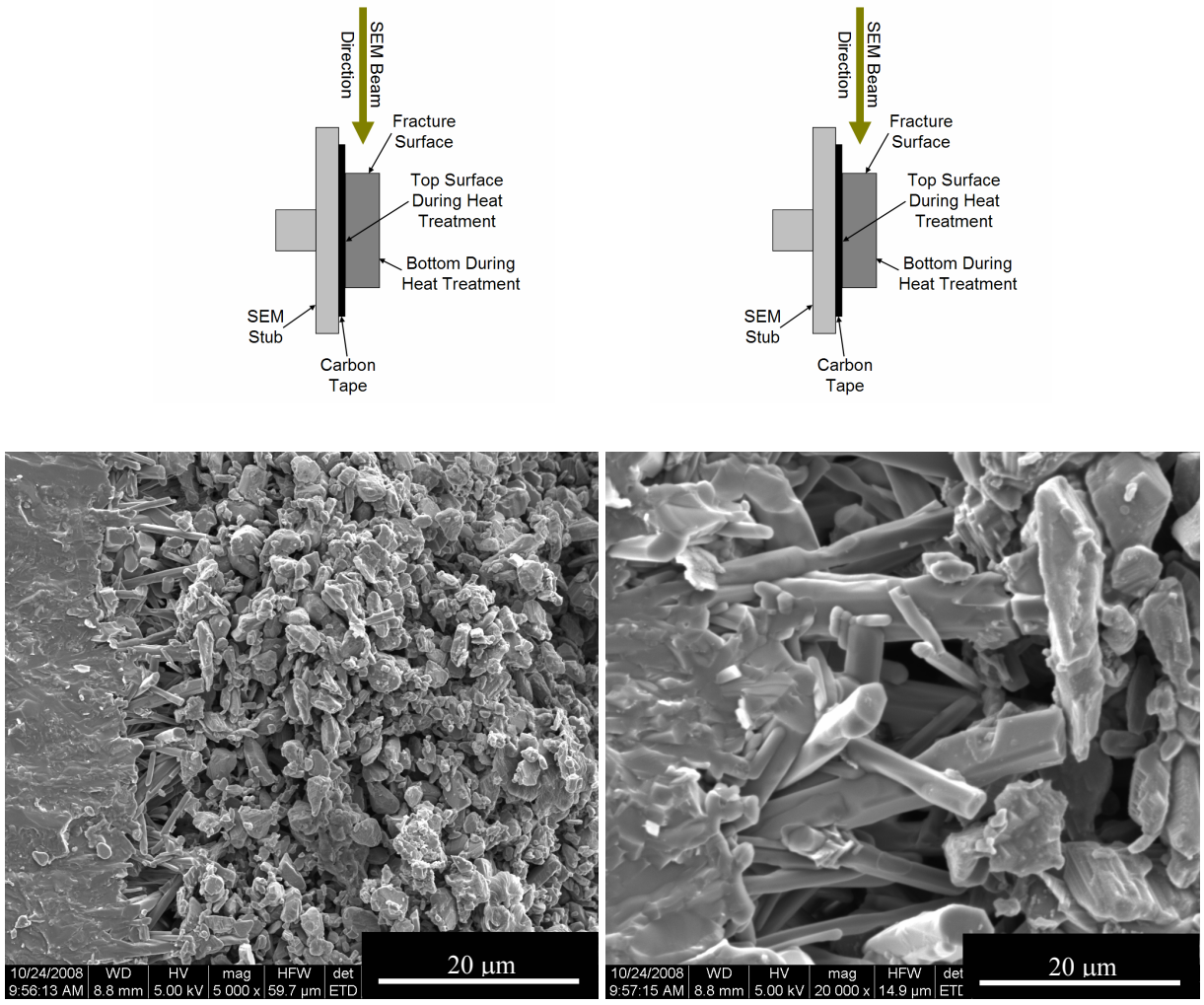

Figure 4.29 – General microstructure at the transition between bottom surface and subsurface regions (left) and the crystal formations at the transition (right) from a sample of SHS produced Al_2O_3/TiB_2 heat treated at 1500°C for 30 minutes.

EDS was used to analyze the chemistry of the samples regions as shown in Figure 4.30. Studying the chemistry from EDS provided insight into possible compounds present within each region. The EDS showed large variations in the amounts of aluminum (Al), oxygen (O), and titanium (Ti) over the four regions observed as shown in Table 4.14. Limitations of the EDS

detector were unable to provide information on the presence and relative percentages of boron (B) in each region.

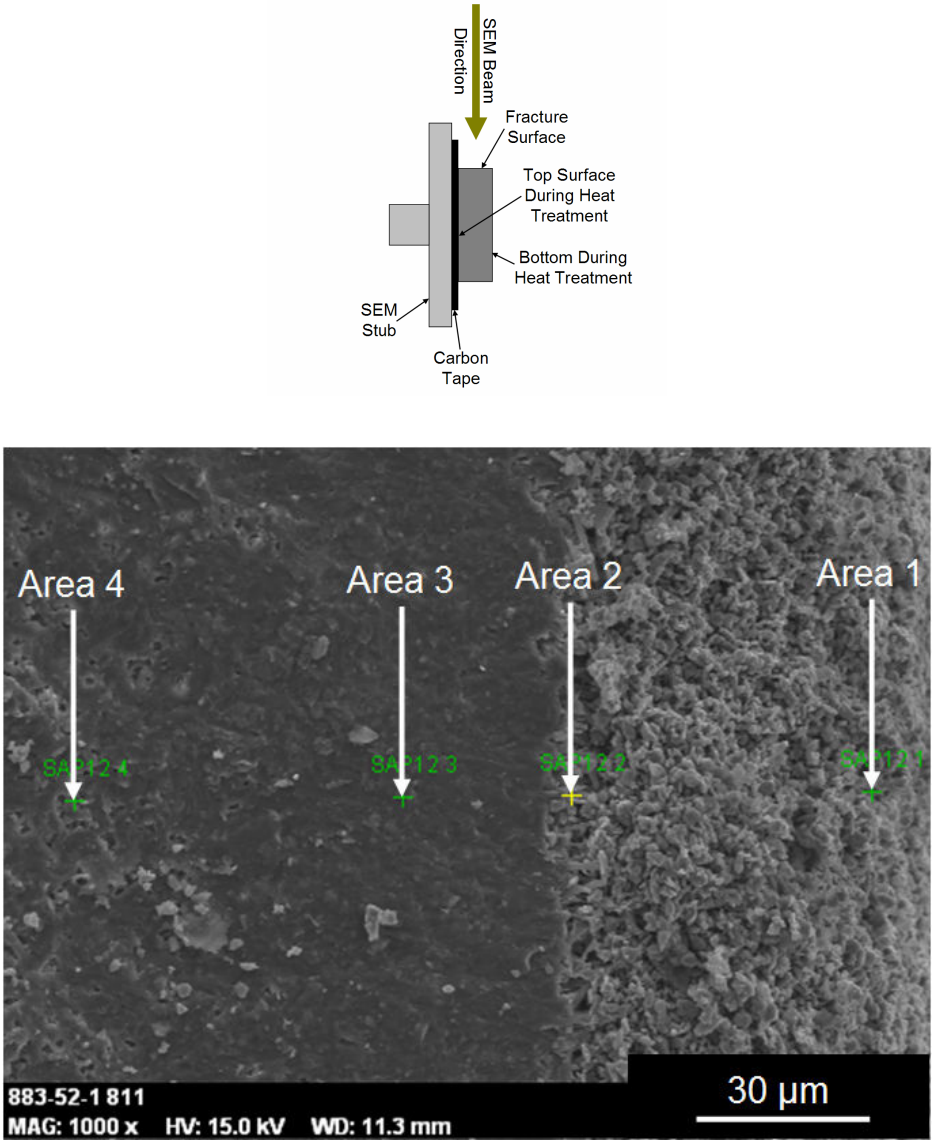

Figure 4.30 – SEM micrograph of the regions from sample heat treated at 1500°C for 30 minutes and analyzed using EDS.

The chemistry seemed to indicate area 1 was primarily composed of Ti compounds and based on SEM images of area 1 (shown in Figure 4.30) it seemed area 1 was powder (TiB_2) from the sample holder tray fused to the sample's bottom. Area 2 contained mostly Al and O, which suggested the region was probably either Al_2O_3 or $Al_{18}B_4O_{33}$. SEM of area 2 showed acicular crystallites and the crystallite structure suggested the crystallites were $Al_{18}B_4O_{33}$.

Area 3 showed a similar chemistry to area 2, which suggests the presence of Al_2O_3 or $Al_{18}B_4O_{33}$. The SEM of area 3 appeared mostly amorphous, which suggested area 3 may contain $Al_{18}B_4O_{33}$ since $Al_{18}B_4O_{33\ (s)} + B_2O_{3\ (l)}$ formation begins above 1000°C. Area 4 showed appreciable amounts of Al, O, and Ti suggesting the region was primarily Al_2O_3 and TiB_2; however, $Al_{18}B_4O_{33}$ may have also been present in area 4. The trace amounts of calcium (Ca), iron (Fe), magnesium (Mg), phosphorous (P), and silicon (Si) were probably due to impurities from processing of the powders used for the SHS reaction.

Table 4.14 – Chemical Analysis Obtained from EDS of a Sample Heat Treated at 1500°C for 30 Minutes

Spectrum	Al	Ca	Fe	Mg	O	P	Si	Ti
Area 1	1.34	-	-	-	28.36	-	0.94	69.36
Area 2	28.27	-	-	-	69.56	-	0.86	1.31
Area 3	25.37	0.66	-	1.17	68.18	-	2.09	2.53
Area 4	8.11	-	1.28	-	45.85	1.23	0.12	43.41
Mean	15.78	0.16	0.32	0.29	52.99	0.31	1.00	29.15
Sigma	13.11	0.33	0.64	0.58	19.69	0.61	0.81	33.18
Sigma Mean	6.55	0.16	0.32	0.29	9.85	0.31	0.41	16.59

Based on the XRD, SEM, and EDS data it seemed plausible $Al_{18}B_4O_{33}$ formed by reaction of Al_2O_3 and TiB_2 according to Equation 4.1. After heat treatment, the TiB_2 powder directly underneath of the samples was observed to be lighter in color than all the other powder as shown in Figure 4.31. Also, after heat treatment, the areas of the tray directly underneath of the samples had changed color as shown in Figure 4.31. The color change along Al_2O_3/TiB_2 interfaces within the experimental setup suggested reaction between Al_2O_3 and TiB_2 in support of the reaction theory proposed by Equation 4.1.

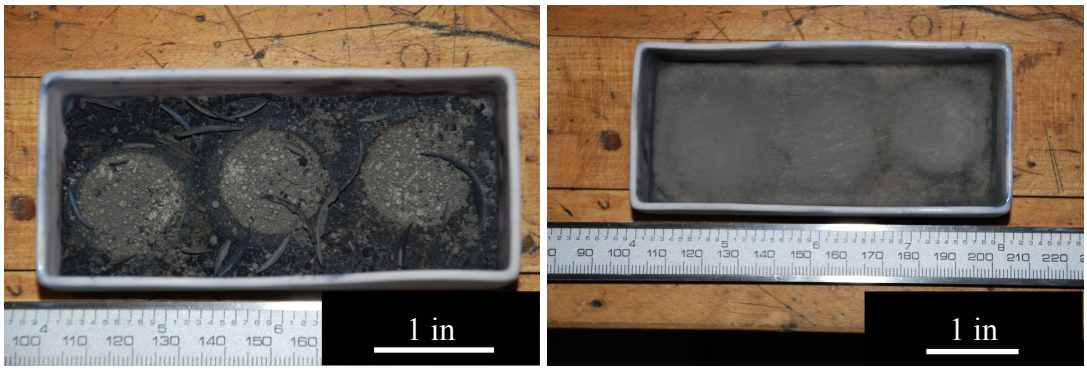

Figure 4.31 – Lighter region in TiB_2 powder (left) and darker region on the surface of Al_2O_3 crucible (right) after heat treatment.

The crystallites found in area 2 were also found in certain parts of area 4 as shown in Figure 4.32. The crystallites were believed to be $Al_{18}B_4O_{33}$ based on the EDS results shown above and crystallite morphology. The crystallites may have also formed by reaction of Al_2O_3 and TiB_2 according to Equation 4.1.

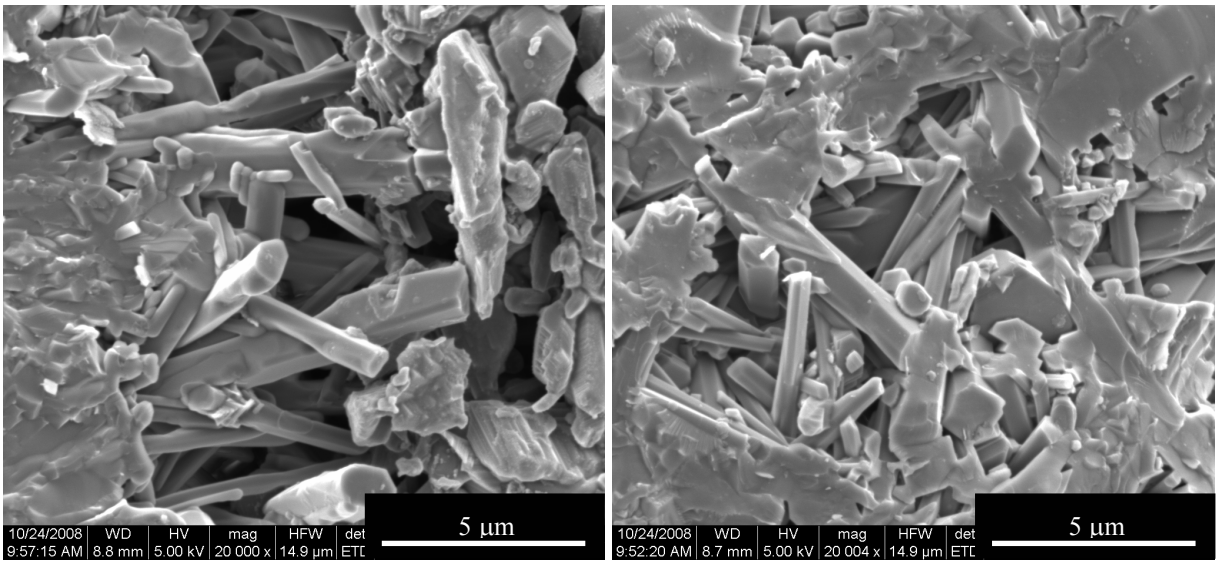

Figure 4.32 – General microstructure at the bottom surface to subsurface transition region (left) and the bulk region (right) in a sample of SHS produced Al_2O_3/TiB_2.

4.3.3.4 Normal Line Pressure versus Low Line Pressure

The bottom surface of an oxidized SHS produced Al_2O_3/TiB_2 sample was compared with the bottom surface of a representative sample heat treated at 1500°C as shown in Figure 4.33. The representative SHS produced Al_2O_3/TiB_2 sample heat treated at 1500°C showed several acicular crystallites had formed in various directions with smaller particles attached at various places along the sample surface. The crystallites observed on the sample's bottom surface seemed to support the idea of formation of $Al_{18}B_4O_{33}$ along Al_2O_3 and TiB_2 interfaces.

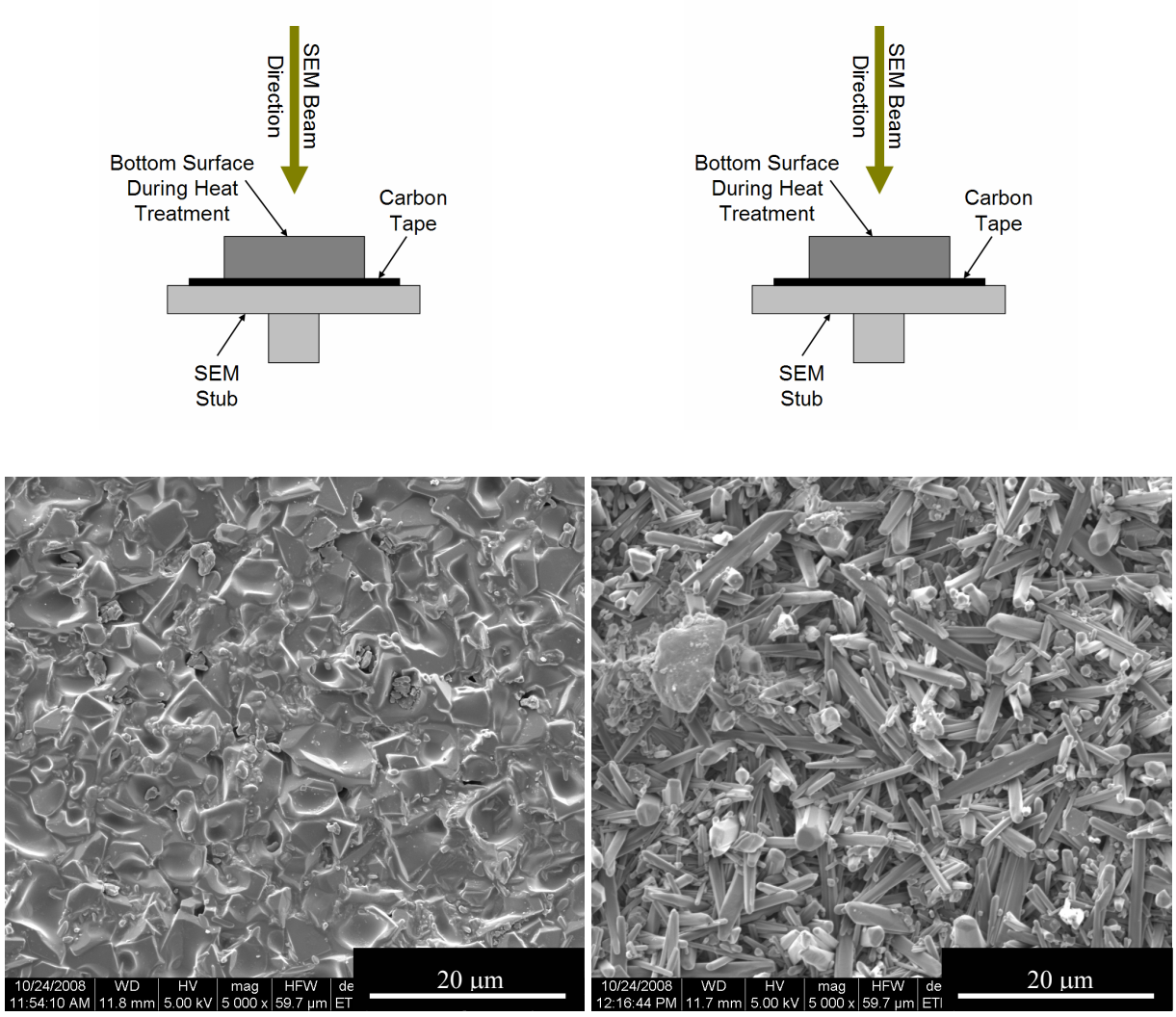

Figure 4.33 – Micrographs of the bottom surface of a sample of SHS produced Al_2O_3/TiB_2 exposed to air during cooling (left) and a representative sample (right) of SHS produced Al_2O_3/TiB_2 after being heat treated at 1500°C.

4.3.4 Rate Controlling Diffusion Mechanism and Activation Energy Calculations

The calculated n-values for SHS produced Al_2O_3/TiB_2 varied from 0.34 to 0.45 and averaged 0.40 ± 0.06. The activation energy was calculated to be 333.6 ± 93.2 kJ. Based on the calculated n-value, it seemed the RCDM for SHS produced Al_2O_3/TiB_2 was volume diffusion. A plot of the densification factor versus the heat treatment time yielded the following fit equation $\eta = 3.0781t^{0.40}$ with an R^2 value of 0.9979 as shown in Figure 4.34. However, the calculations for determining theoretical sample volume assumed the presence of Al_2O_3 and TiB_2 but not $Al_{18}B_4O_{33}$. Based on characterization results for heat treatment of SHS produced Al_2O_3/TiB_2, it seemed unreasonable to ignore the presence of $Al_{18}B_4O_{33}$.

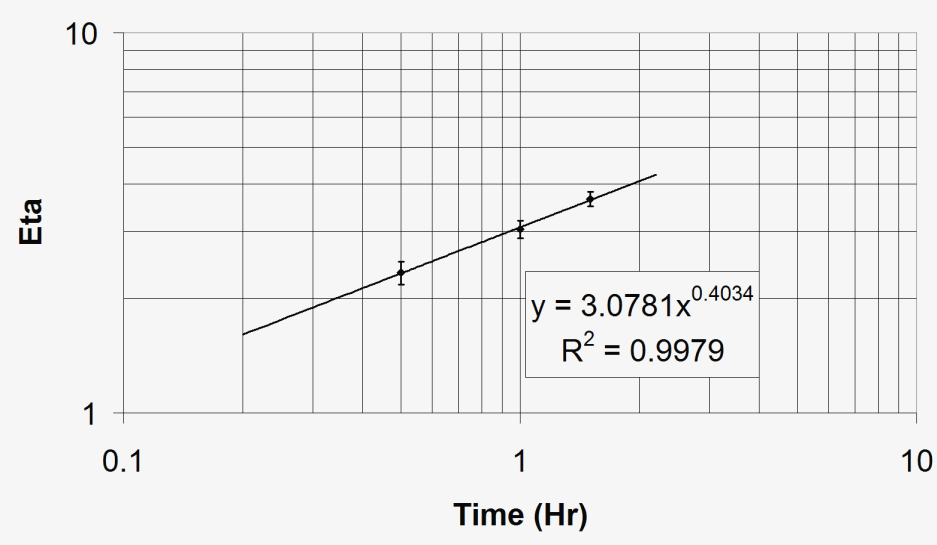

Figure 4.34 - Densification factor versus heat treatment time for determining RCDM of SHS produced Al_2O_3/TiB_2 based on the presence of Al_2O_3 and TiB_2 only.

When the presence of $Al_{18}B_4O_{33}$ was accounted for in determining theoretical sample volume, the calculated n-values varied from 0.45 to 0.61 and averaged 0.56 ± 0.09. The corresponding activation energy was calculated to be 296.4 ± 86.7 kJ. Based on the calculated n-value, the RCDM was liquid phase diffusion. Volume diffusion may have also been active during the densification process. Observed microstructural features seemed to support both liquid phase and volume diffusion mechanisms were active during the densification of SHS produced Al_2O_3/TiB_2. A plot of the densification factor versus heat treatment time yielded the following fit equation $\eta = 4.7875t^{0.55}$ with an R^2 value of 0.9989 as shown in Figure 4.35. The large standard deviations for both activation energy calculations are probably due to the small number of data points available for the calculations. Further experimentation with more data points may reduce the standard deviation and provide more accurate calculation of the activation energy.

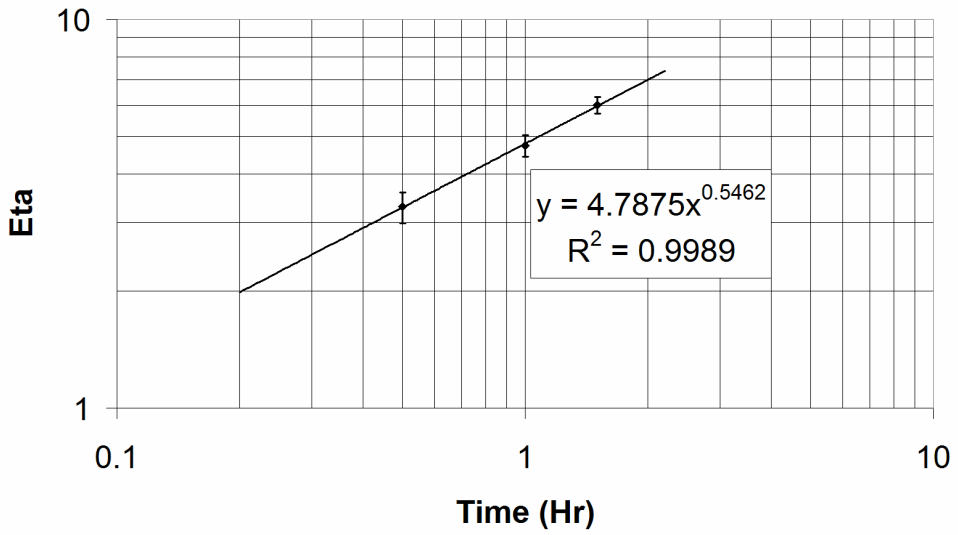

Figure 4.35 – Densification factor versus heat treatment time for determining RCDM of SHS produced Al_2O_3/TiB_2 based on Al_2O_3, TiB_2, and $Al_{18}B_4O_{33}$.

4.4 Theoretical and Experimental Comparison

This section discusses the comparison of preliminary predictions with experimental results for STCs and sintering of CMCs models. The STCs section explains differences and similarities found during comparison of STCs for Al_2O_3 and SHS produced Al_2O_3/TiB_2. The sintering of CMCs section describes differences in model predictions and experimental data for SHS produced Al_2O_3/TiB_2.

4.4.1 Time Constant for Sintering Al_2O_3/TiB_2

The STC for SHS produced Al_2O_3/TiB_2 heat treated at 1500°C was calculated to be 217.4 minutes as shown in Figure 4.36. The large STC value suggested a long STC dominated for heat treatment times greater than 30 minutes. The data seemed to suggest the assumption that TiB_2 in the composite was non-densifying may have been accurate. It was not possible to draw any definite conclusion about the densification of TiB_2 in the composite without performing further experimentation. The large STC for SHS produced Al_2O_3/TiB_2 suggested an increase in heat treatment temperature may result in higher densities and shorter required heat treatment times. The STC for SHS produced Al_2O_3/TiB_2 may have also been an indication samples were close to full density.

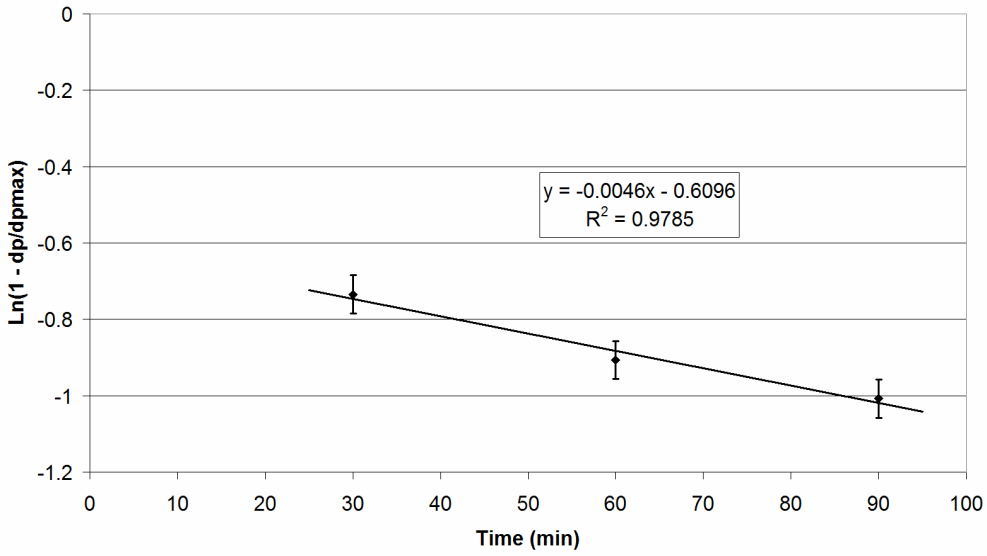

Figure 4.36 – Plot used to determine the STC for SHS produced Al_2O_3/TiB_2 heat treated at 1500°C.

4.4.2 Validation of Bordia and Raj's Composite Sintering Model

Based on calculation of densification factor versus heat treatment time, the Bordia and Raj model for densification of a composite seemed to not fit the experimental data above 90 minutes as shown in Figure 4.37. At a heat treatment time of 90 minutes, samples should have had an average density of 3.60 g/cm^3 but experimental data showed an average density of 3.39 g/cm^3 (See Table 4.12). Differences in theory and experimental results were probably due to the $Al_{18}B_4O_{33}$ not being accounted for in the theory rather than inaccuracies in the model itself.

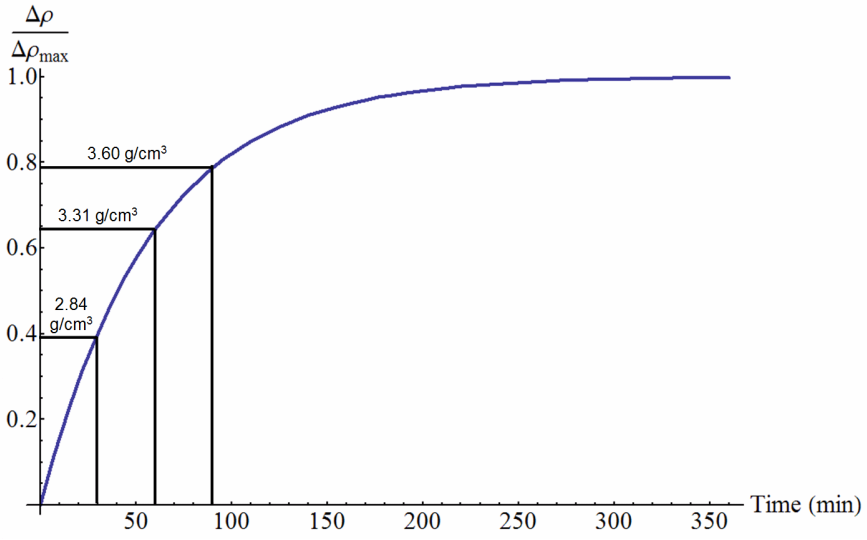

Figure 4.37 – Predictive sintering curve for SHS produced Al_2O_3/TiB_2 heat treated at 1500°C.

5. Conclusions

This chapter presents conclusions drawn from results discussed in Chapter 4.

5.1 Preliminary Experiments

As milled SHS produced Al_2O_3/TiB_2 powder contained $Al_{18}B_4O_{33}$ based on XRD analysis.

Particle size distributions showed a particle size range of 0.1 - 300 μm.

The composite rule of mixtures calculated Al_2O_3/TiB_2 refractive index showed drastically different results than indices for Al_2O_3 and TiB_2.

SHS produced Al_2O_3/TiB_2 powder particles were approximately spherical or elliptical with rough surfaces.

Optimal pressing settings for SHS produced Al_2O_3/TiB_2 were determined to be single action pressing to 20,000 psi with as milled powder.

Springback at peak pressure was responsible for warping of samples after heat treatment.

Heat treatment of carbothermic TiB_2 at 1800°C for 30 minutes showed negligible density changes from the green state.

Heat treatment of carbothermic TiB_2 at 2100°C for 60 minutes showed evidence of densification.

During heat treatment of SHS produced Al_2O_3/TiB_2, temperature correction was impacted by helium line pressure.

Very low helium line pressure during heat treatment of SHS produced Al_2O_3/TiB_2 resulted in sample discoloration, formation of $Al_{18}B_4O_{33}$, and amorphous structure along sample surfaces.

5.2 Predicting the Densification Behavior of SHS Produced Al_2O_3/TiB_2

For densification of submicron Al_2O_3, long STCs should dominate for heat treatments of 30 minutes or longer at temperatures above 1300°C.

Densification stage progression for heat treatment of Al_2O_3 should be faster at higher temperatures.

TiB_2 reinforcement in manually mixed Al_2O_3/TiB_2 restricts densification during heat treatments at 1700°C and 1800°C as compared with Al_2O_3.

Results from the sintering of CMCs model for heat treatment of manually mixed Al_2O_3/TiB_2 agree with preliminary experiments for heat treatment of carbothermic TiB_2 in suggesting that TiB_2 may be considered non-densifying at temperatures below 1800°C.

5.3 Rate Controlling Diffusion Mechanism and Activation Energy

There is a possible diffusion barrier below 1500°C for 30 minute heat treatments of SHS produced Al_2O_3/TiB_2.

There is a possible change in densification stage at 60 minutes for heat treatments of SHS produced Al_2O_3/TiB_2 at 1500°C.

Heat treatment of SHS Produced Al_2O_3/TiB_2 at 1500°C resulted in a possible reaction between Al_2O_3 and TiB_2 leading to the formation of $Al_{18}B_4O_{33}$ and B_2O_3 liquid.

The RCDM for heat treatment of SHS produced Al_2O_3/TiB_2 was liquid phase diffusion with volume diffusion also likely being active.

Further Experiments are required to accurately determine activation energy for densification of SHS produced Al_2O_3/TiB_2

5.4 Theoretical and Experimental Comparison

A long STC dominated for SHS produced Al_2O_3/TiB_2 heat treated at 1500°C for 30 minutes or longer as predicted by using data for submicron Al_2O_3.

The sintering of CMCs model for SHS produced Al_2O_3/TiB_2 heat treated at 1500°C showed inaccuracies above 60 minutes.

Inaccuracies in the predicted density for SHS produced Al_2O_3/TiB_2 heat treated at 1500°C were likely due to difficulties with incorporation of a reaction to create $Al_{18}B_4O_{33}$ into the model.

6. Future Work

$Al_{18}B_4O_{33}$ was formed during SHS reaction of Al, B_2O_3, and TiO_2, as well as, during heat treatment of SHS produced Al_2O_3/TiB_2. In addition, $Al_{18}B_4O_{33\ (s)} + B_2O_{3\ (l)}$ formed above 1000°C is believed to be the source of liquid formed during heat treatment of SHS produced Al_2O_3/TiB_2 and liquid phase diffusion was found to be the RCDM. Therefore, research into methods for effectively controlling the amount of $Al_{18}B_4O_{33}$ formed during the SHS reaction and subsequent heat treatments would be very beneficial.

A thin amorphous layer was observed on exterior surfaces of SHS produced Al_2O_3/TiB_2 heat treated under oxidizing conditions and it seemed plausible formation of $Al_{18}B_4O_{33}$ + liquid above 1000°C was responsible for the amorphous layer. Low open porosity and liquid absorption for SHS produced Al_2O_3/TiB_2 exposed to oxidizing conditions suggested the amorphous layer may prevent further exposure of the material's bulk to oxygen. Based on the findings for SHS produced Al_2O_3/TiB_2 exposed to oxidizing conditions, oxidation studies should be pursued to determine if the amorphous compound provides an oxygen passivating layer.

Acicular crystallites of $Al_{18}B_4O_{33}$ formed in the microstructure of SHS produced Al_2O_3/TiB_2 heat treated at 1500°C. The crystallites seemed to be most prevalent along interfaces of Al_2O_3 and TiB_2. Further study should be done to determine the role of $Al_{18}B_4O_{33}$ crystallites in diffusion processes occurring during densification of SHS produced Al_2O_3/TiB_2 and whether densification is diffusion limited, reaction limited, or mixed mode.

Diffusion through a liquid was found to be the RCDM with volume diffusion likely aiding the densification of SHS produced Al_2O_3/TiB_2. Also, a possible shift in densification stage was identified at 60 minutes for heat treatment of SHS produced Al_2O_3/TiB_2 at 1500°C. The densification behavior of SHS produced Al_2O_3/TiB_2 suggests Rate Controlled Sintering (RCS) may be a good processing alternative. RCS studies with SHS produced Al_2O_3/TiB_2 may provide greater control over the densification of SHS produced Al_2O_3/TiB_2.

Appendices

A. Full and Fractional Factorial Arrays

Three Factors at Two Levels

Table A.1 – Full Factorial Array for Three Factors at Two Levels

Trial	A	B	C (A x B)
1	1	1	1
2	1	2	1
3	1	1	2
4	1	2	2
5	2	1	1
6	2	2	1
7	2	1	2
8	2	2	2

Table A.2 – Fractional Factorial Array for Three Factors at Two Levels

Trial	A	B	C (A x B)
1	1	1	1
2	1	2	2
3	2	1	2
4	2	2	1

Seven Factors at Two Levels

Table A.3 – Fractional Factorial Array for Seven Factors at Two Levels

Trial	A	B	C (A x B)	D	E (A x C)	F (B x C)	G
1	1	1	1	1	1	1	1
2	1	1	1	2	2	2	2
3	1	2	2	1	1	2	2
4	1	2	2	2	2	1	1
5	2	1	2	1	2	1	2
6	2	1	2	2	1	2	1
7	2	2	1	1	2	2	1
8	2	2	1	2	1	1	2

B. Example ANOVA Calculations

B.1 Calculations to Create an ANOVA Table

As an example, consider data shown in Table B.1 as results from a designed experiment. Based on the data in Table B.1, SS_T, SS_A, SS_B, SS_{AxB}, and SS_e may be calculated as shown by Equations B.1 – B.5.

Table B.1 – Example Experimental Data from a Designed Experiment

	A1	A2
B1	5, 7	2, 3
B2	6, 7	8, 9

$$SS_T = \left(5^2 + 7^2 + 2^2 + 3^2 + 6^2 + 7^2 + 8^2 + 9^2\right) - \frac{(47)^2}{8} = 40.875 \tag{B.1}$$

$$SS_A = \frac{(5+7+6+7)^2}{4} + \frac{(2+3+8+9)^2}{4} - \frac{47^2}{8} = 1.125 \tag{B.2}$$

$$SS_B = \frac{(5+7+2+3)^2}{4} + \frac{(6+7+8+9)^2}{4} - \frac{47^2}{8} = 21.125 \tag{B.3}$$

$$SS_{AxB} = \frac{(5+7)^2}{2} + \frac{(2+3)^2}{2} + \frac{(6+7)^2}{2} + \frac{(8+9)^2}{2} - \frac{47^2}{8} - 1.125 - 21.125 = 15.125 \tag{B.4}$$

$$SS_e = 40.875 - 1.125 - 21.125 - 15.125 = 3.500 \tag{B.5}$$

Degrees Of Freedom (DOF) for A, B, AxB, error, and total DOF for the data in Table B.1 may be calculated as shown in Equations B.6 – B.10.

$$\nu_T = 8 - 1 = 7 \tag{B.6}$$

$$\nu_A = 2 - 1 = 1 \tag{B.7}$$

$$\nu_A = 2 - 1 = 1 \tag{B.8}$$

$$\nu_{A\times B} = 1 \cdot 1 = 1 \tag{B.9}$$

$$\nu_e = 7 - 1 - 1 - 1 = 4 \tag{B.10}$$

Variance for A, B, AxB, and error for the data in Table B.1 may be calculated as shown in Equations B.11 – B.14.

$$V_A = \frac{1.125}{1} = 1.125 \tag{B.11}$$

$$V_B = \frac{21.125}{1} = 21.125 \tag{B.12}$$

$$V_{A\times B} = \frac{15.125}{1} = 15.125 \tag{B.13}$$

$$V_e = \frac{3.500}{4} = 0.875 \tag{B.14}$$

F-values for A, B, and AxB for the data in Table B.1 may be calculated as shown in Equations B.15 – B.17.

$$F_A = \frac{1.125}{0.875} = 1.286 \tag{B.15}$$

$$F_B = \frac{21.125}{0.875} = 24.143 \tag{B.16}$$

$$F_{AxB} = \frac{15.125}{0.875} = 17.286 \tag{B.17}$$

SS' for A, B, and AxB for the data in Table B.1 may be calculated as shown in Equations B.18 – B.20.

$$SS'_A = 1.125 - (0.875)\cdot(1) = 0.25 \tag{B.18}$$

$$SS'_B = 21.125 - (0.875)\cdot(1) = 20.25 \tag{B.19}$$

$$SS'_{A\times B} = 15.125 - (0.875)\cdot(1) = 14.25 \tag{B.20}$$

Percentage of Influence for A, B, and AxB for the data in Table B.1 may be calculated as shown in Equations B.21 – B.23.

$$P_A = \frac{0.25}{40.875}\times 100 = 0.6\% \tag{B.21}$$

$$P_B = \frac{20.25}{40.875}\times 100 = 49.5\% \tag{B.22}$$

$$P_{A\times B} = \frac{14.25}{40.875} \times 100 = 34.9\% \tag{B.23}$$

Results of calculations shown in B.1 – B.23 may be summarized in an ANOVA table as shown in Table B.2.

Table B.2 – Example ANOVA Table from a Designed Experiment

Source	SS	DOF	V	$F_{calc.}$	SS'	P
A	1.125	1	1.125	1.286	0.25	0.6%
B	21.125	1	21.125	24.143	20.25	49.5%
A x B	15.125	1	15.125	17.286	14.25	34.9%
Error	3.500	4	0.875	-	-	-
Total	40.875	7	-	-	-	85%

B.2 Error Pooling

Based on data from Table B.2, error pooling may be employed. For the first example error will be pooled down. Since factor B has the largest SS value, factor A and the interaction AxB will be pooled into error and a new ANOVA table is generated as shown in Table B.3.

Table B.3 – Example ANOVA Table for Error Pooled Down

Source	SS	DOF	V	$F_{calc.}$	SS'	P
A	e_p	e_p	e_p	e_p	e_p	e_p
B	21.125	1	21.125	2.600	13.000	34.8%
A x B	e_p	e_p	e_p	e_p	e_p	e_p
e_p	16.250	2	8.125	-	-	-
Total	37.375	3	-	-	-	34.8%

For the second example, error will be pooled up. Since factor A has the smallest SS value, factor A will be pooled into error and a new ANOVA table is generated as shown in Table B.4.

Table B.4 – Example ANOVA Table for Error Pooled Up

Source	SS	DOF	V	$F_{calc.}$	SS'	P
A	e_p	e_p	e_p	e_p	e_p	e_p
B	21.125	1	21.125	18.778	20.000	53.5%
A x B	15.125	1	15.125	13.444	14.000	37.5%
e_p	1.125	1	1.125	-	-	-
Total	37.375	3	-	-	-	91.0%

B.3 Prediction of Optimum Settings

An example of predicted response (PR) for factor A at level 1 and factor B at level 1 is shown in Equation B.24. A table summarizing PR for all combinations of A and B is shown in Table B.5.

$$PR = 6.25 + 4.25 + 6 - (2)(5.875) = 4.750 \tag{B.24}$$

Table B.5 – Example Prediction of Optimum Settings

Setting	Predicted Response
A2 B2	9.750
A1 B2	8.500
A1 B1	4.750
A2 B1	0.500

C. Electrical Schematic of SHS Reaction Setup

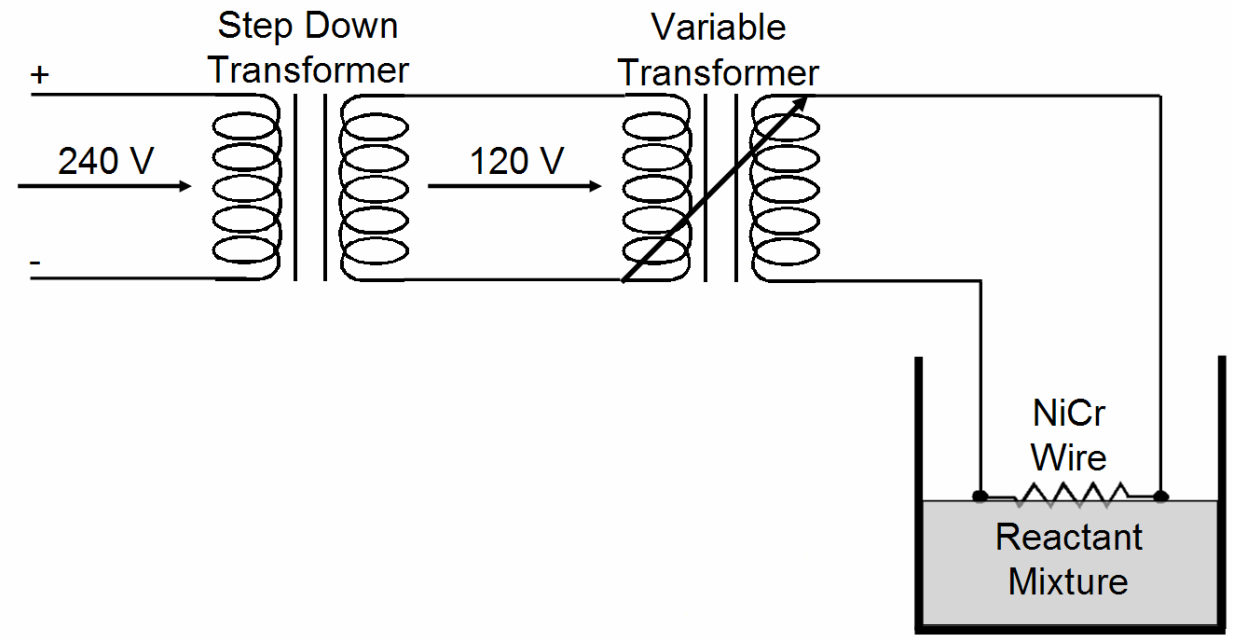

D. Gas Adsorption Surface Area Raw Data

D.1 Summary and Comparison

05/27/2008

Quantachrome Instruments
Quantachrome Autosorb Automated Gas Sorption System Report
Autosorb 1 for Windows 1.53

File name: C:\QCdata\PhysData\SHS100HR.raw
Sample ID: SHS100HR Description: SHS 100 hour - Michael
Comments:

Operator: Susan	Sample weight: 0.1147 g	
Analysis gas: Nitrogen	X sect. area: 16.2 Å²/molec	Non-ideality: 6.58e-05
Adsbate (DRP): Nitrogen	Bath Temp.: 77.30	
Outgas Temp: 300.0 °C	Outgas Time: 4.3 hrs	Analysis Time: 184.5 min
P/Po tolerance: 1	Equil. time: 3	End of run: 05/22/2008 19:01
Station #: 1	PC sw. version: 1.53	TempComp: Off

AREA-VOLUME-PORE SIZE SUMMARY

SURFACE AREA DATA

Multipoint BET	2.103E+01	m²/g
Langmuir Surface Area	2.743E+02	m²/g
BJH Method Cumulative Adsorption Surface Area	1.764E+01	m²/g
BJH Method Cumulative Desorption Surface Area	1.807E+01	m²/g
DH Method Cumulative Adsorption Surface Area	1.809E+01	m²/g
DH Method Cumulative Desorption Surface Area	1.844E+01	m²/g
t-Method External Surface Area	2.103E+01	m²/g
t-Method Micro Pore Surface Area	0.000E+00	m²/g
DR Method Micro Pore Area	6.093E+01	m²/g
NLDFT Method Cumulative Surface Area	1.580E+01	m²/g

PORE VOLUME DATA

Total Pore Volume for pores with Diameter less than 2859.8 Å at P/Po = 0.99324	1.280E-01	cc/g
BJH Method Cumulative Adsorption Pore Volume	1.256E-01	cc/g
BJH Method Cumulative Desorption Pore Volume	1.258E-01	cc/g
BJH Interpolated Cumulative Adsorption Pore Volume for pores in the range of 5000.0 to 0.0 Å Diameter	1.256E-01	cc/g
BJH Interpolated Cumulative Desorption Pore Volume for pores in the range of 5000.0 to 0.0 Å Diameter	1.258E-01	cc/g
DH Method Cumulative Adsorption Pore Volume	1.220E-01	cc/g
DH Method Cumulative Desorption Pore Volume	1.223E-01	cc/g

t-Method Micro Pore Volume.....	0.000E+00	cc/g
DR Method Micro Pore Volume.....	2.171E-02	cc/g
NLDFT Method Cumulative Pore Volume.....	9.512E-02	cc/g

PORE SIZE DATA

Average Pore Diameter.....	2.434E+02	Å
BJH Method Adsorption Pore Diameter (Mode).....	3.644E+01	Å
BJH Method Desorption Pore Diameter (Mode).....	6.116E+01	Å
DH Method Adsorption Pore Diameter (Mode).....	3.644E+01	Å
DH Method Desorption Pore Diameter (Mode).....	6.116E+01	Å
DR Method Micro Pore Width	7.686E+01	Å
NLDFT method Pore Diameter (Mode).....	1.531E+02	Å

DATA REDUCTION PARAMETERS

Thermal Transpiration : ON
Effective Molecule Diameter (D) 4.0000 Å
Effective Cell Stem Inner Diameter (d) 1.0000 mm
Last Po Acquired 512.00 mm Hg
MaxiDose : ON
Initial Fill : OFF
DoseWizard : OFF

BJH/DH Moving Average Size : 1
Thickness method : DeBoer

Interaction Constant (K) 2.9600 nm^3 x kJ/mol

ADSORBATE MODEL PARAMETERS

Adsorbate Type = Nitrogen
Adsorbate Temp. = 77.3500 K
Molecular Weight = 28.0134 g/mol
Cross-Sect. Area = 16.2000 Å²/molecule
Liquid Density = 0.8060 g/cc
Critical Temp. = 126.2000 K
Critical Pressure = 33.5000 atm
Average Diameter = 0.3000 nm
Polarizability = 1.4600 (cc/molec) x 1e-24
Magnetic Suscept. = 2.0000 (cc/molec) x 1e-29
Molecular Density = 6.7000 (molec/cm²) x 1e14
Surface Tension = 8.8500 erg/cm²
Contact Angle = 0.0000 degrees
Supercritical Ads. Constant K = 1.0000

ADSORBENT MODEL PARAMETERS

Adsorbent Type = Carbon
Atom Diameter = 0.3400 nm
Polarizability = 1.0200 (cc/molecule) x 1e-24
Magnetic Suscept. = 13.5000 (cc/molecule) x 1e-29
Surface Atom Density = 38.4500 (molec/cm²) x 1e14
Adsorbent Density = 2.2460 g/cc
DR exponent (n) = 2.0000

D.2 Pore Diameter

05/27/2008

Quantachrome Instruments
Quantachrome Autosorb Automated Gas Sorption System Report
Autosorb 1 for Windows 1.53

File name: C:\QCdata\PhysData\SHS100HR.raw
Sample ID: SHS100HR Description: SHS 100 hour - Michael
Comments:

Operator: Susan	Sample weight: 0.1147 g	
Analysis gas: Nitrogen	X sect. area: 16.2 Å²/molec	Non-ideality: 6.58e-05
Adsbate (DRP): Nitrogen	Bath Temp.: 77.30	
Outgas Temp: 300.0 °C	Outgas Time: 4.3 hrs	Analysis Time: 184.5 min
P/Po tolerance: 1	Equil. time: 3	End of run: 05/22/2008 19:01
Station #: 1	PC sw. version: 1.53	TempComp: Off

AVERAGE PORE SIZE

Average Pore Diameter = 2.434E+02 Å

D.3 Pore Volume

05/27/2008

Quantachrome Instruments
Quantachrome Autosorb Automated Gas Sorption System Report
Autosorb 1 for Windows 1.53

File name: C:\QCdata\PhysData\SHS100HR.raw
Sample ID: SHS100HR Description: SHS 100 hour - Michael
Comments:

Operator: Susan	Sample weight: 0.1147 g	
Analysis gas: Nitrogen	X sect. area: 16.2 Å²/molec	Non-ideality: 6.58e-05
Adsbate (DRP): Nitrogen	Bath Temp.: 77.30	
Outgas Temp: 300.0 °C	Outgas Time: 4.3 hrs	Analysis Time: 184.5 min

P/Po tolerance: 1 Equil. time: 3 End of run: 05/22/2008 19:01
Station #: 1 PC sw. version: 1.53 TempComp: Off

TOTAL PORE VOLUME

Total pore volume = 1.280E-01 cc/g for

pores smaller than 2859.8 Å (Diameter),

at P/Po = 0.99324

D.4 Multi-Point BET

05/27/2008

Quantachrome Instruments
Quantachrome Autosorb Automated Gas Sorption System Report
Autosorb 1 for Windows 1.53

File name: C:\QCdata\PhysData\SHS100HR.raw
Sample ID: SHS100HR Description: SHS 100 hour - Michael
Comments:
Operator: Susan Sample weight: 0.1147 g
Analysis gas: Nitrogen X sect. area: 16.2 Å²/molec Non-ideality: 6.58e-05
Adsbate (DRP): Nitrogen Bath Temp.: 77.30
Outgas Temp: 300.0 °C Outgas Time: 4.3 hrs Analysis Time: 184.5 min
P/Po tolerance: 1 Equil. time: 3 End of run: 05/22/2008 19:01
Station #: 1 PC sw. version: 1.53 TempComp: Off

MULTIPOINT BET

P/Po	Volume [cc/g] STP	1/(W((Po/P)-1))
1.0421e-01	5.4487	1.708E+01
2.0236e-01	6.2050	3.271E+01
3.0192e-01	6.9332	4.991E+01

Area = 2.103E+01 m²/g

Slope = 1.661E+02

Y - Intercept = -4.463E-01

Correlation Coefficient = 0.999725

C = -3.711E+02

E. Additional Micrographs

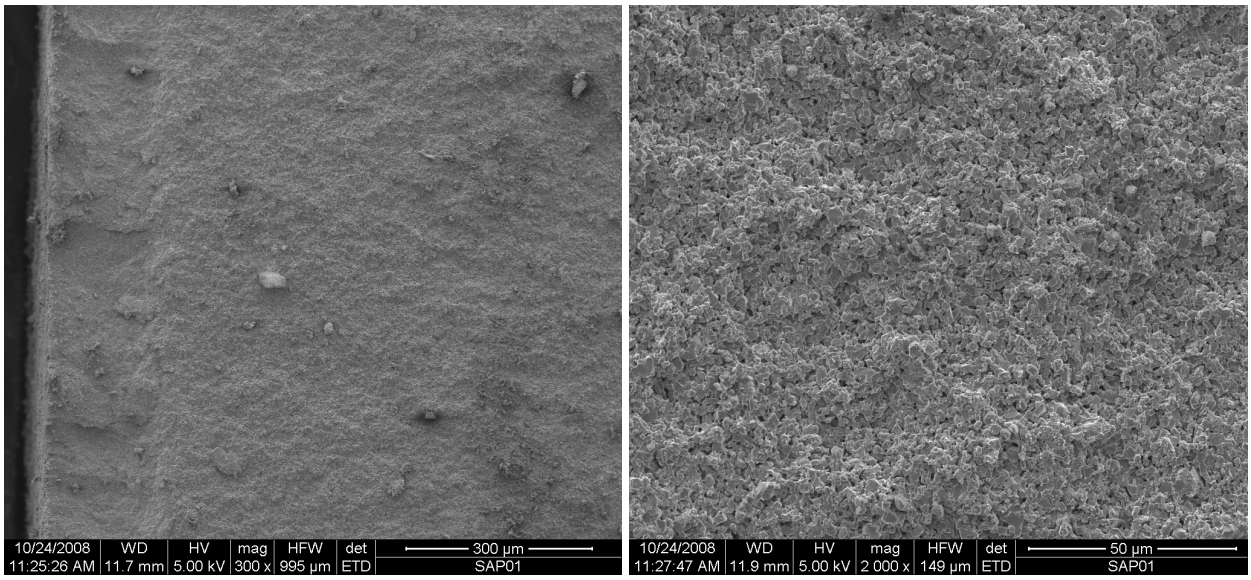

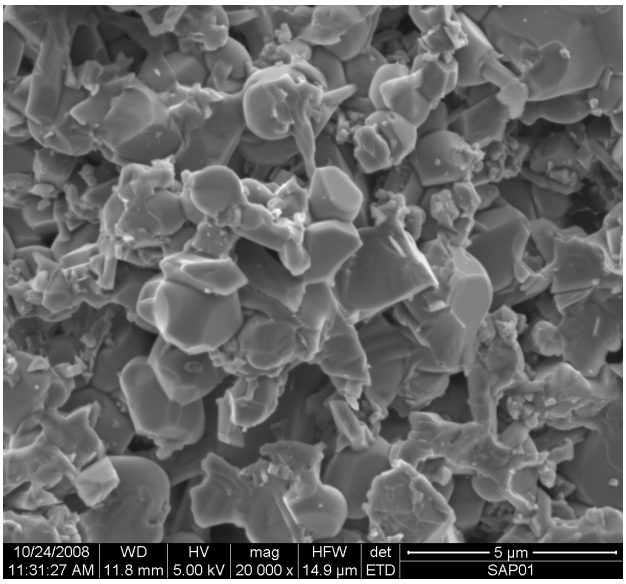

Figure E.1– SEM micrographs of samples heat treated at 1370°C for 30 minutes.

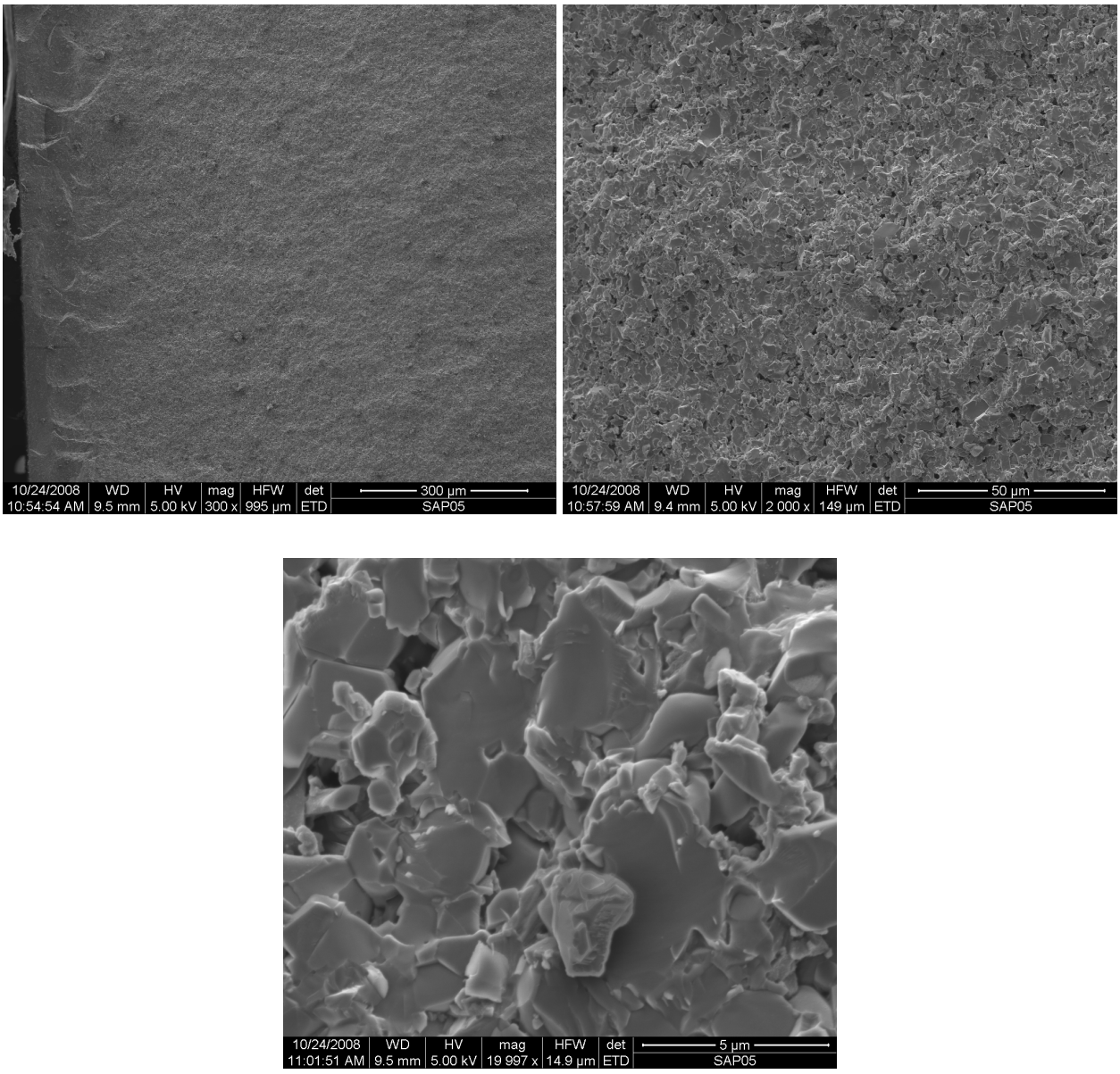

Figure E.2 – SEM micrographs of samples heat treated at 1500°C for 60 minutes.

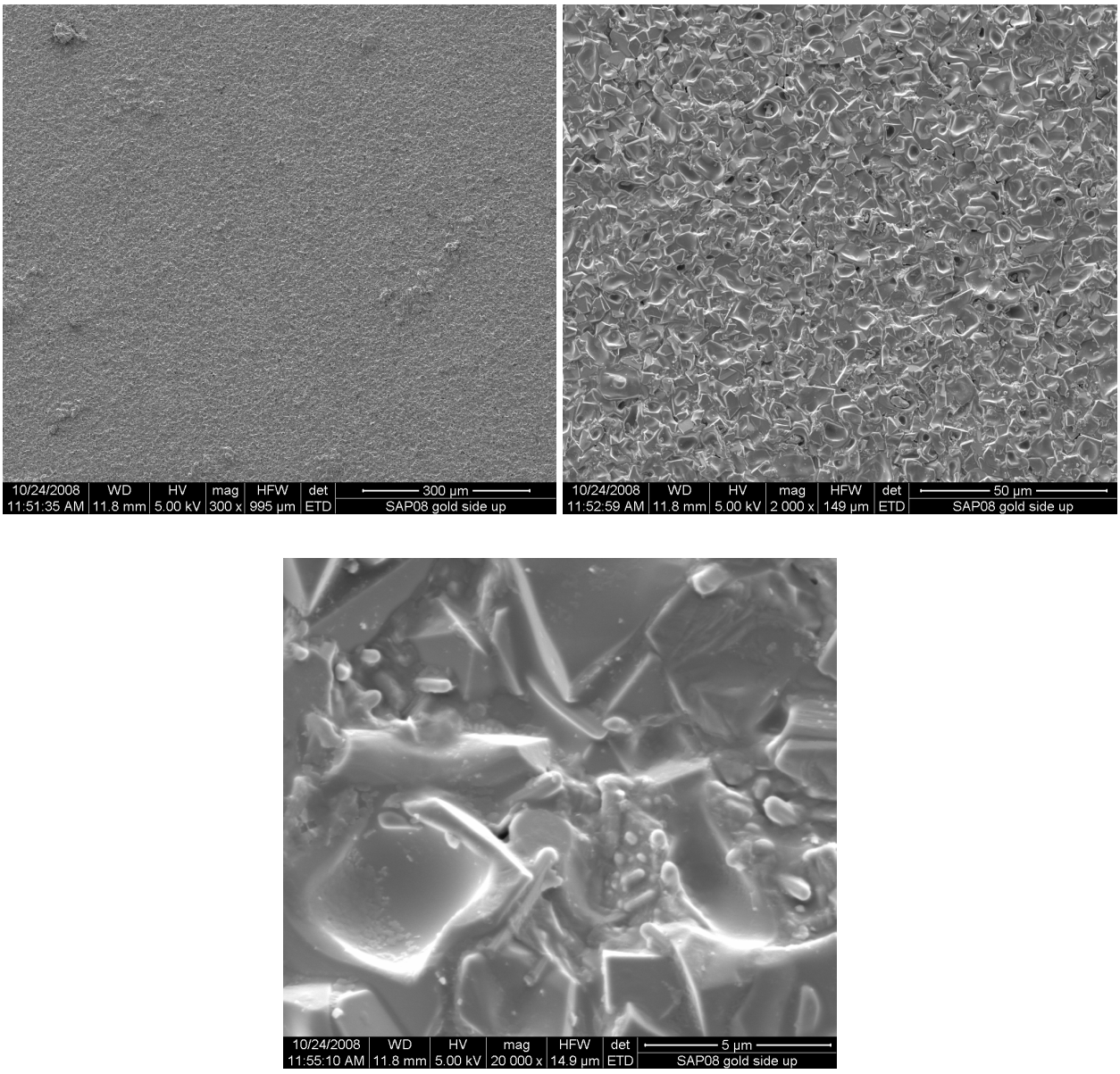

Figure E.3 – SEM micrographs of the bottom surface of a sample that was exposed to an oxidizing atmosphere during cooling.

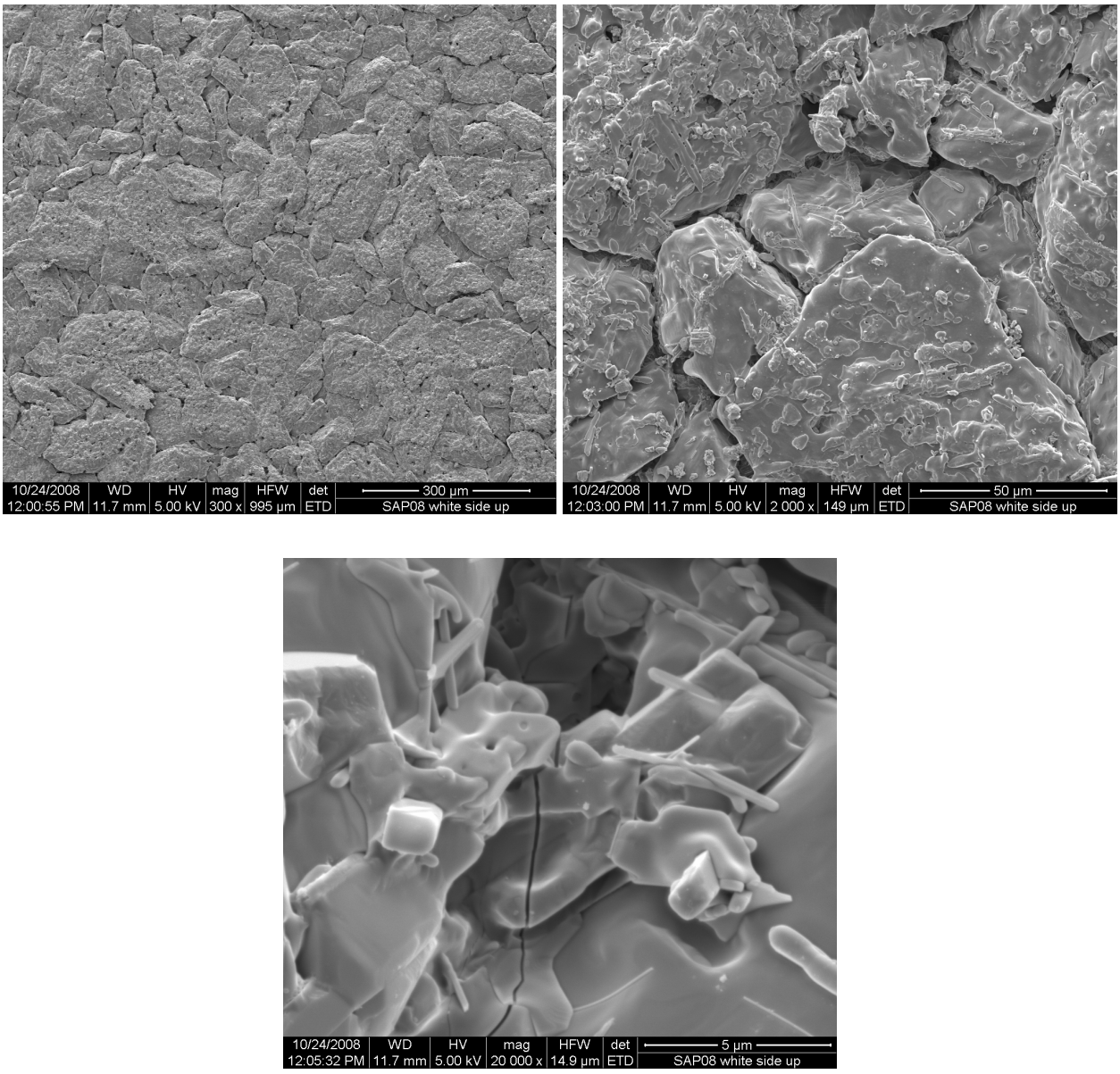

Figure E.4 – SEM micrographs of the top surface of a sample that was exposed to an oxidizing atmosphere during cooling.

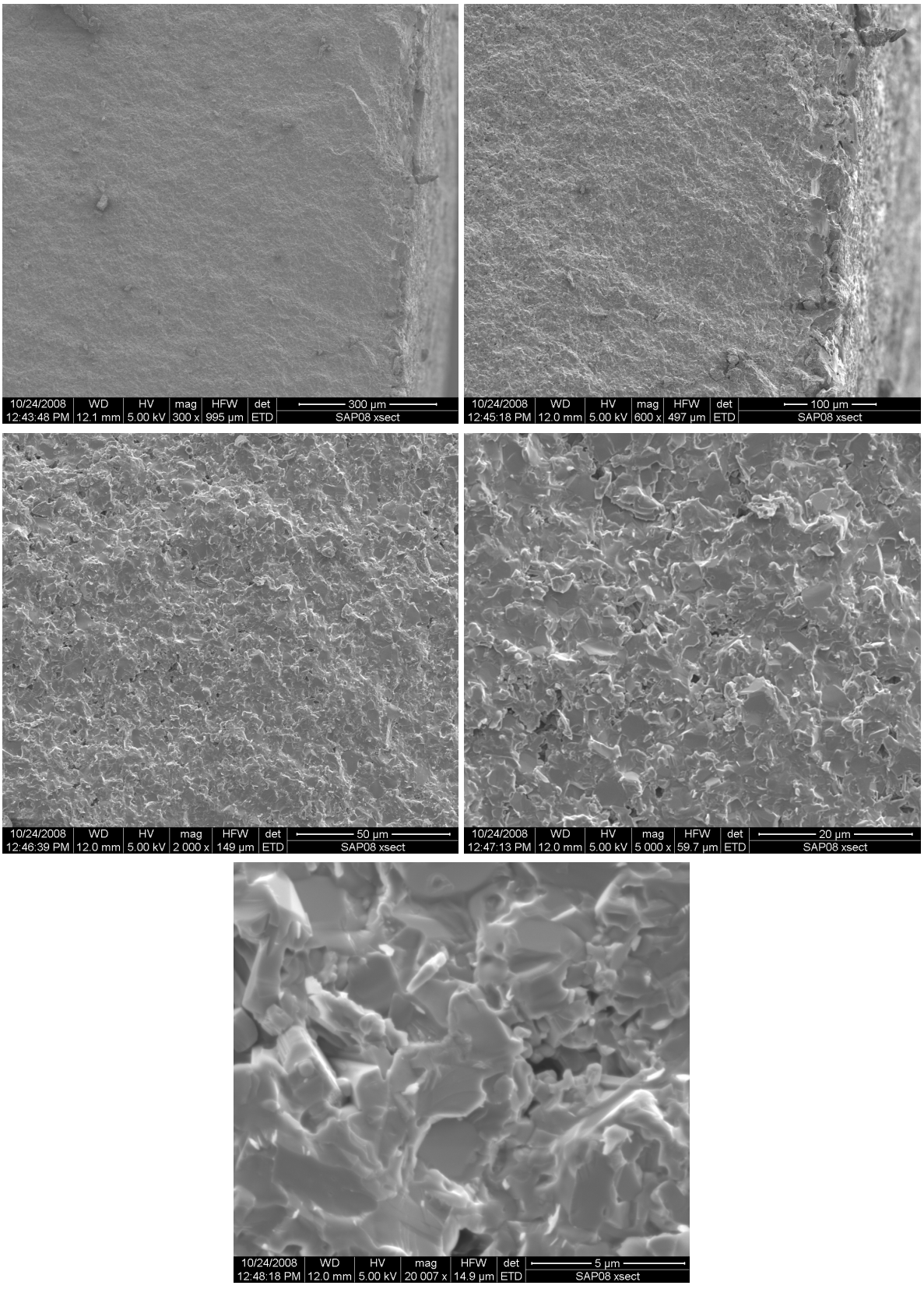

Figure E.5 – SEM micrographs of the cross-section of a sample that was exposed to an oxidizing atmosphere during cooling.

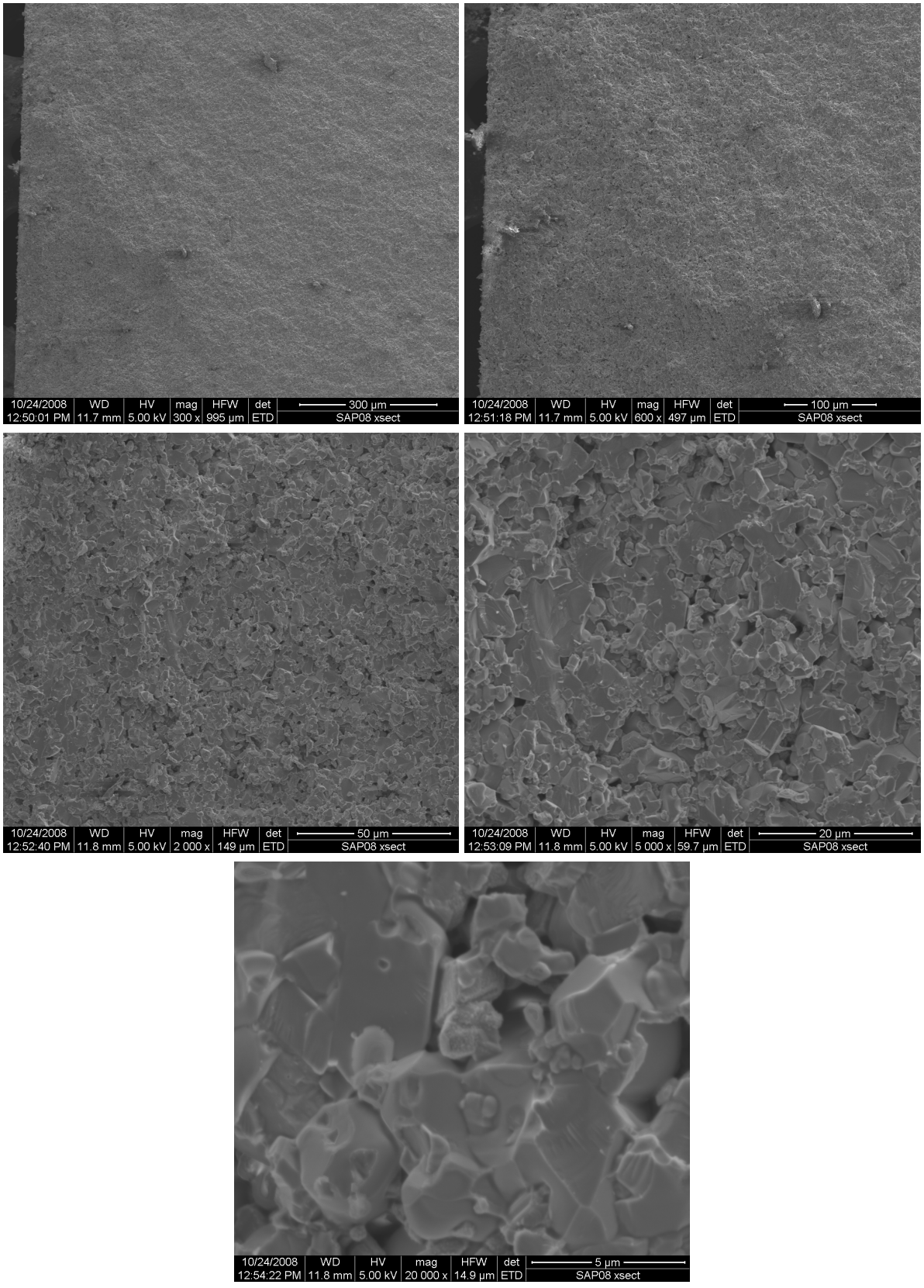

Figure E.6 - SEM micrographs of another cross-sectional area of a sample that was exposed to an oxidizing atmosphere during cooling.

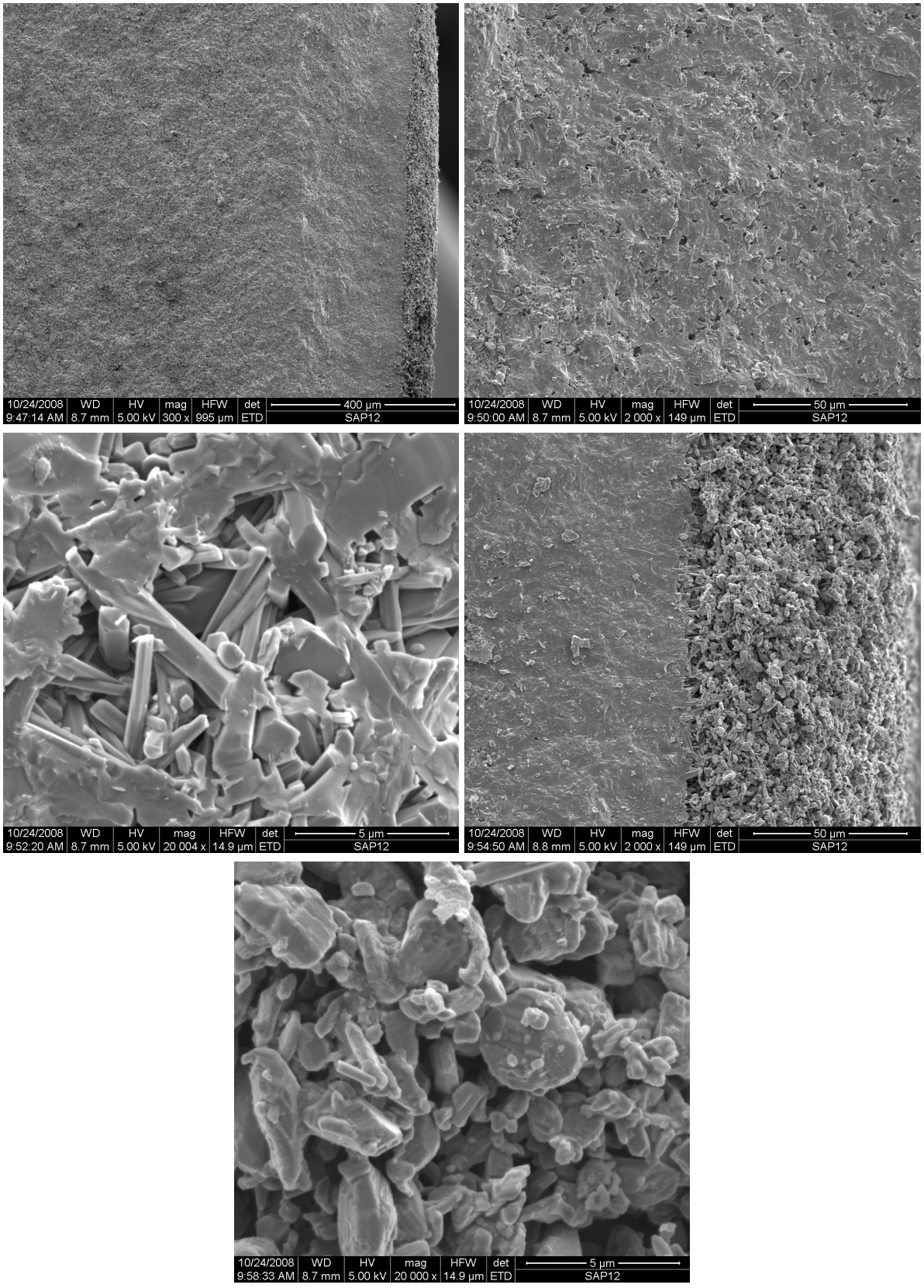

Figure E.7 – SEM micrographs from a sample heat treated at 1500°C for 30 minutes.

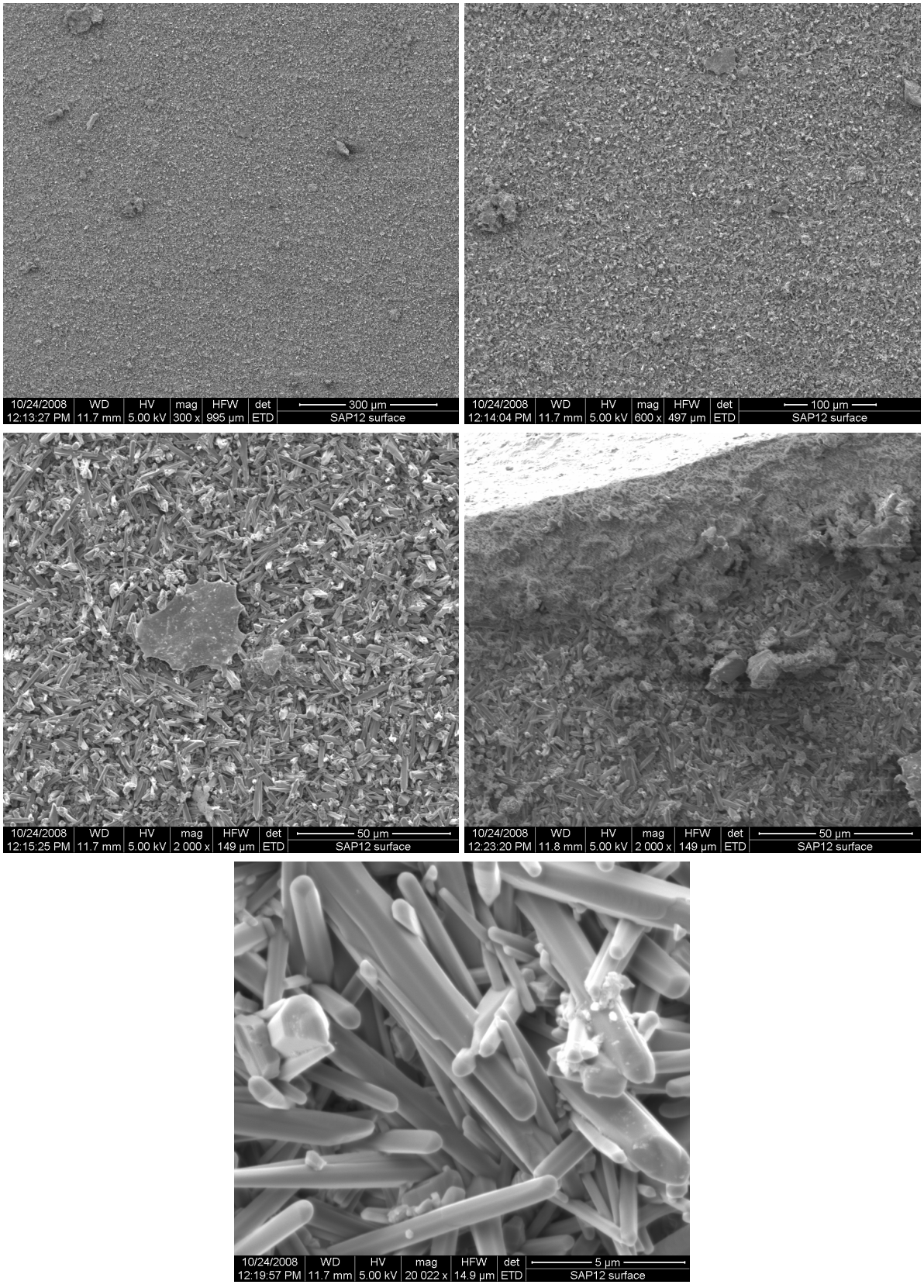

Figure E.8 – SEM micrographs of the surface of a sample heat treated at 1500°C for 30 minutes

F. Density Calculations Raw Data

Table F.1 – Density Data for Samples Heat Treated at 1500°C for 30 Minutes

Sample ID	Water Density (g/cm^3)	Dry Mass (g)	Suspended Mass (g)	Saturated Mass (g)
ST/A040108001SAP10	0.99987	5.9303	4.3093	6.1383
ST/A040108001SAP12	0.99987	5.8400	4.2395	6.0684
ST/A040108001SAP13	0.99987	5.8231	4.2215	6.0863

Sample ID	Exterior Volume (cm^3)	Pore Volume (cm^3)	Impervious Volume (cm^3)	Apparent Porosity (%)	Liquid Absorption (%)	Immersion Bulk Density (g/cm^3)
ST/A040108001SAP10	1.8292	0.2080	1.6212	11.37	3.51	3.2420
ST/A040108001SAP12	1.8291	0.2284	1.6007	12.49	3.91	3.1928
ST/A040108001SAP13	1.8650	0.2632	1.6018	14.11	4.52	3.1222

Table F.2 – Density Data for Samples Heat Treated at 1500°C for 60 Minutes

Sample ID	Water Density (g/cm^3)	Dry Mass (g)	Suspended Mass (g)	Saturated Mass (g)
ST/A040108001SAP04	0.99987	5.8357	4.2901	6.0625
ST/A040108001SAP05	0.99987	5.8346	4.2871	6.0555
ST/A040108001SAP06	0.99987	5.8613	4.3093	6.0780

Sample ID	Exterior Volume (cm^3)	Pore Volume (cm^3)	Impervious Volume (cm^3)	Apparent Porosity (%)	Liquid Absorption (%)	Immersion Bulk Density (g/cm^3)
ST/A040108001SAP04	1.7726	0.2268	1.5458	12.80	3.89	3.2921
ST/A040108001SAP05	1.7686	0.2209	1.5477	12.49	3.79	3.2990
ST/A040108001SAP06	1.7689	0.2167	1.5522	12.25	3.70	3.3135

Table F.3 – Density Data for Samples Heat Treated at 1500°C for 90 Minutes

Sample ID	Water Density (g/cm^3)	Dry Mass (g)	Suspended Mass (g)	Saturated Mass (g)
ST/A040108001SAP14	0.99987	5.7791	4.2117	5.9200
ST/A040108001SAP15	0.99987	5.7590	4.1932	5.8823
ST/A040108001SAP16	0.99987	5.8295	4.2384	5.9598

Sample ID	Exterior Volume (cm^3)	Pore Volume (cm^3)	Impervious Volume (cm^3)	Apparent Porosity (%)	Liquid Absorption (%)	Immersion Bulk Density (g/cm^3)
ST/A040108001SAP14	1.7085	0.1409	1.5676	8.25	2.44	3.3825
ST/A040108001SAP15	1.6893	0.1233	1.5660	7.30	2.14	3.4091
ST/A040108001SAP16	1.7216	0.1303	1.5913	7.57	2.24	3.3861

Table F.4 – Density Data for Samples Heat Treated at 1370°C for 30 Minutes

Sample ID	Water Density (g/cm^3)	Dry Mass (g)	Suspended Mass (g)	Saturated Mass (g)
ST/A040108001SAP01	0.99987	5.8476	4.3009	6.3599
ST/A040108001SAP02	0.99987	5.8548	4.3137	6.3508
ST/A040108001SAP03	0.99987	5.8530	4.3007	6.3417

Sample ID	Exterior Volume (cm^3)	Pore Volume (cm^3)	Impervious Volume (cm^3)	Apparent Porosity (%)	Liquid Absorption (%)	Immersion Bulk Density (g/cm^3)
ST/A040108001SAP01	2.0593	0.5124	1.5469	24.88	8.76	2.8397
ST/A040108001SAP02	2.0374	0.4961	1.5413	24.35	8.47	2.8397
ST/A040108001SAP03	2.0413	0.4888	1.5525	23.94	8.35	2.8674

Table F.5 – Density Data for Samples Heat Treated at 1435°C for 30 Minutes

Sample ID	Water Density (g/cm^3)	Dry Mass (g)	Suspended Mass (g)	Saturated Mass (g)
ST/A040108001SAP17	0.99987	5.9550	4.3119	6.3802
ST/A040108001SAP18	0.99987	5.9215	4.2495	6.3061
ST/A040108001SAP19	0.99987	5.8730	4.2365	6.2967

Sample ID	Exterior Volume (cm^3)	Pore Volume (cm^3)	Impervious Volume (cm^3)	Apparent Porosity (%)	Liquid Absorption (%)	Immersion Bulk Density (g/cm^3)
ST/A040108001SAP17	2.0686	0.4253	1.6433	20.56	7.14	2.8788
ST/A040108001SAP18	2.0569	0.3846	1.6722	18.70	6.49	2.8789
ST/A040108001SAP19	2.0605	0.4238	1.6367	20.57	7.21	2.8503

Table F.6 – Density Data for Samples Exposed to an Oxidizing Atmosphere During Cooling

Sample ID	Water Density (g/cm^3)	Dry Mass (g)	Suspended Mass (g)	Saturated Mass (g)
ST/A040108001SAP07	0.99987	5.9303	4.3093	6.1383
ST/A040108001SAP08	0.99987	5.8400	4.2395	6.0684
ST/A040108001SAP09	0.99987	5.8231	4.2215	6.0863

Sample ID	Exterior Volume (cm^3)	Pore Volume (cm^3)	Impervious Volume (cm^3)	Apparent Porosity (%)	Liquid Absorption (%)	Immersion Bulk Density (g/cm^3)
ST/A040108001SAP07	1.8292	0.2080	1.6212	11.37	3.51	3.2420
ST/A040108001SAP08	1.8291	0.2284	1.6007	12.49	3.91	3.1928
ST/A040108001SAP09	1.8650	0.2632	1.6018	14.11	4.52	3.1222

References

1. **J. Matsushita, et al.** *Pressureless Sintering of TiB2-Al2O3*. Journal of the Ceramic Society of Japan (1989). Vol. 97 (1200-1205): p. 240-245.
2. **W. Stadlbauer, et al.** *Al2O3-TiB2 Composite Ceramics*. Journal of Materials Science (1989). Vol. 8 (10): p. 1217-1220 (Hardcopy).
3. **K. V. Logan**. *Elastic-Plastic Behavior of Hot Pressed Composite Titanium Diboride/Alumina Powders Produced Using Self-Propagating High Temperature Synthesis*. The Georgia Institute of Technology: Materials Science and Engineering (1992). Doctor of Philosophy.
4. **R. A. Cutler, et al.** *Synthesis, Sintering, Microstructure, and Mechanical Properties of Ceramics Made by Exothermic Reactions*. Journal of the American Ceramic Society (1992). Vol. 75 (1): p. 36-43.
5. **A. K. Khanra, et al.** *Sintering Behavior of Ultra-Fine Titanium Diboride Powder Prepared by Self-Propagating High-Temperature Synthesis (SHS) Technique*. Materials Science and Engineering A (2007). p. 281-287.
6. **M. Cirakoglu, et al.** *Combustion Synthesis Processing of Functionally Graded Materials in the Ti–B Binary System*. Journal of Alloys and Compounds (2002). Vol. 347: p. 259-265.
7. **M. A. Meyers, et al.** *Combustion Synthesis/Densification of an Al2O3–TiB2 Composite*. Materials Science and Engineering A (2001). Vol. 311: p. 83-99.
8. **A. L. Maximenko and E. A. Olevsky**. *Effective Diffusion Coefficients in Solid-State Sintering*. Acta Materialia (2004). Vol. 52: p. 2953-2963.
9. **S. R. Lampman, et al.** *Engineering Materials Handbook: Ceramics and Glasses (2nd ed.)*. ASM International: Materials Park (2000). Vol. 4.
10. **R. J. McAfee and I. Nettleship**. *A Mesoscale Description of Microstructure Evolution for the Sintering of Ceramics*. Acta Materialia (2005). Vol. 53: p. 4305-4311.
11. **M. F. Ashby**. *Materials Selection in Mechanical Design (3rd ed*.). Elsevier Butterworth-Heinemann: Oxford (2005).
12. **M. M. Opeka, et al.** *Oxidation-Based Materials Selection for 2000C+ Hypersonic Aerosurfaces: Theoretical Considerations and Historical Experience*. Journal of Materials Science (2004). Vol. 39: p. 5887-5904.
13. **M. N. Rahaman**. *Ceramic Processing*. CRC/Taylor & Francis: Boca Raton, FL. (2007).
14. **D. W. Richardson**. *Modern Ceramic Engineering: Properties, Processing, and Use in Design (3rd ed*.). CRC Taylor & Francis: Boca Raton, FL (2006).
15. **M. Braginsky, et al.** *Numerical Simulation of Solid State Sintering*. International Journal of Solids and Structures (2005). Vol. 42: p. 621-636.
16. **R. M. German**. *A Sintering Parameter for Submicron Powders*. Science of Sintering (1978). Vol. 10 (1): p. 11-25.
17. **G. Agarwal and R. F. Speyer**. *Effect of Rate Controlled Sintering on Microstructure and Electrical Properties of ZnO Doped with Bismuth and Antimony Oxides*. Journal of Materials Research (1997). Vol. 12 (9): p. 2447-2454.
18. **K. S. Meyers, et al.** *Rate Controlled Sintering of Nano-Sized BaTiO3*. SPIE Conference on Sensory Phenomena and Measurement Instrumentation for Smart Structures and Materials (1998): San Diego, CA. SPIE. Vol. 3330: p. 80-89.

19. **J. Fuller**. *Guest Editorial: Ultra-High Temperature Ceramics*. Journal of Materials Science (2004). Vol. 39: p. 5885.
20. **R. Telle, et al.** *Boride-Based Hard Materials*. Vol. 2: p. 802-945.
21. **H. Pastor**. *Metallic Borides: Preparation of Solid Bodies - Sintering Methods and Properties of Solid Bodies*. Springer-Verlag: New York (1977). p. 457-493 (Hardcopy).
22. **M. F. Ashby**. *CES Selecter (Ver. 4.6)*. Granta Design Limited: Cambridge (2005). Software for finding material properties, comparing materials, and deciding which materials to use by user defined criteria.
23. **R. G. Munro**. *Material Properties of Titanium Diboride*. Journal of Research of the National Institute of Standards and Technology (2000). Vol. 105 (5): p. 709-720.
24. **D. Jianxin, et al.** *Self-Lubricating Behaviors of Al2O3/TiB2 Ceramic Tools in High-Speed Machining of Hardened Steel*. Journal of the European Ceramic Society (2005). Vol. 25: p. 1073-1079.
25. **A. R. Keller and M. Zhou**. *Effect of Microstructure on Dynamic Failure Resistance of Titanium Diboride/Alumina Ceramics*. Journal of the American Ceramic Society (2003). Vol. 86 (3): p. 449-457.
26. **J. W. Adams, et al.** *Microstructure Development of Aluminum Oxide/Titanium Diboride Composites for Penetration Resistance*. Journal of the American Ceramic Society. p. (Hardcopy).
27. **G. A. Gilde and J. W. Adams**. *Processing and Ballistic Performance of Al2O3/TiB2 Composites*.
28. **P. Lundberg, et al.** *Impact of Metallic Projectiles on Ceramic Targets: Transition Between Interface Defeat and Penetration*. International Journal of Impact Engineering (2000). Vol. 24: p. 259-275.
29. **W. D. Callister**. *Materials Science and Engineering: An Introduction (6th ed*.). John Wiley & Sons, Inc.: New York (2003).
30. **R. Limpert**. *Brake Design and Safety (2nd ed*.). Society of Automotive Engineers, Inc.: (1999).
31. **S. Baik and P. F. Becher**. *Effect of Oxygen Contamination on Densification of TiB2*. Journal of the American Ceramic Society (1987). Vol. 70 (8): p. 527-530.
32. **A. Fedorov, et al.** *Stability of Hypersonic Boundary Layer on Porous Wall with Regular Microstructure*. AIAA Journal (2006). Vol. 44 (8): p. 1866-1871.
33. **D. Manor, et al.** *Aerothermodynamic Environments and Thermal Protection for a Wave-Rider Second Stage*. Journal of Spacecraft and Rockets (2005). Vol. 42 (2): p. 208-212.
34. **A. Maslov, et al.** *Hypersonic Laminar Flow Control Using a Porous Coating of Random Microstructure*. 44th AIAA Aerospace Sciences Meeting and Exhibit (2006): Reno, Nevada. AIAA
35. **D. Mattia, et al.** *Oxidation Behaviour of an Aluminum Nitride-Hafnium Diboride Ceramic Composite*. Journal of the European Ceramic Society (2005). Vol. 25: p. 1789-1796.
36. **M. Singh and H. Wiedemeier**. *Chemical Interactions in Diboride-Reinforced Oxide-Matrix Composites*. Journal of the American Ceramic Society (1991). Vol. 74 (4): p. 724-727.
37. **A. Abada**. *Processing, Compatibility, and Oxidation of Diboride Reinforced Oxide Matrix Composites for Ultra High Temperature Applications*. Case Western Reserve

University: Department of Metallurgy and Materials Science (1990). Doctor of Philosophy.
38. **Y. I. Krylov and T. S. Sergeeva**. *Thermal Stability of Composite Materials Based on Boride-Oxide Systems*. Powder Metallurgy and Metal Ceramics (1977). Vol. 16 (8): p. 637-640.
39. **J. Han, et al.** *Thermal Shock Resistance of TiB2-Cu Interpentrating Phase Composites*. Composites Science and Technology (2005). Vol. 65: p. 1711-1718.
40. **Y. Sawai and Y. Shibagaki**. *AE Measuring System at High Temperature for Ceramics with Low Thermal Expansion due to Microcracking*. Journal of Materials Science (2004). Vol. 39: p. 3483-3485.
41. **L. D. Wegner and L. J. Gibson**. *The Mechanical Behaviour of Interpenetrating Phase Composites - I: Modelling*. International Journal of Mechanical Sciences (2000). Vol. 42 (5): p. 925-942.
42. **L. D. Wegner and L. J. Gibson**. *The Mechanical Behaviour of Interpenetrating Phase Composites – II: A Case Study of a Three-Dimensionally Printed Material*. International Journal of Mechanical Sciences (2000). Vol. 42 (5): p. 943-964.
43. **N. Stadlbauer, et al.** *Al2O3-TiB2 Composite Ceramics*. Journal of Materials Science (1989). Vol. V8 (N10): p. 1217-1220 (Hardcopy).
44. **J. Toon**. *Company Begins Production of Improved High-Performance Materials for Cutting Tools, Dies and Electrodes*. Georgia Tech Research News (1995). June 7, 2007. Available From: http://gtresearchnews.gatech.edu/newsrelease/TIB2.html
45. **C. F. Feng and L. Froyen**. *On the Reaction Kinetics of an Al-TiO2-B System for Producing In-Situ Al/(Al203+TiB2) Composites*. Journal of Materials Science (2000). Vol. 19: p. 103-105.
46. **ACerS and NIST**. *Phase Equilibria Diagrams*. American Ceramics Society and National Institute of Standards and Technology - Ceramics Division: (1992-2008).
47. **G. Pickrell**. *Crystal Chemistry and Phase Equilibria*. MSE 5984 (Fall 2006) - Graduate course on principles and fundamentals of phase equilibria.
48. **P. J. M. Gielisse and W. R. Foster**. *The System Al2O3-B2O3*. Nature (1862). Vol. 195: p. 69-70.
49. **S. Postrach and J. Potschke**. *Pressureless Sintering of Al2O3 Containing up to 20 Vol% Zirconium Diboride (ZrB2)*. Journal of the European Ceramic Society (2000). Vol. 20: p. 1459-1468.
50. **X. Tao, et al.** *Nanomechanical Characterization of One-Step Combustion-Synthesized Al4B2O9 and Al18B4O33 Nanowires*. Nano Letters (2007). Vol. 7 (10): p. 3172-3176.
51. **P. Doerner, et al.** *CALPHAD: Comput. Coupling Phase Diagrams Thermochem.* (1979). (Fig. 06434).
52. **J. Wang, et al.** *Chemical Synthesis of Al14B4O33 Whiskers Via a Combustion Method*. Materials Letters (2008). Vol. 62: p. 2447-2449.
53. **J. Wang, et al.** *Large-Scale Synthesis of Al4B2O9/Al18B4O33 Whiskers Via a Novel Method*. Materials Letters (2008). Vol. 62: p. 1208-1211.
54. **K. V. Logan and G. R. Villalobos**. *Advanced Armor Materials Development*. U.S. Army Research Office (1993). (Contract No.: DAAL-03-88-K0042).
55. **B. I. Lee and E. J. A. Pope**. *Chemical Processing of Ceramics*. Marcel Dekker: New York (1994).

56. **M. E. Möbius, et al.** *Size Seperation of Granular Particles*. Nature (2001). Vol. 414 (11): p. 270.
57. **M. P. Hunt and K. V. Logan**. *Pressureless Sintering of Titanium Diboride Powders*. 32nd International Conference and Exposition on Advanced Ceramics and Composites (2008): Daytona Beach, FL.
58. **W. J. Tang, et al.** *Fabrication and Characteristics of TiB2/Al2O3 Core/Shell Particles by Hybridization*. Powder Technology (2006). Vol. 167: p. 117-123.
59. **D. Schwechten**. *Method for Fluidized Bed Jet Mill Grinding*. USA Patent No.: (November 30, 1999)
60. **P. Woodall and U. Enderle**. *Attrition Mill*. USA Patent No.: 5797550 (August 25, 1998)
61. **I. Gentle**. *Interfacial Science: An Introduction*. Oxford University Press: Oxford (2005).
62. **E. Kaufmann**. *Characterization of Materials*. Wiley-Interscience: Hoboken, NJ (2003). Vol. 1.
63. **B. D. Cullity and S. R. Stock**. *Elements of X-Ray Diffraction (2nd ed*.). Prentice Hall, Inc.: Upper Saddle River, NJ (2001).
64. **L. V. Azaroff**. *Elements of X-Ray Crystallography*. McGraw-Hill, Inc.: New York (1968).
65. **H. D. Young and R. A. Freedman**. *University Physics (10th ed*.). Addison-Wesley: New York (2000).
66. **J. Antony**. *Design of Experiments for Engineers and Scientists*. Elsevier Butterworth-Heinemann: Oxford (2003).
67. **G. Pickrell**. *Introduction to Materials Optimization Through Designed Experiments*. MSE 4984 (Spring 2006) - Undergraduate course in design of experiments, six sigma, and Taguchi methods.
68. **R. K. Bordia and R. Raj**. *Analysis of Sintering of a Compostie with a Glass or Ceramic Matrix*. Journal of the American Ceramic Society (1986). Vol. 69 (3): p. C-55 - C-57.
69. **Y. S. Kang, et al.** *Effect of Addition of Cr on the Sintering of TiB2 Ceramics*. Journal of Materials Science (2005). Vol. 40:
70. **L.-H. Li, et al.** *Sintering and Mechanical Properties of Titanium Diboride with Aluminum Nitride as a Sintering Aid*. Journal of the European Ceramic Society (2002). Vol. 22: p. 973-977.
71. **W. Wang, et al.** *Influence of Hot Pressing Sintering Temperature and Time on Microstructure and Mechanical Properties of TiB2 Ceramics*. Journal of the European Ceramic Society (2002). Vol. 22: p. 1045-1049.
72. **O. F. Devereux**. *Topics in Metallurgical Thermodynamics*. Wiley & Sons: New York (1983).
73. **J. M. Howe**. *Interfaces in Materials: Atomic Structure, Thermodynamics and Kinetics of Solid-Vapor, Solid-Liquid, and Solid-Solid Interfaces*. Wiley: New York (1997).
74. **D. R. Gaskell**. *Introduction to the Thermodynamics of Materials (4th ed*.). Taylor & Francis: London (2003).
75. **D. R. Gaskell**. *An Introduction to Transport Phenomena in Materials Engineering*. Macmillan Publishing Company: New York (1992).
76. **M. E. Glicksman**. *Diffusion in Solids: Field Theory, Solid State Principles, and Applications*. John Wiley & Sons, Inc.: New York (2000).
77. **D. Farkas**. *Diffusion and Kinetics*. MSE 5064 (Spring 2007) - Graduate course on diffusion processes and kinetics of materials transport.

78. **R. M. German and J. F. Lathrop**. *Simulation of Spherical Powder Sintering by Surface Diffusion*. Journal of Materials Science (1978). Vol. 13: p. 921-929.
79. **H. Ichinose and G. C. Kuczynski**. *Role of Grain Boundaries in Sintering*. Acta Metallurgica (1962). Vol. 10: p. 209-213.
80. **D. L. Johnson and T. M. Clarke**. *Grain Boundary and Volume Diffusion in the Sintering of Silver*. Acta Metallurgica (1964). Vol. 12: p. 1173-1179.
81. **D. L. Johnson and I. B. Cutler**. *Diffusion Sintering: I, Initial Stage Sintering Models and Their Application to Shrinkage of Powder Compacts*. Journal of the American Ceramic Society (1963). Vol. 46 (11): p. 541-545.
82. **J. L. Johnson and R. M. German**. *Solid-State Contributions to Densification During Liquid-Phase Sintering*. Metallurgical and Materials Transactions B (1996). Vol. 27B: p. 901-909.
83. **W. D. Kingery and M. Berg**. *Study of the Initial Stages of Sintering Solids by Viscous Flow, Evaporation-Condensation, and Self Diffusion*. Journal of Applied Physics (1955). Vol. 26 (10): p. 1205-1212.
84. **L. Levin, et al.** *Solid State Sintering Kinetics in an Iron-Based Friction Material*. Powder Metallurgy International (1980). Vol. 12 (1): p. 26-27.
85. **J. Zhu, et al.** *Microstructure Dependence of Diffusional Transport*. Computational Materials Science (2001). Vol. 20: p. 37-47.
86. **M. Winter**. *WebElements Periodic Table of Elements*. The University of Sheffield: (1993 - 2008). June 3, 2008. Available From: http://www.webelements.com/
87. **R. L. Coble**. *Initial Sintering of Alumina and Hematite*. Journal of the American Ceramic Society (1958). Vol. 41 (2): p. 55-62.
88. **J. L. Shi**. *Solid State Sintering of Ceramics: Pore Microstructure Models, Densification Equations, and Applications*. Journal of Materials Science (1999). Vol. 34: p. 3801-3812.
89. **F. Tang, et al.** *Solid State Sintering and Consolidation of Al Powders and Al Matrix Composites*. Journal of Light Metals (2002). Vol. 2: p. 201-214.
90. **G. Bockstiegel**. *On the Rate of Sintering*. Journal of Metals (1956). p. 580-585.
91. *X'Pert Pro Diffractometer*. Physics Department - University of North Dakota: Grand Forks, ND (2004). November 2008. Available From: http://www.physics.und.edu/facilities_xrd.html
92. *HORIBA: Particle Size Distribution Analyzer/Partica LA-950*. Horiba, Ltd.: (2009). November 2008. Available From: http://www.jp.horiba.com/analy_e/la-950/
93. *Hitachi High Technologies America: S-3700N Ultra Large VP-SEM*. (2002). November 2008. Available From: http://www.hitachi-hta.com/pageloader~type~product~id~464~orgid~42.html
94. *Surface Area Analyzer and Pore Size Analyzer: Autosorb-1*. Quantachrome Instruments: (2008). Available From: http://www.quantachrome.com/gassorption/images/as_1.png
95. *ICTAS*. Virginia Tech/Institute for Critical Technology and Applied Science - Nanoscale Characterization and Fabrication Laboratory: Blacksburg, VA. November 2008. Available From: http://www.ictas.vt.edu/facilities/esem.shtml